学位論文

Strain and Chemical Engineering of Electrical Properties in Perovskite Oxynitride Epitaxial Thin Films

（歪および化学組成制御によるペロブスカイト型酸窒化物
エピタキシャル薄膜の電気物性開拓）

平成26年12月博士（理学）申請

東京大学大学院理学系研究科
化学専攻
岡　大地

Strain and Chemical Engineering of Electrical Properties in Perovskite Oxynitride Epitaxial Thin Films

by

Daichi Oka

Department of Chemistry
Graduate School of Science
The University of Tokyo

December, 2014

Abstract

Perovskite oxynitrides are new and promising classes of electrical materials because of their unique properties including high dielectric constant and colossal magnetoresistance. However, they have difficulty in preparing dense specimens with the conventional synthesis method, which has prevented reliable evaluation of the electrical properties and progress of researches on the material group. To tackle this issue, I fabricated single crystalline perovskite oxynitride specimens suitable for electrical measurements using an epitaxial thin film growth technique. Electrical properties of the obtained thin films as influenced by arrangement of nitrogen were investigated.

I adopted nitrogen plasma assisted pulsed laser deposition (NPA-PLD) for the thin film growth of $SrTaO_2N$, a representative of perovskite oxynitrides, on $SrTiO_3$ (STO) substrates. I obtained stoichiometric single crystalline thin films with high crystallinity through optimization on the film growth conditions. Furthermore, I successfully synthesized another perovskite oxynitride, $CaTaO_2N$, by changing the starting material and by slightly modifying the film growth conditions, which indicated versatility of NPA-PLD as a technique to synthesize single crystalline oxynitrides with a wide range of cation combination. Impedance measurements revealed high insulating natures of the obtained thin films, which assures that their quality was high enough to conduct reliable electrical measurements.

Using piezoresponse force microscope (PFM), I investigated ferroelectricity of the $SrTaO_2N$ epitaxial thin film, which was highly strained by STO substrate with smaller lattice constants. Precise PFM measurements revealed small domains (10^1–10^2

nm) exhibiting classical ferroelectricity, which has not been observed in perovskite oxynitrides so far. The surrounding matrix region exhibited relaxor ferroelectric-like behavior, with remanent polarization invoked by domain poling. First-principles calculations suggested that the small domains had *trans*-type structure which was stabilized by tetragonal distortion caused by epitaxial stress, while the surrounding region is plausibly composed of thermodynamically stable *cis*-type anion arrangements.

Next, I performed structural characterizations of anion distribution in a series of $Ca_{1-x}Sr_xTaO_2N$ epitaxial thin films in which epitaxial strain was systematically controlled by changing the composition parameter x and the kind of substrate. The films grew coherently in the range of $0 \leq x \leq 0.5$ on STO substrate and the highest tetragonal distortion (c/a = 1.05) was achieved at x = 0.5. From polarized X-ray absorption measurements of the x = 0.5 film, I clearly observed linear dichroism, indicating the difference in site occupancy of nitrogen and oxygen between axial and equatorial sites. Meanwhile, in the $SrTaO_2N$ epitaxial thin film with x = 1, whose tetragonal distortion was small due to lattice relaxation, almost no linear dichroism signal was detected. Electron energy loss spectroscopy combined with transmission electron microscope was conducted on the x = 0.5 film with the highest tetragonal distortion and revealed higher occupation of nitrogen at the axial site than the equatorial one.

As another topic, I investigated electrical transport properties of $SrNbO_{3-x}N_x$ epitaxial thin films, in which the nitrogen content x was systematically changed in order to observe the effect of nitrogen introduction on the filling state of the conduction band composed mainly of 4*d* orbital of Nb. With increasing x, resistivity monotonically increased and the “metallic” transport properties was gradually converted to “semiconducting” ones. Light absorption in near infrared and visible region was also

systematically varied. The change of absorption spectrum in visible light region is understandable by assuming a crossover from intraband transition in the Nb 4*d* orbital to interband one between the valence and conduction bands. These results indicate that anion substitution is also effective to modify the band structure similarly to the cases of widely studied cation substitution. In addition, I found anomalously large positive magnetoresistance in the $SrNbO_{3-x}N_x$ films at low temperature despite their paramagnetic or non-magnetic characteristics. The magnetoresistance was positively dependent on nitrogen content x and $SrNbO_2N$ showed a value as high as 50% at 2 K under 9 T, where strong localization of wave function associated with nitrogen introduction might play a significant role.

In conclusion, I succeeded in strain and chemical engineering in perovskite oxynitride epitaxial thin films. The researches on $SrTaO_2N$ and $Ca_{1-x}Sr_xTaO_2N$ films revealed that it is possible to control anion arrangement artificially by applying external stress and to develop new functionality like ferroelectricity. At the same time, nitrogen introduction is useful to tune the electronic states of transition metal compounds as demonstrated in the study on $SrNbO_{3-x}N_x$. These results indicate that the thin-film based approach is effective to elucidate how nitrogen anions cause unique electrical properties and to seek for new functionality in oxynitride materials, leading to expectation for future electronics based on them.

Acknowledgement

I would like to show my appreciations to all those who have helped me conduct the research related to this thesis.

First of all, I specially thank my supervisor Prof. Tetsuya Hasegawa, for his advice, encouragement and patience. His objective and sharp perspective is always beyond my point of view and has guided me in the direction of my true game. I am also grateful to Dr. Yasushi Hirose, who has provided me tireless support in every moment of this research. His advice is full of fruitful inspirations and has shed light on the issues I faced during the research.

I also owe my doctoral thesis to Dr. Hideyuki Kamisaka. He has made cooperative works of computational calculation and given me a beneficial insight on a core point of this research. Prof. Tomoteru Fukumura has given me many advices based on his deep knowledge and stimulated my curiosity about solid state chemistry. Dr. Akira Chikamatsu has always created friendly and comfortable atmosphere in the laboratory, which should have promoted my research. I have learned many about research especially, experimental techniques, from Mr. Shoichiro Nakao. I am really grateful to them.

I am indebted to my collaborators. Mr. Seiji Ito, Mr. Akira Morita, Prof. Hiroyuki Matsuzaki and Prof. Katsuyuki Fukutani of the University of Tokyo, and Prof. Kimikazu Sasa, Mr. Satoshi Ishii and Prof. Daiichiro Sekiba of University of Tsukuba assisted me to perform nuclear reaction measurements, which is one of the fundamental parts of this thesis. Some of the TEM measurements are conducted by the support of

Prof. Yukio Sato of Kyusyu University and Prof. Yuichi Ikuhara of the University of Tokyo. Dr. Hitoshi Morita of Bruker AXS assisted the high temperature XRD measurements.

I would like to send my sincere thanks to Mr. Kei Shigematsu and Mr. Tomoo Terasawa. They entered Hasegawa laboratory together with me when we were bachelor students. They have provided me a lot of supports not only in the research but also in the daily life. I really feel fortunate to have spent my student life with them.

I would like to show my acknowledgement to the members of Hasegawa laboratory. KAST members, Dr. Sohei Okazaki, Dr. Chang Yang, Dr. Youngok Park, Mr. Atsushi Suzuki, Mr. Kazuki Aizawa, Mr. Kenta Shimamoto, Mr. Masahito Sano, Mr. Jumpei Takahashi, Mr. Vitchaphol Motaneeyachart, Mr. Takanori Yamazaki and Naoki Kashiwa have provided me a comfortable environment to conduct my research. Hongo members, Dr. Daisuke Ogawa, Mrs. Anri Watanabe, Mr. Jie. Wei, Mr. Shungo Kojima, Mr. Tsukasa Katayama, Ms. Thantip. S. Krasienapibal, Mr. Jeon Il, Ms. Xi Shen, Mr. Shun Inoue, Ms. Mayuko Oka, Mr. Ryosuke Sei, Ms. Kaori Kurita, Mr. Ryosuke Takagi, Mr. Tomoya Onozuka, Mr. Kenichi Kaminaga, Mr. Kyohei Yamatake, Mr. Keisuke Kawahara, Mr. Yuji Kurauchi, Mr. Ryota Kantake, Mr. Fahd S. Kahn, Mr. Yutaka Uchida, Mr. Dai Kutsuzawa, Mr Takuma Takeda, Mr. Shunsuke Shibata, Mr. Naoaki Hashimoto and Keisuke Yamada, I have enjoyed to interact with them. I must thank to the secretaries of Hasegawa laboratory, Mrs. Mie Umino, Mrs. Aya Imoji, Mrs. Mayuko Kikuchi and Mrs. Miki Komazawa.

Finally I would like to show my appreciation to my family for giving me the opportunity to learn in Hasegawa laboratory.

Contents

Chapter 1

General introduction

1.1 Backgrounds

Perovskite oxide is a material group with a composition of ABO_3 and its basic structure is shown in Figure 1. In this half century, the material group has been extensively studied to develop new functionalities because of its wide range of physical properties arising from the flexibility in chemical composition and crystal structure [1].

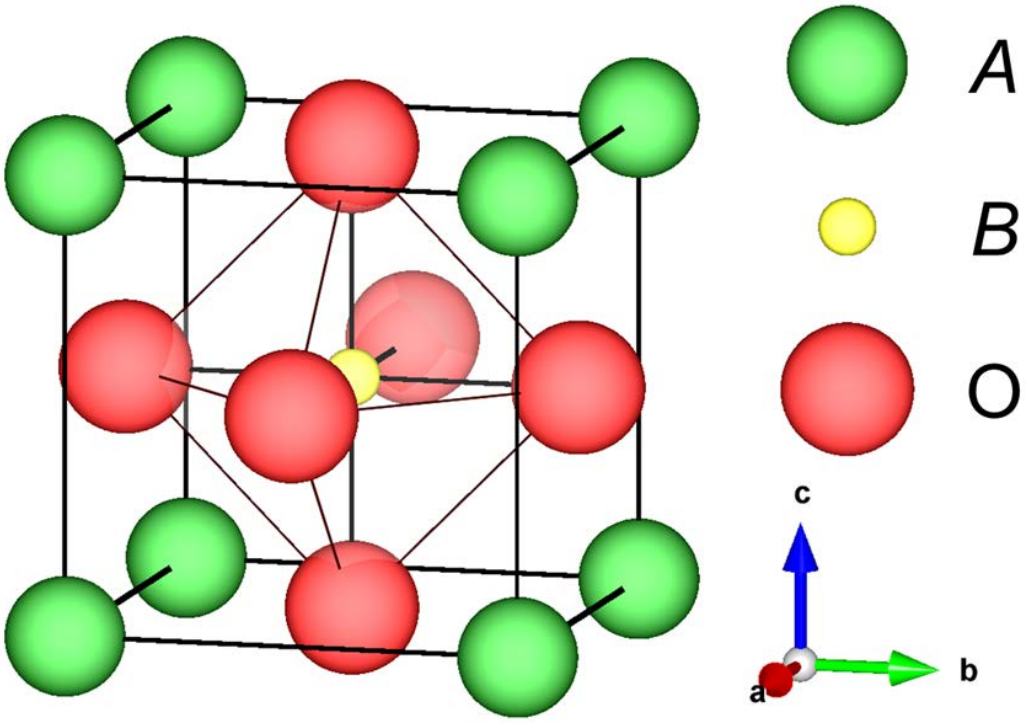

Figure 1. Formula unit of perovskite oxide ABO_3.

One of the successful ways to modify the properties is chemical substitution of component elements at *A* and/or *B* cation sites. For example, $Pb(Zr,Ti)O_3$ is a practical ferroelectric material [2], $(La,Sr)MnO_3$ exhibits ferromagnetism together with metallic electrical conductivity [3], $(Li,La)TiO_3$ is a good candidate for Li ion conducting solid electrolytes [4] and $Ba(Pb,Bi)O_3$ is a superconducting material with a relatively high transition temperature [5].

In contrast to the varieties of cations to be introduced to *A* and *B* sites, anions that can occupy the oxygen site are very limited: Considering ionic sizes, O^{2-}, H^-, N^{3-} and F^- are the only single-element anions that can be substituted for oxide ions. If one introduces the other anionic species like halogens other than fluorine into oxides, they occupy independent sites and tend to change the crystal structure into layered ones.

Furthermore, it has been difficult to prepare oxide-based mixed-anion systems until a few decades ago because oxides are usually the most stable phases in the air. That is, anion-substituted oxides are generally metastable and require precise control of their synthesis conditions. Recent progress in synthetic technique has radically changed the situation and provided an increasing number of studies on oxide-based mixed-anion systems. Anion substitution has sometimes provided unique functionalities which are difficult to achieve with cation substitution. For example, H^- doping in perovskite $BaTiO_3$, which was recently achieved via a topotactic synthesis, was found to trigger the insulator to metal transition, which had never been reported in cation substituted $BaTiO_3$ [6].

Perovskite oxynitride $AB(O,N)_3$, which contains both oxygen and nitrogen in their anion sites, is a representative of anion-mixed perovskites and expected to be a group of next-generation functional materials. Especially, their optical properties are

gaining much attention because of their visible light activity, which is rarely seen in simple oxide materials [7, 8]. Indeed, perovskite oxynitrides has been widely accepted as promising visible light active photocatalysts despite the short history of the studies [9, 10].

Perovskite oxynitrides also have a potential as noble electrical materials because nitrogen introduction affects both crystal structure and electronic state of the mother compounds, which are generally fundamental factors that govern the intrinsic electrical properties of materials.

From a structural viewpoint, partial substitution on oxygen with nitrogen raises two possible formula unit structures. In case of ABO_2N composition, nitrogen can arrange in *cis*- and *trans*-type manners as shown in Figure 2. In a macroscopic view, ordering and disordering of nitrogen ions govern the symmetry of crystal system and

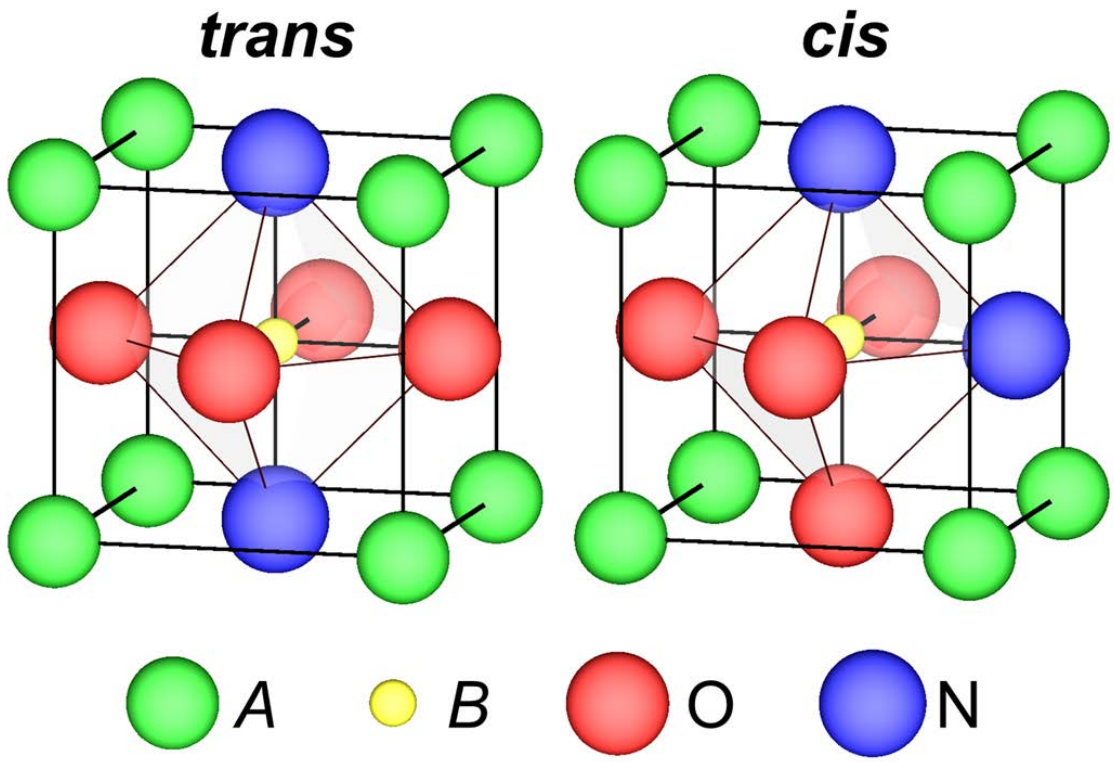

Figure 2. *trans*- and *cis*-type formula unit of perovskite oxynitride ABO_2N.

band structure and hence determine the polarity.

Several influences on electronic state are also expected due to the differences in electronic characteristic between nitrogen and oxygen: 1) Nitride ion works as acceptor because it has larger negative formal charge than oxide ion by one. Thus, the valence state of the component cations can be controlled by changing nitrogen concentration. 2) The larger charge of nitride ions than oxide ions provides local dipole moment. 3) Nitrogen has larger covalency compared to oxygen and nitrogen-metal and oxygen-metal bonds behave differently. This affects bond lengths and causes distortion, rotation and/or tilting of crystalline lattice.

One attractive example of the unique electrical properties reported on perovskite oxynitrides is high dielectric constants of $BaTaO_2N$ and $SrTaO_2N$ [11]. Their dielectric constant values have been reported to be of the order of 10^3 despite they do not have net spontaneous polarization. Researchers have been discussing the origin of the unique dielectric properties of $BaTaO_2N$ and $SrTaO_2N$ taking both local bonding states [12] and anion arrangement [13] into consideration though full understanding has not been achieved.

Despite strong expectation for perovskite oxynitrides as new functional materials, only a limited number of studies have been conducted on their electrical properties so far. This is because the conventional synthesis method called ammonolysis includes several challenges: 1) The method is applicable only to powder form samples in order to complete the reaction between precursor oxide materials and reactant gaseous ammonia. The resulting oxynitride specimens contain too many grain boundaries and air gaps which tend to cause unexpected extrinsic influences on electrical measurement, although considerable efforts have been made to reduce the

defects and to improve the density of the oxynitride samples. 2) Because the reaction is kinetic, systematic tuning on anion arrangement and chemical composition is difficult, preventing us from understanding the influence of nitrogen introduction on the electrical properties of perovskite oxynitrides.

1.2 Overall objective of this study

As mentioned in the previous section, it is difficult to conduct reliable electrical measurements on bulk perovskite oxynitride samples with the conventional techniques developed so far. In the history of materials science, researchers have faced similar challenges even in the field of pure oxides and other semiconductor materials.

Epitaxial growth of thin films is one of the highly established techniques to break through such situations. In the technique, it is possible to synthesize objective materials in single crystalline form, which is most suitable for electrical evaluation, with the aid of template of single crystals. In addition, epitaxial stress caused by lattice mismatch between film and substrate is sometimes useful to control the crystal structure of film materials. Anion arrangement in perovskite oxynitrides can also be affected by such external stress. Although several attempts for epitaxial growth of perovskite oxynitrides have been reported [14–18], the quality of the obtained films was much worse than those of oxide films. This is mainly because the technique to efficiently introduce nitrogen into thin films has not been established yet.

The purpose of this study is to understand the role of nitrogen ions in the electrical properties of perovskite oxynitrides and to develop new functionalities based

on the materials group using the technique of heteroepitaxy. I adopted nitrogen plasma assisted pulsed laser deposition (NPA-PLD) method to grow perovskite oxynitride thin films. Oxides were used as starting materials (targets) and nitrogen was introduced as reactant gas in the form of plasma, which has much higher reactivity than molecular N_2. Growth conditions were optimized through the synthesis of model systems, $SrTaO_2N$ and $CaTaO_2N$. The technique was further expanded to seek for the way to develop novel functionalities in oxynitrides. Firstly, ferroelectricity of $SrTaO_2N$ was investigated from the viewpoint of nitrogen arrangement in the TaO_4N_2 octahedral structure. Next, artificial control of anion arrangement was demonstrated in $Ca_{1-x}Sr_xTaO_2N$ thin films based on the results of the above-mentioned study. As another topic, I examined the function of nitrogen ion as an electron acceptor due to its larger negative charge (−3) than oxygen ion (−2) and performed filling control of conduction band of $SrNbO_{3-x}N_x$ by varying nitrogen content x in a systematic manner.

Chapter 2

Perovskite Oxynitride

2.1 Introduction

The history of study on perovskite oxynitrides is less than 30 years. Marchand *et al* reported the first synthesis of perovskite oxynitrides in 1986 [19]. In 1990s, cation-mixed perovskite oxides with special ordering of ions, so-called double perovskite oxides, began to be studied intensively because they were figured out to possess exclusive physical properties which are inaccessible with simple perovskite oxides [20]. Following them, some researchers started detailed investigations on synthesis method, crystal structure and optical and electrical properties of perovskite oxynitrides around 2000. By far, many kinds of perovskite oxynitrides with various *A* and *B* cations have been synthesized and examined. Tables 1 and 2 summarize the past researches from the viewpoint of synthesis method, specimen forms and physical properties. In this chapter, more detailed information than the tables will be reviewed to help our perspective understanding of the current situation of the studies on perovskite oxynitrides and to clarify concrete issues to be solved. In the end, I will mention the strategy of this study.

Table 1. Perovskite oxynitrides synthesized in bulk form

Composition	Synthesis method	Sample form	Physical property	Reference
$BaTaO_2N$	Ammonolysis High temperature synthesis [23] Urea-based route [26]	Powder	High dielectric constant (> 4000) [11] Band gap = 1.8 eV [11], 2.0 eV [29] Photocatalysis (H_2 evolution) [25]	[8][11][19] [21–29]
$SrTaO_2N$	Ammonolysis Microwave induced plasma reactions [9] High temperature synthesis [23] Urea-based route [26] Ammonolysis on oxide single crystal [31]	Powder Single-crystal [31]	High dielectric constant (> 2000) [11], (>1000) [35] Band gap = 2.2 eV [11], 2.06 or 2.10 eV [36] Photocatalysis (H_2 evolution) [25]	[8][9][11] [24–26] [29][30–36]
$CaTaO_2N$	Ammonolysis High temperature synthesis [23] Urea-based route [26]	Powder	Low dielectric constant (~ 30) [11] Band gap = 2.4 eV [11][36], 2.6 eV [29] Photocatalysis (H_2 evolution) [25]	[8][11][24–26][29][30] [36]
$BaNbO_2N$	Ammonolysis Urea-based route [26]	Powder	Band gap = 1.8 eV [11]	[8][11][19] [21][24][26] [27]
$SrNbO_2N$	Ammonolysis Microwave induced plasma reactions [9] High temperature synthesis [23] Urea-based route [26] Ammonolysis on oxide single crystal [31]	Powder Single-crystal [31]	Band gap = 1.9 eV [11] Photoanode for water splitting [37]	[8][9][11] [24][26][31] [32][37]
$CaNbO_2N$	Ammonolysis	Powder	Band gap = 2.1 eV [11] Photocatalysis (water) [38]	[11][24][38]
$LaTiO_2N$	Ammonolysis Ammonolysis on oxide single crystal [9] Urea-based route [26] Microwave induced plasma reactions [31]	Powder Single-crystal [9]	Band gap = 2.1 eV [10] Photocatalysis (water) [10]	[8–10] [26][31] [39–41]
$LaTi(O,N)_3$	Ammonolysis	Powder	Band gap = 2.28–2.60 eV [14] Photocatalysis (acetone) [14]	[14]

Table 1. Perovskite oxynitrides synthesized in bulk form (continued).

Composition	Synthesis method	Sample form	Physical property	Reference
$LaTaON_2$	Ammonolysis	Powder	Band gap = 1.84 or 1.88 eV [35]	[30][36][42]
$LaNbON_2$	Ammonolysis	Powder	Band gap = 1.7 eV	[43]
$SrMoO_{3-x}N_x$ ($x > 1$)	Ammonolysis	Powder	*p*-type conductor	[44]
$SrMoO_2N$	Ammonolysis	Powder	*p*-type conductor (Semiconductive) Anomaly in magnetism (T_C ~ 54K)	[45]
$SrMoO_{2.5}N_{0.5}$	Ammonolysis	Powder	Spin glass at low temperature Metalic conductivity	[46]
$SrMoO_{2.6}N_{0.4}$	Ammonolysis	Powder		[47]
$SrMoO_{3-x}N_x$	Urea-based route	Powder		[26]
$SrWO_2N$	Ammonolysis	Powder	Pauli paramagnetism Semiconducting conducitivity	[46]
$EuWO_{3-x}N_x$	Ammonolysis	Powder	Ferromagnetism Colossal magnetoresistance	[48][49]
$EuNbO_2N$	Ammonolysis	Powder	Ferromagnetism (T_C = 5.2 K) Colossal magnetoresistance	[50]
$BaMo(O,N)_3$	Ammonolysis	Powder		[51]
$BaSc_{0.05}Ta_{0.95}O_{2.1}N_{0.9}$	Ammonolysis	Powder	High dielectric contant (~ 7300) Band gap = 1.8 eV	[52]
$BaZr_xTa_{1-x}O_{2+x}N_{1-x}$	Ammonolysis	Powder	Photocatalysis (water) [53]	[53][54]
$Ca_{0.25}La_{0.75}TiO_{2.25}N_{0.75}$	Ammonolysis	Powder	Band gap = 2.0 eV Photocatalysis (water)	[10]
$Ca_{1-x}La_xTaO_{2-x}N_{1+x}$	Ammonolysis	Powder	Absorption edge = 2.00–2.75 eV	[7]

Table 1. Perovskite oxynitrides synthesized in bulk form (continued).

Composition	Synthesis method	Sample form	Physical property	Reference
$CaMoO_{1.7}N_{1.3}$	Ammonolysis	Powder		[51]
$CaZr_xTa_{1-x}O_{2+x}N_{1-x}$	Ammonolysis	Powder		[53]
$GaZr_{0.5}Ta_{0.5}O_{2.5}N_{0.5}$	Ammonolysis	Powder		[8]
$La_{1-x}Ba_xTi(O,N)_3$	Ammonolysis	Powder		[55]
$La_{1-x}Ca_xTiO_{2+x}N_{1-x}$	Ammonolysis	Powder	Band gap = 2.23–3.72 eV	[56]
$La_{1-x}Sr_xTi(O,N)_3$	Ammonolysis	Powder	Band gap = 1.96–3.31 eV)	[55]
$LaMg_{1/2}Ta_{1/2}O_{5/2}N_{1/2}$	Ammonolysis	Powder	Low dielectric contant (~ 150) Band gap = 1.9 eV	[52]
$LaMg_{1/3}Ta_{2/3}O_2N$	Ammonolysis	Powder	Low dielectric contant (~ 120) Band gap = 1.9 eV	[52]
$LaZrO_2N$	Ammonolysis	Powder		[39]
$LnNbON_{2-\delta}$ (Ln = La, Nd, Pr)	Ammonolysis	Powder		[57]
$NdTiO_2N$	Ammonolysis	Powder		[39]
$NdVO_2N$	Ammonolysis	Powder	Pauli paramagnetism Weak antiferromagnetic interaction	[58]
$NdZrO_2N$	High pressure synthesis	Powder		[59]
$PrTaON_2$	Ammonolysis	Powder	Band gap = 2.0 eV	[29]
$PrZrO_2N$	High pressure synthesis	Powder		[59]
$SmZrO_2N$	High pressure synthesis	Powder		[59]
$SrZr_xTa_{1-x}O_{2+x}N_{1-x}$	Ammonolysis	Powder		[53]

Table 2. Perovskite oxynitrides synthesized in thin film form.

Composition	Synthesis method	Sample form	Physical property	Reference
$(La,Sr)Ti(O,N)_3$	Ammonolusis on oxide films	Thin film	Band gap = 2.31–3.1 eV [59]	[14][60]
$BaTaO_2N$	PLD	Epitaxial thin film	$\varepsilon' = 200–240$, $\tan\delta = 0.001\sim0.2$	[61]
$LaTiO_2N$	RF sputtering	Thin film [62] Epitaxial thin film [63]	$\varepsilon' = 170$ $\tan\delta = 0.7$ tunability = 72% $\varepsilon' = 350$ $\tan\delta = 0.3$ tunability = 57 % [62] $\varepsilon' = 375$ $\tan\delta = 1$ [63]	[62][63]
$LaTi(O,N)_3$	RF sputtering [15,16,64,65] PRCLA [18] NH_3 plasma treatment on oxide film [66]	Thin film [16][18] [64][66] Epitaxial thin film [15][65]	$\varepsilon' = 615$ $\tan\delta = 0.060$ [16] Band gap = 2.6–3.7 eV [64], 2.20–3.45 eV [16], 2.05–2.35 eV [65], 2.36–2.95 eV [18] Photocurrent [65] Semiconducting conductivity [66]	[15,16,18, 64–66]
$LaTi_{0.9}Nb_{0.1}(O,N)_3$	NH_3 plasma treatment on oxide film	Thin film	Semiconductive conductivity	[66]
$LaTi_{0.9}Ta_{0.1}(O,N)_3$	NH_3 plasma treatment on oxide film	Thin film	Semiconductive conductivity	[66]
$Sr_{0.75}La_{0.25}TiO_{2.75}N_{0.25}$	Ammonolysis on oxide film	Thin film		[31]
$SrMoO_{3-x}N_x$	PLD	Epitaxial thin film	Metalic conduction	[17]

2.2 Synthesis

In the past researches on perovskite oxynitrides, the specimens have been prepared mainly in two kinds of forms: bulk powders and films. Bulk samples are appropriate for structural investigations because neutron diffraction technique is applicable to them. On the other hand, films have some merits such as capability of electrical property measurements. This section will review the techniques and issues concerning sample preparation within the category of bulk and film form.

2.2.1 Bulk synthesis

The perovskite oxynitride specimens prepared so far are mostly in bulk powder form. As for the preparation of the powders, the method called ammonolysis has been generally used [9,67]. In the method, nitrogen atoms replace the oxygen ones in the precursor oxides under NH_3 gas flow at high temperature around 1000 ℃.

While ammonolysis has allowed successful syntheses of considerable kinds of perovskite oxynitrides, it always requires careful control of reaction conditions to obtain homogeneous and phase-pure specimens. Followings are the general challenges recognized in the synthesis of perovskite oxynitrides: 1) Oxynitrides are typically less stable than oxides composed of the same cation species, especially in the air ambient, and hard to form; 2) There are mainly two rate-limiting steps in ammonolysis. One is the exchange process of atoms between solids and gaseous atmosphere. The other is the diffusion of nitrogen atoms in the solid phases as widely seen in solid state reactions. Through a great number of synthetic works, key factors determining whether perovskite oxynitrides are successfully form under a certain reaction condition have been revealed

as follows:

a) Stabilization of nitriding process [68]

The first challenge can be depicted by the following reaction equation in the case of composition of ABO_2N:

$$\frac{1}{2}A_2B_2O_7 + \frac{1}{2}N_2 \rightarrow ABO_2N \quad (2.1)$$

$$\Delta G_0 > 0 \quad (2.2)$$

ΔG_0 is the Gibbs free energy of the reaction. In order to set the reaction forward from left to right, stabilization of the whole reaction system with side reactions is necessary. In this viewpoint, NH_3 is one of the most suitable nitriding agents because it forms thermodynamically stable H_2O at the same time as the provision of nitrogen. This can be described by the following equations:

$$\frac{1}{2}A_2B_2O_7 + NH_3 \rightarrow ABO_2N + \frac{3}{2}H_2O \quad (2.3)$$

$$\Delta G_f = \Delta G_0 + \frac{3}{2}\Delta G_{H_2O} - \Delta G_{NH_3} \quad (2.4)$$

ΔG_f is the Gibbs free energy of the reaction, and ΔG_{H_2O} and ΔG_{NH_3} are the Gibbs formation energy of H_2O and NH_3, respectively. If the value of ΔG_f is negative, the oxynitride ABO_2N may be generated. This stabilization of the reaction explains why ammonolysis is preferable to synthesize perovskite oxynitrides. Contrastively to the reactivity of NH_3, mixture of N_2 and H_2 is reported to be not effective to promote nitriding reactions because of the too strong triple bond in a nitrogen molecule.

Another candidate for efficient nitriding agents is microwave induced

plasma (MIP) including nitrogen. Ebbinghaus *et al*. demonstrated synthesis of perovskite oxynitrides with MIP of ammonia [9]. Advantage of this synthesis method is substantial shortening of reaction time. It took 2 hours to complete the nitriding reaction with MIP plasma while 1 day reaction is necessary in usual ammonolysis in the case of $LaTiO_2N$.

b) Synthesis condition

Needless to say, control of synthesis conditions is crucial in chemical reactions including ammonolysis. From the viewpoint of set-up of the reaction, rotating tube furnace has been revealed to be convenient to enhance the exchange rate of atoms between solids and gas [9]. Rotation of the reaction system is effective to obtain homogenous products, as well.

Artificially variable parameters in ammonolysis are temperature, NH_3 flow-rate and reaction time. Though high temperature around 1000 ˚C is required to promote the diffusion of nitrogen in solids, NH_3 decomposes into unreactive N_2 and H_2 under such condition [9]. Construction of non-equilibrium condition by flowing NH_3 gas is, thus, necessary to realize reaction between the solids and high temperature ammonia. Reaction time must be set at an appropriate value depending on the other conditions. If the time is too short, reaction cannot be completed, whereas too long reaction time sometimes results in the formation of nitride impurities.

While ammonolysis is typically conducted around 1000 ˚C, higher temperature, 1500 ˚C, sometimes enables synthesis of perovskite oxynitrides not in NH_3 but in N_2 atmosphere [23]. In this case, the starting material is a mixture of alkaline metal oxide and transition metal oxynitride prepared with ammonolysis

beforehand.

c) Electronegativity of cations

Even if one completely tunes the conditions of ammonolysis synthesis of perovskite oxynitride, whether the reaction is successful ultimately depends on the kind of cation species in *A* and *B* sites.

Elder *et al*. investigated thermodynamic data of oxides and nitrides and proposed an empirical law to predict the results of ammonolysis nitriding reactions [68]. Though this study aimed at examining the feasibility of synthesis of ternary nitrides from ternary oxides, the proposed law is useful also for judging the availability of oxynitride compounds through ammonolysis.

One of the conclusions of the research is that the less electronegative the component cations are, the more likely nitrides and/or oxynitrides are to be formed. For example, perovskite oxynitrides including titanium in their *B* site are more easily synthesized than those including zirconium as reported by Clarke *et al* [39].

Besides electronegativity of ions, the valence state of cations is also crucial for procession of nitriding reaction. Because of the existence of a certain amount of H_2 gas generated from ammonia under ammonolysis, the nitriding reaction usually progresses in a highly reductive condition. This makes it difficult to artificially control the valence state of cations, and the *B*-site cations are mostly limited to those possessing no *d* electrons (so called d^0 ions) like Ta^{5+}, Nb^{5+} and Ti^{4+}. Recent improvement in synthetic technique, nevertheless, enabled synthesis of $NdVO_2N$ including vanadium ion with d^1 state [58].

d) Precursor

The choice of precursors is a significant issue when we conduct nitriding reactions because they directly affect the energy difference between the left- and right-hand sides of the chemical reactions and the probability of atomic diffusion and determine the final products. Precursors for perovskite oxynitride $ABO_{3-x}N_x$ can be categorized into mainly two types. One is stoichiometric mixture of two compound species including *A* and *B* cations, respectively. The other is a single compound composed of *A* and *B* cations and oxygen, which is so-called ternary oxide.

In the case that formation of oxynitrides is started from two species, binary oxides (AO_y and BO_z) or carbonates ($A(CO_3)_y$) are available. These compounds are commercially available and easily accessed. Carbonates can have advantage to promote the nitriding reactions because they release CO_2 as a reactant which can reduce the total formation energy of the reactions like in the case of H_2O formation from NH_3.

A merit to use ternary oxides as precursors is reduction of diffusion steps of the cations during the nitriding reactions [68]. This can result in the reduction of processing temperature and sometimes makes it possible to obtain unstable oxynitrides which decompose at high temperature. Furthermore, reduction of diffusion steps of NH_3 gas and/or nitrogen atoms is also expected in the precursors because most ternary oxides possess perovskite related crystal structure with excess oxygen layers where the nitrogen sources can pass with small friction energy [36]. This similarity in crystal structure between the precursors and resulting perovskite oxynitrides, in some cases, enables topotactical reaction of single crystals although the reaction tends to stop at the surface region with several

micrometers in thickness [31].

While ternary oxides created with conventional solid state reactions have crystalline form, soft chemistry processes can provide amorphous phase, which is another alternative of precursors [24,33–35,40,43,56]. Their unstable chemical bonds and uniform composition in atomic scale make diffusion of atoms faster and are helpful to prepare oxynitrides, even if the included cations have low electronegativity. Clarke *et al.*, for instance, used an amorphous precursor to synthesize perovskite oxynitrides including Zr at *B* site which is hard to be formed from crystalized precursors [39]. Furthermore, perovskite oxynitrides created from amorphous are expected to be more suitable for photocatalysts compared to those created from crystal precursors, because they tend to show porous structure with high surface area which provides much higher opportunity of reactions between the solids and liquids (or gases) to be decomposed [9].

Not only precursors themselves but also additives are effective to control diffusion of atoms in solids. Chloride mineralizers such as NaCl, KCl, NH_4Cl and $CaCl_2$ are reported to be especially practical to reduce the temperature of the nitriding reactions [36,24,33,40,43,56,42]. This is because these chemicals work as flux and enhance the diffusion of both cations and anions, which move much faster in molten medium than in solids. It is, in addition, known that some sintering additives help high densification of oxynitride materials, which is helpful for electrical measurements [34].

Though the synthesis methods of perovskite oxynitride specimens have been gradually improved, they still lack precise controllability on sample configuration. As

for structure of perovskite oxynitrides, it is known that the synthetic procedure affect anion arrangement, which will be reviewed in more detail later on. However, the key factor to change anion arrangement is unclear. Electrical measurements usually require highly dense specimens, but it is difficult to prepare sufficiently dense bulk samples of oxynitrides. Though the use of the additives improves the density of the samples to some degree, the problem still remains.

2.2.2 Film synthesis

Thin films with nanometer to micrometer thickness have become a basis of modern technology due to the requirement of small size in electronic devices. They are useful even in the field of basic research because of a number of merits including down-sizing capability, high density, easiness of shaping, etc. Especially, epitaxial growth technique is very attractive for both basic research and applications because single crystalline films with a certain orientation matching to substrate can be obtained. The structural stabilization by stress from substrate in epitaxy is effective for synthesis of metastable phases and accurate measurement of physical properties, where crystallographic planes are well defined and thus the mechanisms of observed phenomena can be discussed in detail.

Thin films of perovskite oxynitrides have been studied since around 2005 though the number of the reports is still very small. While the motivation of these studies is mainly to measure the physical properties of perovskite oxynitrides, they had to develop techniques to grow oxynitride thin films because oxynitride films cannot be formed at the similar condition as oxide ones.

Aguiar *et al*. reported two-step growth on thin films of perovskite oxynitride

$(La,Sr)Ti(O,N)_3$ [14,60]. They firstly deposited thin films of precursor oxide $(La,Sr)TiO_3$ using a solution process or pulsed laser deposition (PLD). The films were subsequently annealed in ammonia and nitrided. Formation of oxynitride films with perovskite structures was confirmed in various composition of the *A* site cations. However, the films had some problems in quality including crystal orientation, chemical composition and surface roughness. The measured resistivity of the films was not very reasonable and clearly needed improvement in quality.

French groups reported film growth of $LaTiO_2N$ with radio frequency magnetron sputtering [15,16,62–65]. One of the biggest advantages of sputtering is that nitrogen gas can be activated by plasma and they reported that the nitrogen content in the films can be controlled by changing the fraction of nitrogen in the ambient of Ar/N_2. Under certain conditions, the films were grown epitaxially on single crystal substrates of $SrTiO_3$ [15,63,65]. However sputtering technique generally has a problem that the films suffer from damages by highly activated atoms in the atmosphere. Indeed the measured tan δ values of the films in dielectric measurements were higher than 0.06, which indicates that large leakage current flows in the films during the measurements.

PLD is a widely used technique to grow films of oxides and semiconductors in basic research because of the easiness in preparing starting materials (targets), which allows researchers to change the film composition in a flexible manner and to obtain high quality films under a properly tuned condition. While oxygen gas is usually supplied for the growth of oxide films, some modifications on the process have been made for the synthesis of oxynitride films.

Kim *et al*. reported growth of $BaTaO_2N$ thin films with PLD [60]. They used $BaTaO_2N$ ceramics as a target and introduced mixed gas of N_2 and O_2 with the ratio of

20:1 during the film deposition. The films grew epitaxially on the (100) planes of MgO and $SrRuO_3$ buffered $SrTiO_3$ single crystalline substrates. The crystallinity of the films was much better than the films prepared with other techniques and allowed observation on lattice structure with transmission electron microscopy. However, the film contained structural defects which prevented reliable measurements for the high dielectric constant values as observed in the bulk specimens.

Lekshmi *et al*. reported preparation of $SrMoO_{3-x}N_x$ epitaxial thin films on $LaAlO_3$ single crystal substrates [17]. Nitrogen was introduced to the film up to $x = 0.6$ from ammonia gas supplied during the film deposition even despite they used oxide, $SrMoO_3$, as a target. This is probably because of high electro-negativity of Mo.

Marozau *et al*. reported synthesis of $LaTiO_{3-x}N_x$ films with pulsed reactive crossed beam laser ablation (PRCLA), one of the modified PLD methods, using corresponding oxide targets [18]. In the method, gas pulses are supplied in the configuration that they cross the plume ablated from the targets by laser [69,70]. Because the gas pulses are synchronized with the laser pulse in this technique, even inert gas like nitrogen can react with the materials in plume. They tried both NH_3 and N_2 as reaction gas. Though NH_3 showed higher reactivity, N_2 was able to be incorporated in the films in some degree. The ability to cause reaction between oxide starting materials and nitrogen gas is very advantageous because it allows precise control of nitrogen content in the films by tuning variable parameters and excess reduction by H_2 created by decomposition of NH_3 can be avoided. In addition, cation composition can be flexibly changed in a wide range because oxide targets can be prepared using conventional solid state reaction in most cases. Growth of perovskite oxynitride epitaxial thin films with PRCLA still requires improvement because the films

contained some differently oriented crystals and the nitrogen content *x* did not reach to 1 in the report.

Another way to activate inert gas is using a plasma source. The group who reported film growth by PRCLA also attempted synthesis of nitrogen doped $SrTiO_3$ films by nitrogen plasma assisted PLD (NPA-PLD) technique [71]. Though the nitrogen amount was less than 1 at% because of the limitation associated with charge neutrality, nitrogen was successfully introduced to the films from both N_2 and NH_3 plasma.

It is difficult to construct systematic outlook on the film growth of perovskite oxynitride under the current circumstance because there have been a limited number of reports. However, the issues to be solved can be summarized into two: 1) Difficulty in controlling composition and 2) poor crystallinitiy of the oxynitride films. Because nitrogen is easily released from samples as molecular nitrogen during film growth process, it is necessary to seek for ways to “confine” nitrogen in the films. In addition, we need to choose a proper technique and film growth condition to improve crystallinity especially in basic researches which focus on the detailed analysis of crystal structure and electrical properties.

2.3 Crystal structure

Crystal structure is a foundation that governs electrical properties in crystalline systems because it determines the electronic structure in **k** space and ideal (intrinsic) physical properties. As for transition metal oxides, researchers have investigated and found close relationship between lattice structure, including bond distance between

metals and oxygen anions, bond angle in *X*-metal-*X*-metal-⋯ chain and total symmetry of crystal, and physical properties.

It is easy to understand that the presence of two different species at the same sites of crystal reduce the number of symmetric operations. Moreover, the two different ionic species have difference in bonding natures including ionic size and covalency so that the crystal structures of mixed ion compounds like oxynitrides are sometimes very complicated and have been investigated with great interest. In this section past researches on the crystal structures of perovskite oxynitrides will be reviewed.

2.3.1 Perovskite structure

A basic unit of ideal perovskite structure is a cube form with *A* cations at the corners, *B* cation at the body center and *X* anions at the face centers (Fig. 1). In this structure, we can see an octahedral coordination between *B* cation and surrounding six *X* anions. In cases of oxides (i.e. *X* = O), *A* site is mostly occupied with an alkaline earth metal or lanthanoid, while a transition metal often occupies *B* sites.

Perovskite structure can be distorted in reality based on the balance between the sizes of component ions. This sometimes results in deviation of crystal system from the ideal cubic into others. Tolerance factor τ, defined by the formula described below, is an effective measure to understand the relationship between stability of perovskite-type setting and ionic sizes.

$$\tau = \frac{(r_A + r_X)}{\sqrt{2}(r_B + r_X)} \tag{2.5}$$

where r_A, r_B and r_X are the ionic radii of *A*, *B* and *X* ions, respectively. In an ideal case that the ionic sizes are well balanced, the value of τ is unity and the crystal system is

cubic. $SrTiO_3$ is a good example of cubic perovskite with τ equal to 1.002 and space group of $Pm\bar{3}m$. It is empirically known that cubic perovskite structure is allowed if the deviation of τ from unity is less than 0.1. If r_A becomes large relatively to r_B, τ increases. This situation makes a larger space inside the *A* cation cubes and *X*-*B*-*X* bonds elongates to a certain direction. The resulting crystal symmetry is referred to as tetragonal, in which the *c*-axis length is elongated as can be seen in $BaTiO_3$. Oppositely, small r_A, i.e., τ less than 1, results in orthorhombic or rhombohedral structures. In this case, the symmetry lowering is responsible for tilting (including rotations) of BX_6 octahedral structure.

The octahedral tilting at low τ has some patterns and they can be classified using Glazer notation, which is named after the researcher who developed [72]. In the notation, a pseudo-cubic structure with the space group of $Pm\bar{3}m$ is firstly assumed in every case even if the real structure is somehow deviated from cubic. Then, all tilting manners can be described as $a^{\#}b^{\#}c^{\#}$ in which each characters is responsible for rotations around an axis of the assumed pseudo-cubic cell. Difference in the character means the degree of tilting is not isotropic. Two possible directions of each tilting are described with signs of + and –, respectively, and are put at the superscript #. If an axis does not show tilting, the sign is 0. Howard and Stokes analyzed possible tilting in ABX_3-type perovskite structure based on group theory and found that only 15 patterns are possible and can be related in a group-subgroup manner between which first order transition is allowed [73]. For example, $GdFeO_3$ has octahedral tilting described as $a^+b^-b^-$ and space group of *Pnma*. In this situation, a basic ABO_3 unit is no longer a crystallographic primitive cell and $\sqrt{2}\times\sqrt{2}\times 2$ unit is usually taken as a unit cell.

When we consider local octahedral structure, the symmetry must be lowered by partial introduction of nitrogen into the anion sites. This is because nitrogen causes inequivalent sets of *X*-*B*-*X* units. In case of ABO_2N type perovskite oxynitrides, *cis*- and *trans*-type arrangements are possible for an octahedral unit. In both cases there are at least two inequivalent *X*-*B*-*X* units. All of three *X*-*B*-*X* units can be inequivalent if distortion and/or tilting of the octahedron are taken into account.

Local symmetry of octahedral structures is averaged out when they arrange in a statistical manner and the total symmetry becomes higher than local one. On the other hand, if the octahedral units order, the symmetry of entire crystal reflects the symmetry of each unit and/or ordering.

Attfield extended the classification of octahedral tilting in ABX_3 perovskites to ABX_3, ABX_2X' and $ABXX'X''$ perovskites and reported additional 4 patterns (i.e. 19 patterns in total) [74]. Note that this classification can be used to describe the averaged structures and local symmetry might be lower than them.

2.3.2 Experimental investigation

The most conventional method to evaluate averaged crystal structure is X-ray diffraction (XRD). XRD has been widely adopted to investigate the structures of perovskite oxynitrides since the first report by Marchand *et al* [19], and provided information about their symmetry and lattice constants. However, XRD is not very effective to characterize detailed structures including anion arrangement in oxynitride materials because oxygen and nitrogen have very similar atomic form factor with respect to X-ray and are almost impossible to be distinguished. Thus, neutron diffraction method has been frequently used to detect the distribution of the anions due to the large

difference in scattering length between oxygen (5.803 fm) and nitrogen (9.360 fm). Considerable numbers of neutron diffraction studies for structural refinement of perovskite oxynitrides have revealed general tendencies together with some exceptions.

Firstly it has been unraveled that anion arrangement and resulting crystal symmetry in perovskite oxynitrides is dependent on synthesis conditions including starting materials, process temperature and reaction time and additive fluxes, etc. For example, variations in space group and anion distribution have been reported in the system of $LaTiO_2N$.

Yashima *et al*. reported preparation of samples of $LaTiO_2N$ with flux method [41]. They obtained specimens with high crystallinity and determined their space group as *Imma* through neutron refinement. In *Imma* space group, there are two inequivalent anion sites, 4*e* and 8*g*, and the both sites were occupied with the two anions with almost perfectly statistical probability (i.e. O/N = 2). This means that the lowering in symmetry was responsible for tilting of octahedral structures similarly to the case of some oxides.

On the other hand, Clarke *et al.* [39] and Logvinovich *et al*. [40] reported preparation of $LaTiO_2N$ powders with space group of triclinic $I\bar{1}$, which has three inequivalent anion sites. In the former report, the distribution of anions was almost random but its deviation from perfectly random distribution is larger than that of the specimen with *Imma* space group. The specimens in the latter study exhibited clear deviation from the statistical distribution. Almost half of one site was occupied by nitrogen (and also by oxygen) while the other two sites showed similar O/N occupation ratio close to 75%. In this case, not only tilting but also distribution of anions contributes to the lowering in symmetry. The authors confirmed that the lowered symmetry originates from the characteristic anion distribution based on the results of

electron diffraction observation manifesting the presence of superstructure.

The high temperature neutron diffraction measurement conducted on $SrTaO_2N$ and $SrNbO_2N$ by Yang *et al*. explained how the anion arrangement was formed in the perovskite oxynitrides [32]. They detected structures with *I*4/*mmm* space group which possess two inequivalent anion sites in their specimens at 300 °C. While one site showed 50/50 occupation ratio of oxygen and nitrogen, the other site was almost perfectly occupied with oxygen. This means that almost all nitrogen ions distribute in the two dimensional planes perpendicular to the axis that O-*B*-O chain forms (Fig. 3). This partial anion order was robust up to at least 750 °C. The random planer structure is consistent with local ordering of *cis* type units, which will be described later on, when we consider random zigzag *B*-N chains spread into a plane.

Decrease in temperature to room temperature resulted in phase transition of the materials into low symmetry phase with space group of *I*112/*m*, which was lowered in symmetry from *I*4/*mcm* space group by distribution of nitrogen. The phase transition

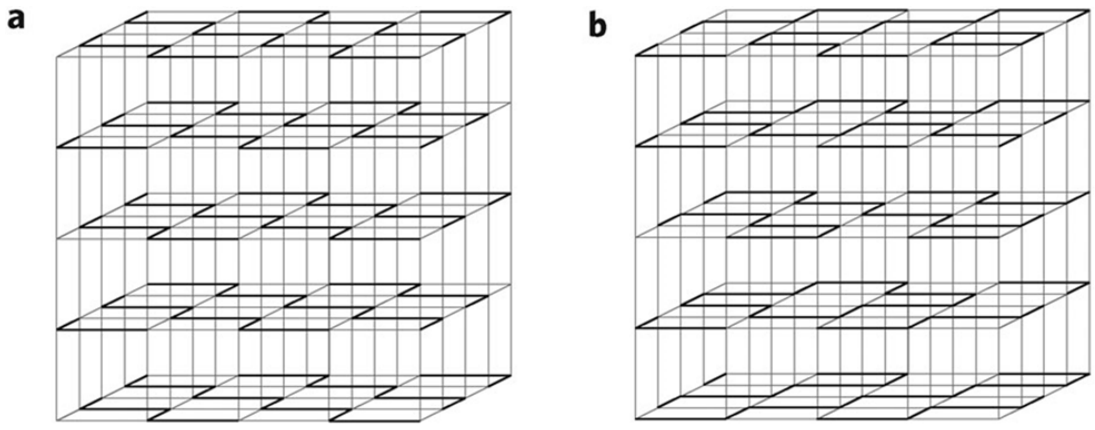

Figure 3. Pervskite oxynitride with (a) perfectly ordered and (b) disordered 2D plane composed of –*B*–N– chain. B site is allocated at each corner and *B*–N–*B* bonds are represented with bold lines. Reprinted by permission from Macmillan Publishers Ltd: Nature Chemistry [32], copyright 2011.

was dominated by rotation of the octahedral structures (Fig. 4). Interestingly the peculiar axis around which the rotation occurred was not the special axis in the high temperature phase formed with O-*B*-O chain but one of the axes included in the 2D plane with random distribution of oxygen and nitrogen. The resulting anion distribution at low temperature can be described by the combination of 50:50 and 75:25 occupancies of oxygen and nitrogen ions in the anion sites mentioned above. The same characteristic distribution has been observed in some other systems including $CaTaO_2N$ [30] and $NdVO_2N$ [58]. In the case of $LaNbON_2$ [43], opposite distribution between nitrogen and oxygen was observed. In addition, electron diffraction measurements proved the formation of superstructure associated with anion arrangement in some perovskite oxynitrides: ABO_2N (*A* = Eu, Sr; *B* = Nb, Ta), $EuWO_2N$ [32], $LaTiO_2N$ [40], $LaNbON_2$ [43] and $NdVO_2N$ [58].

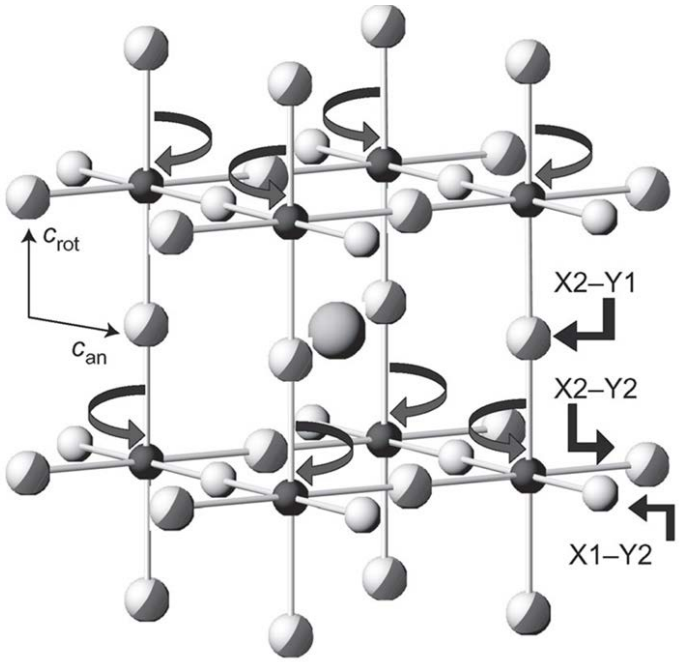

Figure 4. Rotation manner in the transition from high temperature to low temperature phase in perovskite oxynitrides $SrTaO_2N$ and $SrNbO_2N$. Reprinted by permission from Macmillan Publishers Ltd: Nature Chemistry [32], copyright 2011.

$BaTaO_2N$ and $BaNbO_2N$ can be an exception of the considerable kinds of the structurally investigated perovskite oxynitrides because only highly symmetric cubic structure has been observed in them [19,21,27]. This means that the distribution of nitrogen is perfectly random in all three directions and that the ochtahedral structures are not tilted at all or the tilting is perfectly averaged out.

In addition to the studies on average structure using diffraction techniques, observation techniques to investigate local structure have also been applied for perovskite oxynitrides. Extended X-ray-absorption fine-structure (EXAFS) analysis is a powerful method to obtain the information about local bond length. Ravel *et al.* conducted EXAFS measurements on L_{III} edge of $BaTaO_2N$ [12]. Despite neutron diffraction measurements concluded that the average structure was cubic with high symmetry, the XAS spectrum could not be explained by assuming a simple cubic perovskite model. While the assumption of equal lengths for Ta-O and Ta-N bonds yields an unusual value for a fitting parameter, the model considering two different distances between Ta and anions reproduced the spectrum very well. The two different bond distances correspond to Ta-N and Ta-O bonds and the Ta-N bonds were shorter than Ta-O ones by about 0.1 Å. This result contradicts to the general expectation on bond lengths using ionic radii of oxygen (1.38 Å) and nitrogen (1.46 Å), which are widely used to anticipate bond lengths in ionic crystals of oxides and nitrides. The contradiction suggests that the Ta-N bond has considerable covalency because the length of bonds nitrogen forms in organic molecules is usually shorter than those of oxygen [74]. This indicates the presence of local disorder in $BaTaO_2N$.

Page *et al*. investigated the local structure of $BaTaO_2N$ with the technique of neutron pair distribution function (PDF) analysis [74]. In PDF refinements, diffuse

scattering of neutrons in a limited scale of tens Å is analyzed, which is contrastive to the whole range refinement in usual Rietveld analyses. Though the simple cubic structure showed good fit to experimental data in the Rietveld analysis, deviation from experiments became obvious by decreasing the range order of PDF analysis. This indicates that the local structure is apart from the average structure. The authors also conducted first principles calculation to examine the local structure and found that a *cis*-type ordered structure is more stable than the perfectly random one. Because the *cis* structure reproduced the local neutron scattering spectrum well, they concluded that the ordered *cis*-type structure is formed in a local scale of 10 to 20 Å but averaged out in a macroscopic scale in $BaTaO_2N$.

In $BaTaO_2N$, signs of deviation of local structure from simple cubic perovskite were also visible in electron diffraction. Withers *et al.* found diffuse patterns running through the sheets of $\mathbf{G} \pm \{001\}$, indicating formation of polar structures along <001> direction in real space [75]. They suggested that the polar structures were caused by the shift of Ta ions as seen in ferroelectric peorvskite oxides due to the large bond strain of 0.4095 derived from the simple cubic model though correlation between them would be suppressed by strain field formed by the random O/N distribution.

Though the manners of anion distribution and bonding nature of nitrogen ions in perovskite oxynitride compounds have been gradually clarified, key factors to determine anion arrangement have not been understood well. This is partly because of the bad controllability of ammonolysis reaction and thus new synthesis method that allows us to change synthesis parameters more flexibly is demanded for further understanding.

2.3.3 Computational calculation

Though only a small number of reports are found in the literature, first principles calculations have been conducted to understand the structures of perovskite oxynitdes. Computational approaches have advantages that they can “control” anion arrangement freely even if the arrangement is not experimentally confirmed.

Fang *et al*. calculated the most stable structures of $BaTaO_2N$ with ordered and pseudo-random anion arrangements [76]. For ordered arrangements, they assumed three types: *trans*-type, *cis*-type and a combination of different coordination states of Ta (TaO_3N_3 and TaO_5N). They found that the geometries have different relaxed (optimized) structures from each other. All the three settings showed large shifts of Ta ions from the first setting of highly symmetric pseudo-cubic by about 0.1 Å. While the change in lattice constant was not very large in the latter two settings despite the large shift of Ta, the *trans* structure showed large change in lattice structure and bond lengths. Larger change in Ta-N bond than Ta-O one was observed in the *trans* structure and the resulting cell volume and distortion (*c*/*a* ratio) were larger than the other two settings. The total energies of the two structures other than the *trans*-type one were similar (0.06 eV difference) and 0.2 eV smaller than the *trans* structure.

In first principles calculations, a perfectly random structure cannot be investigated because a supercell is assumed and extended by periodic repeat in order to reduce calculation cost. In the report, they assumed two different $4a_0 \times 4a_0 \times 4a_0$ supercells with different combinations of some Ta coordination states to address the structure and stability of random geometries reported in experiment. In these pseudo-random settings, distribution of bond lengths between cations and anions were

investigated and a clear tendency was found that the Ta-N bonds were shorter than the Ta-O bonds. The obtained values for the bond lengths were in good agreement with the experimentally observed bond lengths from neutron diffraction. The total energies of the pseudo-random structures were close to those of the two ordered structures other than the *trans* structure. Considering the reduction in Gibbs free energy $\Delta G \approx \Delta E - T\Delta S$ with the contribution of the entropy term, the random structures are more stable than the ordered structures.

They calculated the electronic structure of one of the pseudo-random structures. Despite the varieties of coordination states, Ta ion showed small variation in charge. This was considered to be due to the covalency in Ta-anion bonds which was well described by the fact that the calculated charges of O, N and Ta are deviated from the formal ones by more than 1. On the other hand, Ba showed an almost empty 6*s* state, which represents its ionic nature.

Characteristic features were seen in the calculated band diagram. A significant hybridization between N 2*s* and Ba 5*p* orbitals was discernible despite they are semicore levels. The band structure consisted of hybridized O 2*p*, N 2*p* and Ta 5*d* orbitals. The N 2*p* level largely contributed to the top of the valence band.

Wolff *et al*. calculated the structures of perovskite oxynitrides ABO_2N (*A* = Ca, Sr, Ba and *B* = Ta, Nb) assuming space groups of highly symmetric cubic $Pm\bar{3}m$, tetragonal *I*4/*mcm* and orthorhombic *Pnma*, which are observed in experiments [77]. Throughout all of the systems, the $Pm\bar{3}m$ structures were most unstable and the *Pnma* ones were most stable. They attributed this to the antibonding hybridization between O and Ta or O and O based on the orbital calculation assuming perovskite-like molecules. In the most stable *Pnma* structures, the calculated bandgap values are in good agreement

with the experiment ones while those of the $Pm\bar{3}m$ settings were much smaller. The calculated bond lengths of Ta-N bonds were shorter than those of Ta-O ones as well as the calculation performed by Fang *et al*. In their calculation, the most stable structure was the ordered structure with $Pmc2_1$ space group, which is derived from *Pnma* space group whose symmetry is lowered by anion arrangement. They considered the reduction of Gibbs energy due to the entropy effect is not enough to stabilize random structures and speculated that the structures with higher symmetry observed in experiments are the consequence of thermal averaging at a finite temperature.

Page *et al*. conducted first principles calculation on $BaTaO_2N$ and $SrTaO_2N$ to investigate the local ordering indicated by PDF analysis, constructing three structural models: Polar *trans*, antipolar *trans* and antipolar *cis* arrangements (Fig. 5) [74]. They obtained optimized structures with *P*4*mm*, *I*4/*mmm* and *Pbmm* space groups for $BaTaO_2N$, respectively. Table 3 shows the bond distances between Ta and anions and total energy of the optimized structure. As can be seen, the *cis* type structure is the most stable of the three, which is in good agreement with experimental structural analyses. Furthermore, they suggested that the polar *trans* structure is stabilized by biaxial stress considering the large tetragonal distortion. This situation was similar to the case of $SrTaO_2N$ as shown in Table 4.

Hinuma *et al.* optimized the structures of $BaTaO_2N$ and $SrTaO_2N$ in more detail to explain their high dielectric constants, which will be described again later on [13]. They started structural optimization with small supercells composed of one or two perovskite ABO_2N formula units and then gradually extended the size of supercells based on the stable cells in smaller size. In the first optimization, they compared *cis*- and *trans*-type units and found that the *cis*-type unit is much more stable than the

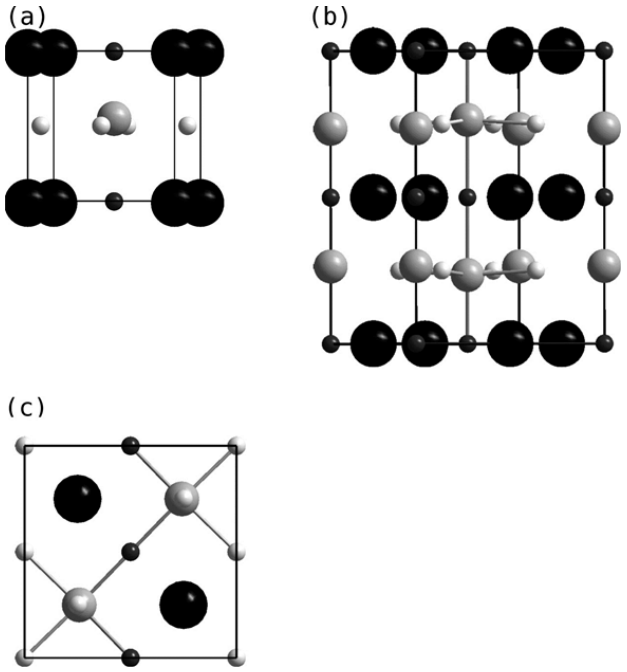

Figure 5. Three structural models for ordered perovskite oxynitride: (a) Polar *trans*, (b) Antipolar *trans* and (c) antipolar *cis*. Reprinted with permission from [74]. Copyright 2007 American Chemical Society.

Table 3. Optimized structure for $BaTaO_2N$ based three models in Fig. 5. Adapted with permission from [74]. Copyright 2007 American Chemical Society.

	Polar *trans* (*P4mm*)	**Antipolar *trans* (*I4/mmm*)**	**Antipolar *cis* (*Pbmm*)**
d_{Ta-O} (Å)	(4×) 2.060	(4×) 2.078	(2×) 2.176
			(2×) 2.068
d_{Ta-N} (Å)	(1×) 2.787	(1×) 2.076	(2×) 2.007
	(1×) 1.870	(1×) 2.075	
ΔE (meV)	0	−482	−508

Table 4. Optimized structure for $SrTaO_2N$ based three models in Fig. 5. Adapted with permission from [74]. Copyright 2007 American Chemical Society.

	Polar *trans* (*P4mm*)	**Antipolar *trans* (*I4/mcm*)**	**Antipolar *cis* (*Pbmm*)**
d_{Ta-O} (Å)	(4×) 2.037	(4×) 2.059	(2×) 2.158
			(2×) 2.036
d_{Ta-N} (Å)	(1×) 2.652	(2×) 2.071	(2×) 1.993
	(1×) 1.877		
ΔE (meV)	0	−85	−550

trans-type one. They continued the calculation up to supercells with $2 \times 2 \times 4 = 16$ formula units. The most stable structures finally obtained were non-centrosymmetric with coiled chains of Ta-N bonds both in the cases of $BaTaO_2N$ and $SrTaO_2N$ (Fig. 6 and 7 for $BaTaO_2N$ and $SrTaO_2N$, respectively). Spontaneous polarizations are raised by the shift of ions in $BaTaO_2N$ while the tilting of ochtahedral structures broke

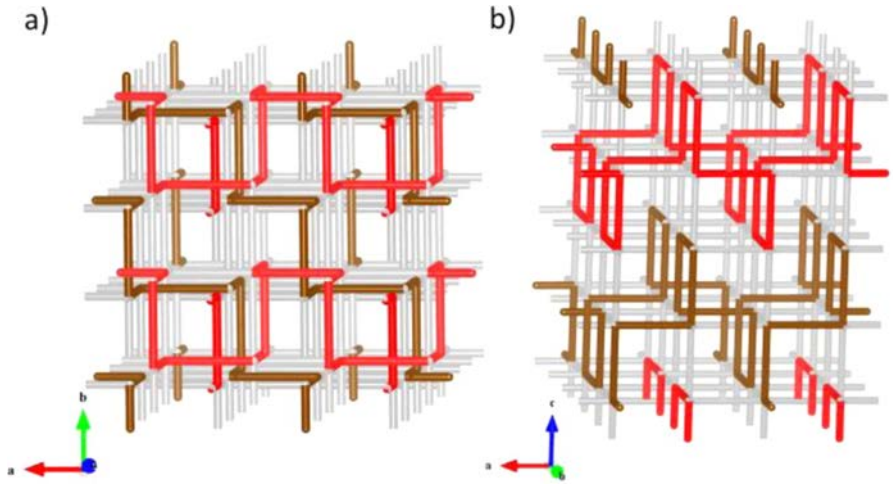

Figure 6. Optimized structure for $BaTaO_2N$ viewed from two directions. Reprinted with permission from [13]. Copyright 2012 American Chemical Society.

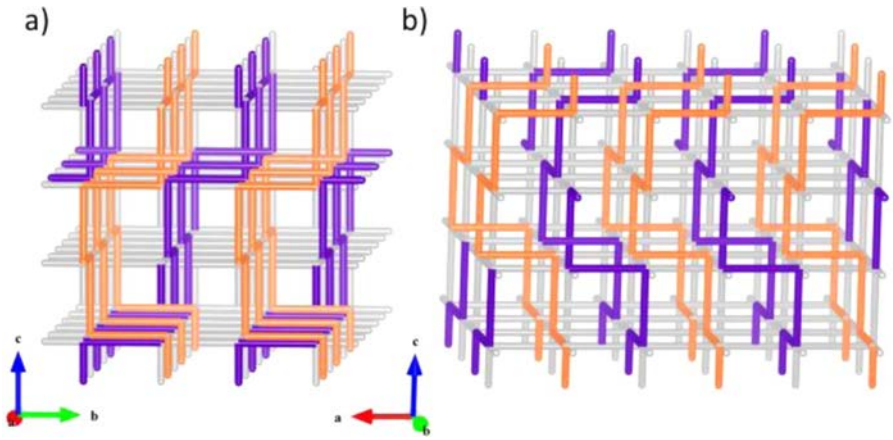

Figure 7. Optimized structure for $SrTaO_2N$ viewed from two directions. Reprinted with permission from [13]. Copyright 2012 American Chemical Society.

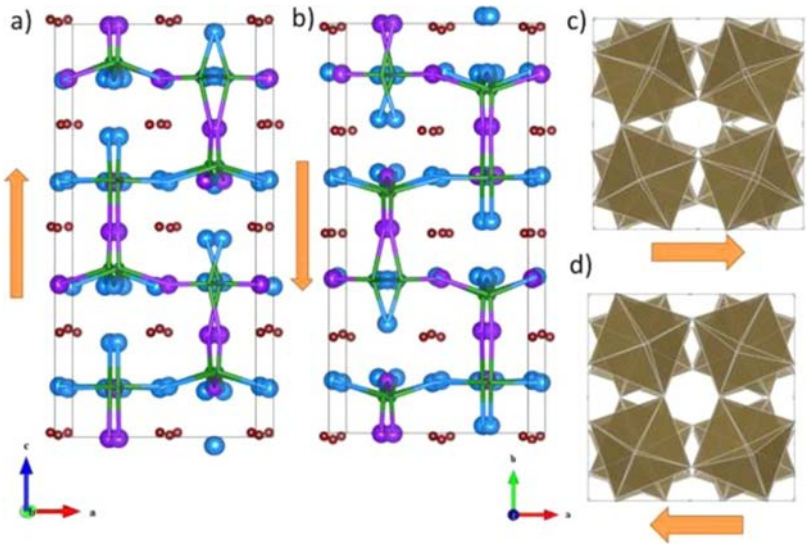

Figure 8. Direction and origin of spontaneous polarization in (a) $BaTaO_2N$ and (b) $SrTaO_2N$. Reprinted with permission from [13]. Copyright 2012 American Chemical Society.

centrosymmetry in $SrTaO_2N$ (Fig. 8). They considered that the flexible polarizations which are easily fluctuated by thermal energy at room temperature are the origin of the high dielectric constant though connection of the supercells with random orientations cancels out net polarization.

The past computational researches on the structures of perovskite oxynitrides showed good agreements with local structures observed or suggested in experiments. However, full understanding of the structure is still far because of the large calculation cost for the structures with large supercells. For further computational approaches, new methods that can treat larger cell sizes are needed.

2.3.4 Theory

The arrangement of oxygen and nitrogen in perovskite oxynitrides is contrastive to those of cations in mixed-cation perovskite oxides. In the case of cation

arrangement, it is well known that the degree of order/disorder is determined by the difference in charge and ionic radius of coexisting species: larger difference in charge and/or ionic size favors ordered structures in higher extent. If the rule is applied to oxygen and nitrogen in oxynitrides, the difference in ionic radius and charge is high enough to form ordered structure stably. However, anions tend to arrange randomly or to be ordered partly in perovskite oxynitrides as described above.

Attfield attributed this to the difference in covalency between nitrogen and oxygen [74]. While ionic radius of nitrogen is larger than oxygen, the length of the covalent bond formed between N and C in a molecule of FCN is smaller than that of the bond between O and C in the isoelectric CO_2. Considering the fact that the *B*-N bonds tend to be slightly shorter than the *B*-O bonds in perovksite oxynitride, as observed both experimentally and theoretically, the *B*-N bonds are considerably covalent even in the basically ionic crystals.

The high covalency of nitrogen ions can give explanation to the favorable formation of *cis*-type units in a local sense. Actually, the trend is not limited to perovskite oxynitrides and but is visible even in polyatomic ions of MoO_2^{2+} and molecules including $MoO_2F_2(thf)_2$ (thf = tetrahydrofuran) and $Mo(NtBu)_2Cl_2(py)_2$ (py = pyridine) [78]. Tatsumi *et al*. explained that this is because the *cis*-type arragement allows larger number of configurations forming π bonding hybridizations between the *d* orbitals of central metals and the *p* orbitals of coordinating species than *trans*-type.

Despite the very similar lengths of the *B*-O and *B*-N bonds results from their partially covalent (and partially ionic) nature, the distribution of oxygen and nitrogen ions was not perfectly statistical and their partial ordering to form 2D planer structure was observed in some perovskite oxynitrides (see Fig. 3). Although the origin of the

favorable formations of the partial ordering has not been clarified, Camp *et al*. gave an interesting insight into the entropy of the system with partially ordered anions [79]. That is, the calculated entropy S on the 2D planer structure showed an unusual relation of $S = (2R\ln 2)/N^{1/3}$ per mole to the number of atoms N where R is gas constant. This "subextensive" entropy is close to 0 for a large single crystal contains one mole atoms while finite entropy remains for a small nanoparticle of several tens nanometers. Because perfectly ordered and random states were described by entropies proportional to N^0 and N^1, respectively, the partially ordered state may be related to the subextensive entropy. For deeper understanding, future experimental investigations on the entropy of perovskite oxynitride specimens are required.

2.4 Physical properties

Perovskite oxides have been revealed to show a wide range of functionalities and the methods to investigate them have been well established for more than half century. In contrast, the history of perovskite oxynitrides is too short for researchers to get systematic understanding on their physical properties and to apply them to actual uses. Nevertheless, their properties reported so far are unique. Thus, it is expected that perovskite oxynitrides exhibit functionalities and applications that are hardly accessible by conventional materials.

2.4.1 Visible light absorption

When a precursor oxide is converted to the corresponding perovskite

oxynitride, color obviously changes under a d^0 configuration. Since nitrogen is less electronegative than oxygen, the nitrogen 2*p* orbital is higher in energy than the oxygen 2*p* orbital, resulting the narrowing of bandgap from ultraviolet (UV) to visible light region. Considering the fact that the bandgaps of semiconductors vary depending on their chemical compositions and crystal structures, colors of perovskite oxynitrides might be tunable to some extent.

Jansen *et al.* reported good tunability of color from yellow through orange to deep red by changing the *x* value from 0.05 to 1.0 in the system of $Ca_{1-x}La_xTaO_{2-x}N_x$ (Fig. 9) [7]. The authors suggested that conventional pigments of these colors, usually containing toxic heavy metals including cadmium, can be replaced by the perovskite oxynitrides, taking into account the environmental friendliness and the heat stability of oxynitrides.

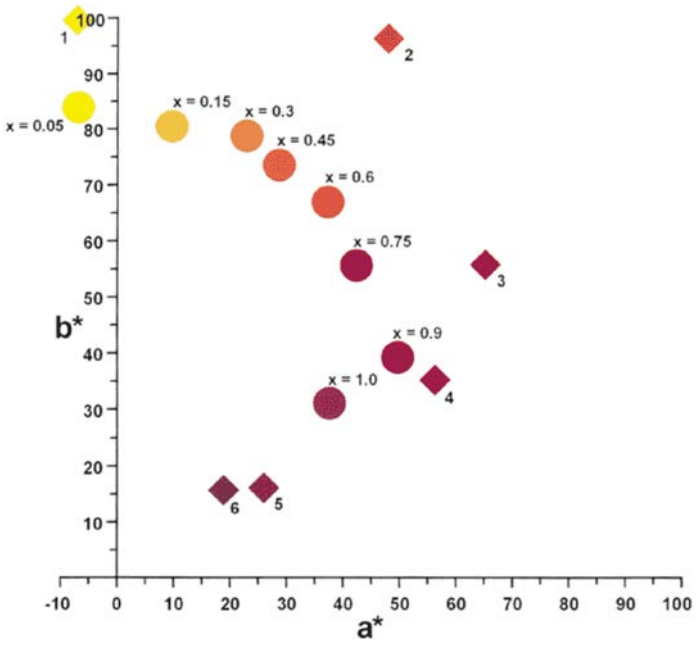

Figure 9. Color coordinates of $Ca_{1-x}La_xTaO_{2-x}N_x$ (circle) and other pigments, cadmium yellow (1), cadmium orange (2), cadmium red (3), cadmium dark red (4), Fe_2O_3 (5) and $(Al_{0.95}Mn_{0.05})_2O_3$. Reprinted by permission from Macmillan Publishers Ltd: Nature [7], copyright 2000.

Aguiar *et al*. studied the colors of various kinds of perovskite oxynitrides including $CaTaO_2N$, $SrTaO_2N$, $BaTaO_2N$, $Yb_2Ta_2O_5N_2$ (with layered perovskite structure), $CaZr_{0.5}Ta_{0.5}O_{2.5}N_{0.5}$, $SrNbO_2N$, $BaNbO_2N$, $SrTiO_3$:N and $LaTiO_2N$ [8]. They discussed the change in bandgap in relation with the width and position of conduction band mainly composed of the empty *d* orbitals of the *B*-site metals. Generally speaking, the band structures of perovskite materials are explained with the overlap between metal *d* orbitals and *p* orbitals surrounding the *B*-site metal both in σ- and π-type configurations. This hybridization of orbitals has been confirmed by theoretical calculations in many reports.

The overlap between the two types of orbitals is highly affected by the bond angle of *B*-*X*-*B*: It takes the highest value of 180˚ in a straight bond, and monotonically decreases to less than 180˚ with tilting of the bond. Though the contribution of the orbitals of *A*-site cations to the hybridization is negligible, the ionic sizes of *A*-site cations determine the value of tolerance factor and the resulting crystal structure including bond angles. The series of perovskite oxynitrides of $CaTaO_2N$, $SrTaO_2N$ and $BaTaO_2N$ gave a good example for this situation. Crystal system of $CaTaO_2N$, $SrTaO_2N$ and $BaTaO_2N$ were determined to be orthorhombic, tetragonal and cubic, respectively, with XRD, and the bond angle of Ta-(O,N)-Ta bonds was found to increase from 153.3˚ through 169.9˚ to 180˚ in the order [8]. This trend reflects the difference in ionic radii of Ca^{2+}, Sr^{2+} and Ba^{2+} with the values of 1.48, 1.58 and 1.75 Å, respectively. The resulting bandgap values are 2.4, 2.1 and 1.8 eV, respectively. The decrease in bandgap is due to the widening of the *d* orbital of Ta ion caused by increased hybridization (Fig. 10a).

In contrast to the width, the position of *d* orbitals depends on electronegativity of transition metals [8]. For example, Nb^{5+} ions are more electronegative and possess *d*

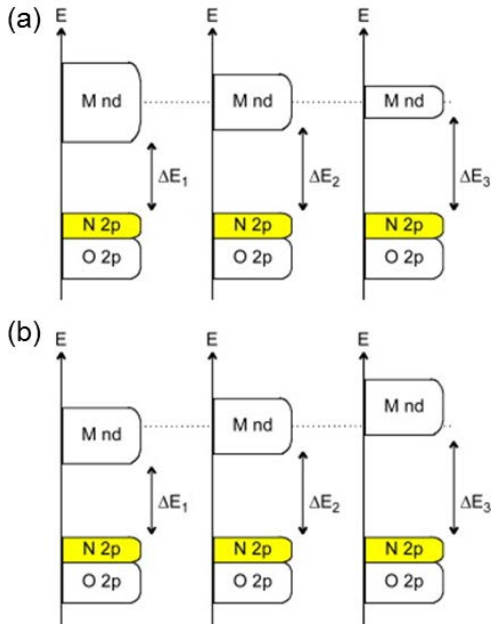

Figure 10. Easy models of band structure of perovskite oxynitrides with (a) different bond angle and (b) different covalency of cations. Reprinted from Dyes and Pigments, **76**, R. Aguiar *et al.*, "The vast colour spectrum of ternary metal oxynitride pigments", 70–75, Copyright 2008, with permission from

orbitals at lower energy than Ta^{5+} ones. This explains why $BaNbO_2N$ has a narrower bandgap than $BaTaO_2N$ and also $SrNbO_2N$ than $SrTaO_2N$ despite the similar ionic radii of Nb^{5+} and Ta^{5+} (Fig. 10b).

2.4.2 Photocatalysis

Another promising usage of the visible-light-active band structure is photocatalysis. Since the first discovery of water splitting reaction known as Honda-Fujishima effect in 1972 [80], many kinds of semiconductors have been studied in terms of their photocatalytic activity. The photocatalytic process has been explained as follows [81,82]: 1) Irradiation light excites electrons in valence band to conduction band and forms hole-electron pairs inside a photocatalytic material. 2) The generated

holes and electrons migrate from inner parts to surface regions. 3) Electrons and holes causes following redox reactions, respectively.

$$2H^+ + 2e^- \rightarrow H_2 \tag{2.6}$$

$$H_2O + 2h^+ \rightarrow \frac{1}{2}O_2 + 2H^+ \tag{2.7}$$

If the bandgap is in visible light region, sun light energy can be converted into the electrochemical energy to produce of hydrogen and oxygen gas effectively without any hazardous exhaust. Thus, use of visible-light active perovskite oxynitride as photocatalyst has a possibility to provide a good solution to the worldwide energy problem.

One of the most crucial requirements for photocatalytic materials is band alignment. This is not only because bandgap determines the active wavelength of light but also because the positions of conduction band and valence band determine whether the redox reactions proceed. Because the redox potentials of the above two reactions are fixed to 0 and +1.23 V vs. NHE at pH = 0, respectively, the redox potential of conduction band must be lower (i.e. higher in energy) than 0 V vs. NHE and that of valence band must be higher than +1.23 V vs. NHE [82].

Balaz *et al*. reported precise band structures of perovskite oxynitrides ATaO$_2$N (A = Ca, Sr and Ba) and PrTaON$_2$ [29]. They determined the positions of Fermi level, valence band maximum and conduction band minimum by combining techniques of X-ray photoemission spectroscopy (XPS), Kelvin probe force microscopy, UV-vis spectroscopy and depth-resolved cathode luminescence spectroscopy. Though ATaO$_2$N possessed suitable positions for both conduction band and valence band, the valence band maximum of PrTaON$_2$ was lower than +1.23 V vs. NHE in redox potential. This

result suggests that the *A*TaO_2N perovskite oxynitrides can prompt overall water splitting while $PrTaON_2$ can cause hydrogen production alone.

However, the situation is somewhat more complicated. So far, the report of successful processing of overall water splitting is limited to $CaNbO_2N$ [38], $LaTiO_2N$, $Ca_{0.25}La_{0.75}TiO_{2.25}N_{0.75}$ [10] and $BaZr_xTa_{1-x}O_{2+x}N_{1-x}$ [54]. Other perovskite oxynitrides are active only for a partial reaction or non-active. This is because photocatalytic reactions can be prevented by many factors: Defects inside crystal structure sometimes provide finite density of states inside the gap (defect level) which tends to prevent generation of hole-electron pairs, to trap the generated carriers, to recombine them and/or even to cause self-decomposition of the photocatalyst [10]. Sample shape also affects the efficiency because it determines the effective surface area where the redox reactions occur. Low crystallinity enhances the chance of recombination of the generated carries because it reduces the mobility of carriers.

Efficiency of water splitting with perovskite oxynitride photocatalysts has been not enough for practical use despite intensive researches so far. Moriya *et al*. summarized synthesis of perovskite oxynitrides for photocatalysts as a fundamental issue in the field in their review paper [83]. It is difficult to obtain perovskite oxynitride specimens with suitable quality using the conventional ammonolysis and the technique must be improved.

2.4.3 Electrical properties

In contrast to the wide investigations on photocatalytic properties, the number of studies on electrical properties has been very limited. This is mainly because of the difficulty in excluding extrinsic effects in powder samples obtained with conventional

ammonolysis [9,67]. Even so, the reported electrical properties on perovskite oxynitrides are unique.

Kim *et al*. reported anomalously high dielectric constant of $BaTaO_2N$ and $SrTaO_2N$ [11]. Because impedance spectra are contributed by both bulk and grain boundaries, they extracted the signal from the bulk part. The resulting dielectric constants were in the order of 2000–5000. These values were comparable to those of practical ferroelectric materials such as PZT though ferroelectric behavior was not observed. In contrast to the behaviors of dielectric constant in ferroelectric materials, the dielectric constants of $SrTaO_2N$ and $BaTaO_2N$ were almost independent of temperature (Fig. 11). Dielectric constants in the same level or even higher values were observed in the specimens of $SrTaO_2N$ with improved density by Zhang *et al* [35]. However, $BaTaO_2N$ epitaxial thin films showed one order of magnitude lower dielectric constant

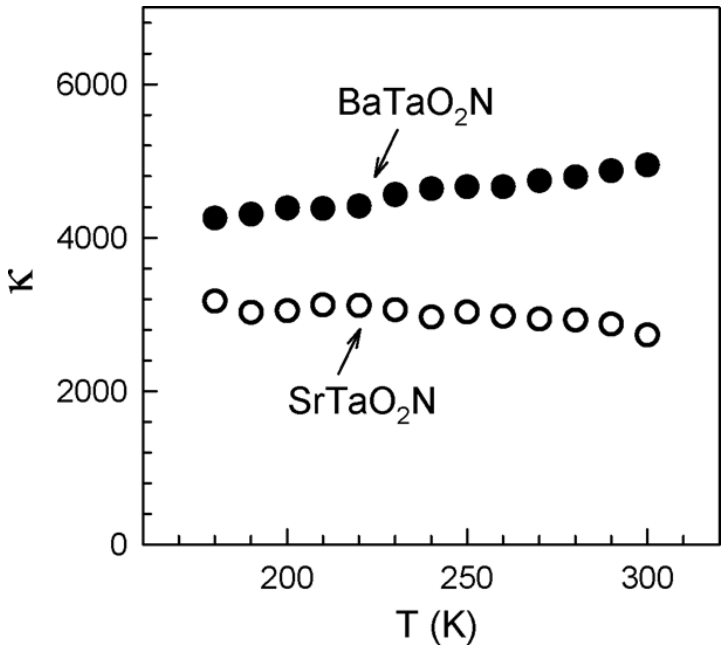

Figure 11. Temperature dependence of dielectric constant of $BaTaO_2N$ and $SrTaO_2N$ in bulk form. Reprinted with permission from [11]. Copyright 2004 American Chemical Society.

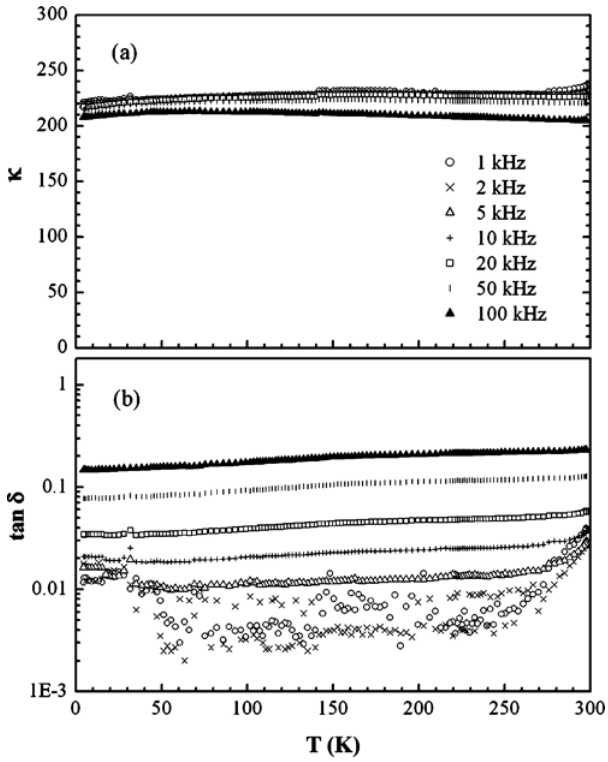

Figure 12. Temperature dependence of dielectric constant and dielectric loss of $BaTaO_2N$ epitaxial thin film. Reprinted with permission from [61]. Copyright 2007 American Chemical Society.

and it is still unclear whether the high values observed in the bulk specimens were intrinsic (Fig. 12). As for the origin of the high dielectric constant, Hinuma *et al.* suggested the contribution of local spontaneous polarizations associated with certain anion arrangements as mentioned above [13].

Kusmartseva *et al.* [48] and Yang *et al.* [49] reported colossal magnetoresistance in $EuWO_{1+x}N_{2-x}$, where the behavior is dependent on the composition parameter x. They prepared specimens with various x from 0.41 through 0.25, 0.18, 0.09 and −0.04 to −0.12. All the samples showed ferromagnetism with Curie temperature of 11–13 K which derived from spins of f electrons in Eu^{2+}. Because W is in d^0 state with the composition of $EuWON_2$, the composition with positive x means an electron-doped state ($W^{6+} \rightarrow W^{5+}$) and negative x represents a hole-doped state

($Eu^{2+} \rightarrow Eu^{3+}$). Negative magentoresistance was observed at low temperature in the full range of *x*. In the electron doped region, the resistance increased monotonically with approaching to the stoichiometric d^0 state except for the highest doped specimen, which showed higher resistivity than expected possibly due to the electrical inhomogeneity. Along with the increased resistivity, magnetoresistance is enhanced and reached the highest at the composition of $x = -0.04$. Hole-doping also caused decrease in resistivity and magnetoresistance. The authors attributed the magnetoresistance to the coupling of *d* electrons of W^{5+} and *f* electrons of Eu^{2+} in the electron-doped region and double exchange interaction between Eu^{2+} and Eu^{3+} in the hole-doped region.

Despite the uniqueness of the electrical properties, researches on them have been prompted at a struggle pace. Similarly to the cases of studies on photocatalytic properties, there is a strong demand for high quality samples which are free from extrinsic effects mainly caused by structural faults in both microscopic and macroscopic scales.

2.5 Strategy of this study

As mentioned above, the biggest issue in the research field of perovskite oxynitrides is preparation of samples with suitable shape and quality for characterization. One of the best ways to access to high quality single crystalline samples is epitaxial growth, considering its large contribution to the researches on perovskite oxides especially in the field of basic research. In this study, I adopted NPA-PLD method to grow epitaxial thin films of perovskite oxynitrides. Advantages of

this technique which I will focus on in this study are as follows: 1) The technique enables soft nitridation which avoids degradation of sample quality during preparation unlike the cases of conventional ammonolysis and sputtering techniques. 2) Stress stabilization of a certain crystal structure is possible and can be used to control anion arrangement in oxynitride films. 3) Nitrogen supply is independent of the supplies of other species constructing perovskite framework, which would lead to good controllability of nitrogen amount and related electronic configuration in the films.

Related to the first feature, I firstly investigated whether it is possible to obtain stoichiometric oxynitrides with NPA-PLD because the technique has been used to dope small amounts of nitrogen, less than several at%, into oxides, but not to synthesize films containing nitrogen as a major component [71,84]. After optimization of the chemical compositions of the films, film qualities including crystallinity and surface morphology were investigated. The electric properties of the films were also evaluated from dielectric capacitance measurements to demonstrate that the film quality was high enough to conduct reliable electrical measurements. $SrTaO_2N$ and $CaTaO_2N$ were chosen as model materials.

The technique to stabilize a certain crystal structure under epitaxial strain was applied to control the anion arrangements in perovskite oxynitrides. Page *et al*. suggested that the polar *trans* type structure of $SrTaO_2N$ can be stabilized if the material grown on a substrate with smaller lattice constant feels compressive stress. Based on this idea, I attempted epitaxial growth of $SrTaO_2N$ (a = 4.03 A; pseudo-cubic approximation [11]) on STO substrate (a = 3.905 A). Focusing on the spontaneous polarization of the calculated structure, I investigated ferroelectricity of the obtained films. In addition, the influence on anion arrangement was structurally investigated on a

series of $Ca_{1-x}Sr_xTaO_2N$ thin films, in which epitaxial strain was controlled.

As another topic, I investigated the influence of nitrogen on transport property using the third feature of NPA-PLD mentioned above. I chose $SrNbO_{3-x}N_x$ as a model compound because Nb has flexibility in valence state in contrast to Ta, in which Ta^{5+} state with d^0 is very stable. I studied the change in transport property of the system whose nitrogen content was systematically controlled.

Chapter 3

Experimental techniques

3.1 Sample preparation

3.1.1 Nitrogen plasma assisted pulsed laser deposition [85–87]

Pulsed laser deposition (PLD) is one of the established ways to grow thin films of solid state materials, especially semiconductors, and categorized as physical vapor deposition. Because it enables fine tuning of composition and crystallinity of films with variable parameters, the obtained specimens generally have enough quality for characterization of physical properties and for practical uses.

As shown in the schematic illustration of PLD in Figure 13, a pulsed laser is used to transfer elements in a source, so-called target, to substrate on which films are grown. Usually lasers used in PLD possess wavelengths of several hundred nm such as 266 nm and 355 nm of quadrupled and tripled Nd:YAG laser, respectively, and 193 nm, 248 nm and 308 nm of ArF, KrF and XeCl excimer lasers, respectively. These short wavelengths enable to form nanosecond pulses in which energy density is enhanced drastically from a continuous laser. When a target placed in an ultrahigh vacuum (UHV) chamber is irradiated with a pulsed laser, the high energy of the laser is absorbed by the target and causes excitation of surface part of the target and injection of single particles

and/or clusters of ionic and atomic species of included elements. The excitation is known to accomplish a complicated process which makes the injected “plume” vertical to the target surface. This highly directed supply of sources enables easy transfer of cationic composition from the targets to thin films. Furthermore, the high energy of laser gives high kinetic energy to the ablated species which enables crystallization at low temperature. This feature sometimes makes it possible to synthesize metastable phases including oxynitrides.

There are two variable parameters related to the laser pulses: fluence (areal energy density) and repetition rate. The laser fluence is controllable with inserting attenuators on its optical path. It has been reported that the fluence affects the transfer efficiency of source elements and precise tuning is required to achieve a perfect transfer of cationic composition from the target to the films. The repetition rate affects the density of anion vacancies in the films. It is difficult to transfer anionic composition from the target to the films completely because anions are easily released from the plume and/or the films to the vacuum circumstance as molecular gas and film composition tends to be less in anions than the original composition of the target. Higher repetition rate generally leads smaller amounts of anion vacancies in the films due to the less time for anions to be released. At the same time, deposition rate of the films are determined by the multiple of supply of the source species by one pulse, which is dependent on the fluence, and the repetition rate. The deposition rate generally affects crystallinity and/or phase stability of the films because it determines the migration time of the active species transferred at the surface of the substrates.

Another factor to determine the anionic composition in the films is the atmosphere. PLD chambers are generally evacuated to UHV with pumps. And it is

possible to supply gases from inlets attached to the chambers and control the partial pressure of them in the chambers with variable leak valves. In case of oxide growth, oxygen gas is generally supplied to control oxygen composition in the films. Meanwhile, in nitrogen plasma assisted pulsed laser deposition (NPA-PLD), nitrogen gas is supplied instead of oxygen in a form of activated plasma from a plasma source equipped to the preparation chamber (Fig. 13). Here, input power to the plasma source is a variable parameter in addition to the partial pressure of N_2 gas.

When epitaxial growth is supposed, single crystals with good lattice matching to an objective material are generally used as template substrates. Depending on the crystallization temperature and the stability of the objective materials, heating of

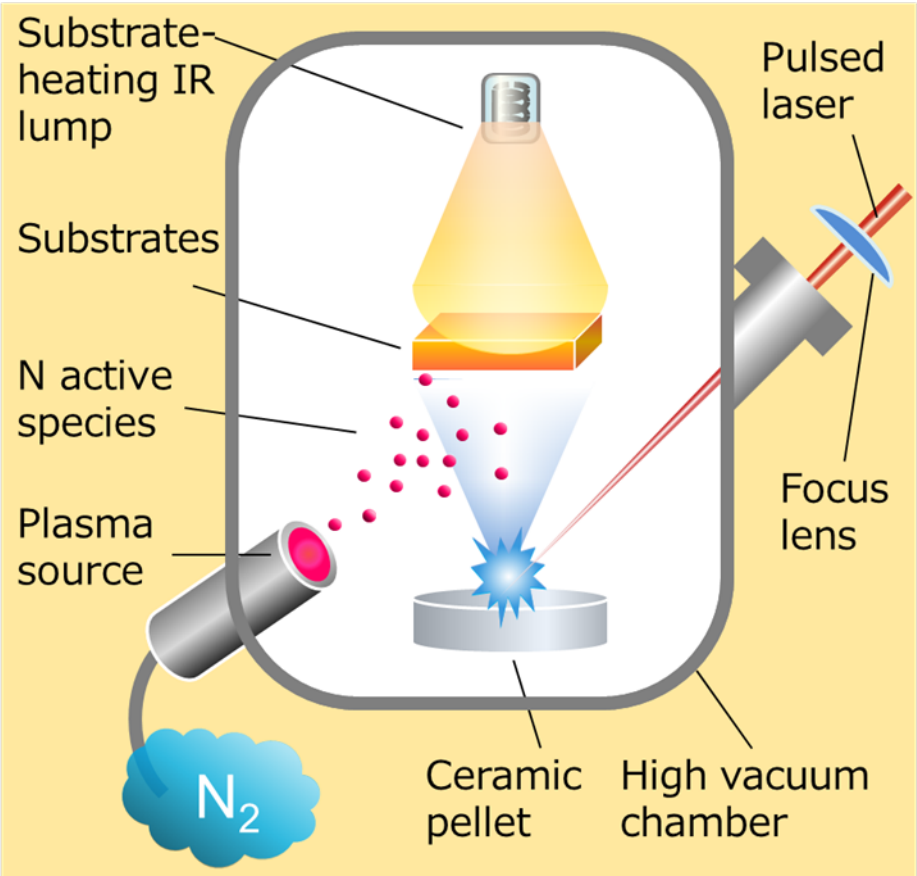

Figure 13. Setup of nitrogen plasma assisted pulsed laser deposition.

substrates is sometimes necessary and the substrate temperature is a variable parameter.

In this study, I used a NPA-PLD system based on a UHV preparation chamber (base pressure $\sim 3 \times 10^{-9}$ Torr) equipped with a KrF excimer laser (λ = 248 nm) and plasma sources such as an electron cyclotron resonator and a radio frequency plasma source. The targets were ceramic pellets of oxides obtained by conventional solid state reactions. The oxides contained the same cation ratio as the objective perovskite oxynitrides. The substrates were single crystals of perovskite oxides which has relatively close lattice constants to the film materials. During the deposition of the films, the substrates were attached to graphite plates with platinum paste and fixed with metal clumps. The backside of the graphite plates were irradiated with infrared light from a lump set in the preparation chamber and the substrate temperature was controlled by the lump input power.

3.2 Crystallographic characterization

3.2.1 Reflection high energy electron diffraction [88–91]

In situ observations on a synthesis process are helpful to understand growth mechanisms of specimens and to optimize their synthesis conditions. As for crystal growth, several diffraction techniques are available for observations under UHV or high-vacuum conditions. Reflection high energy electron diffraction (RHEED) is one of the most established methods among them. Because RHEED provides information on

the crystal structure and morphology of the outermost atomic layer of the sample surfaces, it is useful to observe the crystal growth of deposited films without background signals from the inner structure.

In a typical setup of the measurement, an electron beam is projected from an electron gun to the sample surface with a glancing incident angle within a range of 0.5–2.5 °. The electrons are accelerated by high voltage of 10 to 50 kV to achieve enough high cross-section of diffraction at such low incident angles. Inelastic scattering makes penetration length of electrons in the order of 10 nm, resulting in observation depth less than 1 nm at the shallow incident angles. Scattered electrons were detected with a phosphor screen facing the electron gun across samples and form a diffraction pattern on it.

When electrons with a wave vector $\boldsymbol{k}_0$ are scattered to a wave vector $\boldsymbol{k}$, scattering amplitude F is given by the following equation using the electron density $\mathrm{n}(\boldsymbol{r})$ and the scattering vector $\boldsymbol{K} = \boldsymbol{k} - \boldsymbol{k}_0$.

$$F = \int \mathrm{n}(\boldsymbol{r})\exp(-iK \cdot \boldsymbol{r})\mathrm{d}\boldsymbol{r} \tag{3.1}$$

In a crystal with a periodic lattice structure, the electron density $\mathrm{n}(\boldsymbol{r})$ is given by the sum of the electron densities per unit cell $\mathrm{n_a}(\boldsymbol{r} - \boldsymbol{r}_\mathrm{m})$ as following.

$$\mathrm{n}(\boldsymbol{r}) = \sum_{\boldsymbol{r}_\mathrm{m}} \mathrm{n_a}(\boldsymbol{r} - \boldsymbol{r}_\mathrm{m}) \tag{3.2}$$

where $\boldsymbol{r}_\mathrm{m}$ is the position of a unit cell, represented as $\boldsymbol{r}_\mathrm{m} = x\boldsymbol{a}_1 + y\boldsymbol{a}_2 + z\boldsymbol{a}_3$. Here, x, y and z are integers and $\boldsymbol{a}_1$, $\boldsymbol{a}_2$ and $\boldsymbol{a}_3$ are the lattice vectors. Substituting equation (3.2) in equation (3.1), we obtain

$$F = \int_{\substack{\mathrm{unit} \\ \mathrm{cell}}} \exp(-i\boldsymbol{K} \cdot \boldsymbol{\rho})\mathrm{n_a}(\boldsymbol{\rho})\mathrm{d}\boldsymbol{\rho} \times \sum_{\boldsymbol{r}_\mathrm{m}} \exp(-i\boldsymbol{K} \cdot \boldsymbol{r}_\mathrm{m}) \tag{3.3}$$

$$= S_{\boldsymbol{K}} \times L_{\boldsymbol{K}}$$

where $\boldsymbol{\rho} = \boldsymbol{r} - \boldsymbol{r}_{\mathrm{m}}$. The first and second terms are called structure factor and Laue function, respectively.

In a single crystal with a size of $V = X\boldsymbol{a} \times Y\boldsymbol{b} \times Z\boldsymbol{c}$ where X, Y and Z are integers, the contribution of the Laue function to the scattering cross section is given by the following equation.

$$|L_{\boldsymbol{K}}|^2 = \frac{\sin^2 \frac{X}{2}(\boldsymbol{a} \cdot \boldsymbol{K})}{\sin^2 \frac{1}{2}(\boldsymbol{a} \cdot \boldsymbol{K})} \times \frac{\sin^2 \frac{Y}{2}(\boldsymbol{b} \cdot \boldsymbol{K})}{\sin^2 \frac{1}{2}(\boldsymbol{b} \cdot \boldsymbol{K})} \times \frac{\sin^2 \frac{Z}{2}(\boldsymbol{c} \cdot \boldsymbol{K})}{\sin^2 \frac{1}{2}(\boldsymbol{c} \cdot \boldsymbol{K})} \tag{3.4}$$

The equation has a finite value when $\boldsymbol{a} \cdot \boldsymbol{K} = 2h\pi$, $\boldsymbol{b} \cdot \boldsymbol{K} = 2k\pi$ and $\boldsymbol{c} \cdot \boldsymbol{K} = 2l\pi$ where h, k and l are integers. These equations are satisfied when $\boldsymbol{K}$ is a reciprocal lattice vector $\boldsymbol{G}$, represented by the following equation using the reciprocal vectors $\boldsymbol{b}_1$, $\boldsymbol{b}_2$ and $\boldsymbol{b}_3$.

$$\boldsymbol{b}_1 = 2\pi \frac{\boldsymbol{a}_2 \times \boldsymbol{a}_3}{\boldsymbol{a}_1 \cdot \boldsymbol{a}_2 \times \boldsymbol{a}_3} \; ; \; \boldsymbol{b}_2 = 2\pi \frac{\boldsymbol{a}_3 \times \boldsymbol{a}_1}{\boldsymbol{a}_1 \cdot \boldsymbol{a}_2 \times \boldsymbol{a}_3} \; ; \; \boldsymbol{b}_3 = 2\pi \frac{\boldsymbol{a}_1 \times \boldsymbol{a}_2}{\boldsymbol{a}_1 \cdot \boldsymbol{a}_2 \times \boldsymbol{a}_3} \tag{3.5}$$

$$\boldsymbol{G} = h\boldsymbol{b}_1 + k\boldsymbol{b}_2 + l\boldsymbol{b}_3 \tag{3.6}$$

Thus, a diffraction occurs when $\boldsymbol{K} = \boldsymbol{G}$ is satisfied. This is called Bragg condition and can be schematically drawn with Ewald's sphere. The first term of equation (3.4) becomes 0 when $\boldsymbol{a}_1 \cdot \boldsymbol{K} = 2\pi/\mathrm{X}$. This leads the width of the diffraction peaks in the direction along $\boldsymbol{a}_1$ is of the order of $2\pi/\mathrm{X}$. This means that the size of the observed regions determines the distribution of diffraction intensity. Thus, the diffraction pattern reflects the surface morphology.

When an observed surface is rough in an atomic scale, the observed length is limited to short lengths in the incident direction of the electron beam. This broadens the distribution of intensity and the Ewald's sphere crosses multiple reciprocal lattice points

within a Laue zone, which result in a spotty diffraction pattern. On the other hand, an atomically flat surface leads the observed length in surface normal direction to almost 0 which results in rod-like diffraction patterns elongated along the direction. If there are many step structures on the sample surface, observation length in in-plane direction is also limited to several nm and thus the distribution parallel to the surface is broadened as well. The resulting intensity distributions are thick rods and a streak pattern is formed on the screen. When a step-terrace structure with a constant terrace width is formed by slight tilting of an atomically flat surface, not only the crystal lattices but also the reciprocal step-terrace structure forms reciprocal rods tilting at the same angle as the surface. The reciprocal rods formed by the step-terrace structure cut the other reciprocal rods formed by the lattice structure, which results in diffraction patterns composed of short rods. If the steps are small in number, the reciprocal rods formed with the crystal structure are very thin in in-plane direction and crossed parts with the Ewald's sphere becomes spot. Differently from the patterns formed by rough surfaces, the Ewald's sphere crosses only once with a Laue zone and the spots align concentrically.

Not only the lattice structure but also the crystallinity is also reflected by the diffraction pattern. When a polycrystalline specimen is observed with RHEED, ring patterns are formed on the screen. This is because the random orientation of the crystals causes rotation of the reciprocal points with a central focus at the zero-point and a spherical distribution of diffraction intensity which crosses with the Ewald's sphere with a circular cross section. Amorphous samples show no bright peaks but halo patterns originating from the diffuse scattering of electrons by the component atoms.

Surface-morphology sensitive RHEED measurement is applicable to observe crystal growth mode of thin films. Film growth modes can be categorized into 3 general

groups: Layer-by-layer, step-flow and island growth modes (Fig. 14). Stranski-Krastanov growth mode is a layer-by-layer mode followed by an island growth. Each growth mode has a particular time dependence of the RHEED intensity and pattern on the screen. In layer-by-layer growth mode, the surface of the specimen undergoes random distribution of the adatom species on each terrace during a turn of surface renewal which ends with the perfect coverage of the original surface. This causes a continuous wave-like oscillation of the RHEED intensity (Fig. 15a). A step-flow mode growth is generally observed at relatively high temperature and the adatoms migrate to step edges before the perfect coverage with a new layer. This causes shift of the step edges and RHEED intensity drops when steps traverse the observed area (Fig. 15b). In island growth mode, the second or later layers grow on the tops of the first layers before the coverage of the original surface by the first layer is completed.

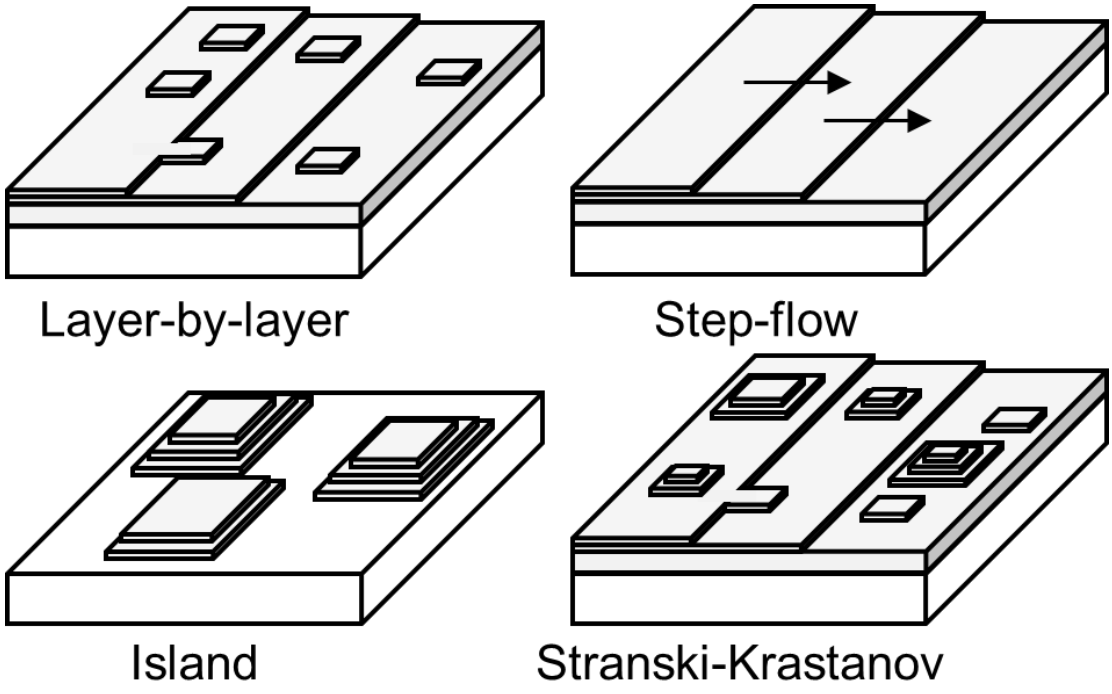

Figure 14. Four basic modes of film growth with epitaxy.

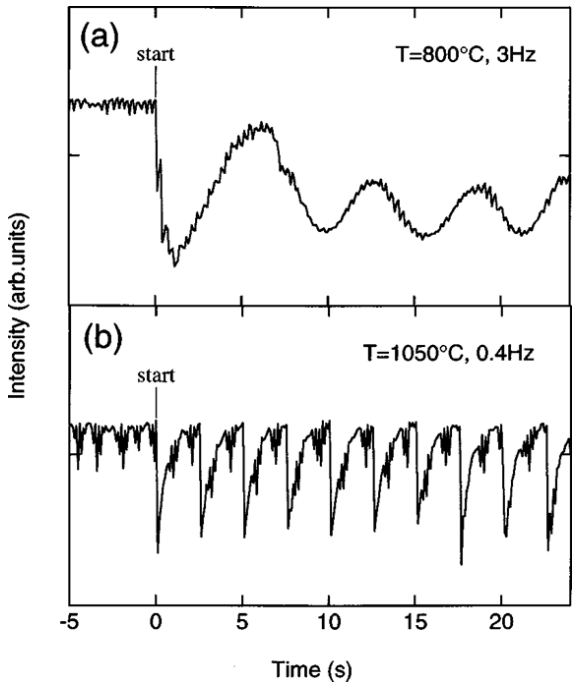

Figure 15. RHEED oscillation observed in (a) layer-by-layer and (b) step-flow mode. Reprinted with permission from [90]. Copyright1999, AIP Publishing LLC.

This forms many island like structures on the surface of substrates and the RHEED pattern changes with reflecting the surface morphology. This is contrastive to the former two modes where atomically flat surfaces are maintained during the deposition. Though the former two modes are preferable to obtain high quality single crystal films without grain boundaries, they tend to be prevented by defect structures and are realized only when mismatch between the film and the substrate are small enough to allow coherent growth of the films.

3.2.2. X-ray diffraction [88,90]

X-ray diffraction (XRD) is one of the most common methods to evaluate crystal structures of solid materials. In contrast to RHEED observation, the measurements are generally conducted in the air with exceptions of *in situ* observations

under UHV conditions using a special instrumental setting. Because X-ray has smaller wave length than high energy electron beam, the peaks are more separated and resolution is higher in XRD than in electron diffraction techniques.

Figure 16 shows a typical setting of a 4-axis XRD machine composed of an X-ray generator, optics, a sample stage on a goniometer, a detector and a monitor. The relative positions of the detector and the measured sample to the incident X-ray are described by angles θ and ω, respectively. In addition, the sample can be tilted or rotated in χ and φ directions. Bragg condition can be translated into the following equation using θ.

$$2d \sin\theta = n\lambda \tag{3.7}$$

where d is the distance between the lattice layers under the observation, λ is the wavelength of the incident X-ray and n is an integer. Lattice constants of the sample can

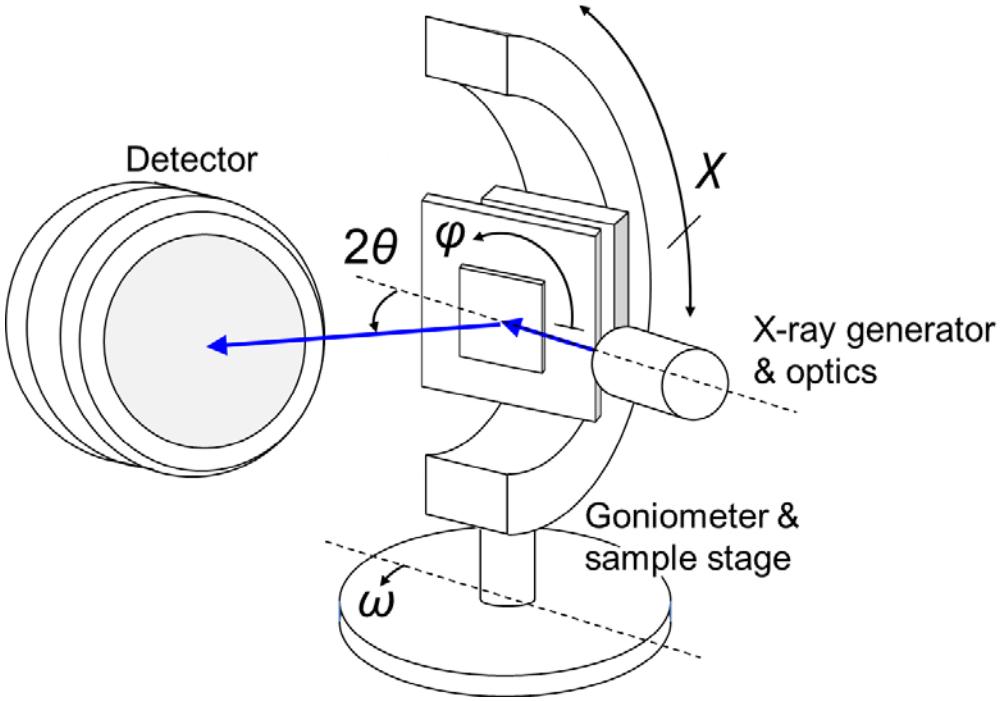

Figure 16. Setup of X-ray diffraction measurement and direction of 4 axes of a goniometer equipped to sample stage.

be calculated from the 2θ values of the peaks by using the equation. When lattice planes parallel to the surface are measured, symmetric diffractions occur under a condition of $\theta = \omega$. Diffractions caused from the other lattice planes can be observed when the sample is tilted in a proper direction (so-called asymmetric settings). XRD data are often shown by the plot of diffraction intensity versus 2θ value measured under conditions of $\theta = \omega$ (2θ-θ plot), because it is useful to visualize the peak positions and the phase purity.

There are mainly three kinds of detectors: 0D (spotty), 1D (linear) and 2D (circular) detectors. With increasing the detector dimensions, detection range becomes larger while resolution becomes lower. Thus, 2D detectors are useful for survey measurement and 1D and 0D detectors are generally used for fine measurements to a certain direction.

Not only microscopic lattice structures but also macroscopic geometries can be investigated with XRD. Equally to RHEED measurement, peak width in 2θ direction reflects the size of the sample. As for thin film samples, thickness can be estimated also from the intervals of oscillation patterns appearing around each peak due to the interference of the diffracted beams.

In contrast to 2θ direction, peak width in χ direction, which can be measured by 2D detectors, reflects orientation of the crystals. Because each diffraction peak is limited to a certain direction in an ideal single crystal, peak width in χ direction is almost 0. Contrastively, a polycrystalline structure exhibits ring patterns diffused in χ direction due to the overlap between the Ewald's sphere and the reciprocal spheres as in the cases of RHEED measurements. Thus, crystallinity can be estimated from the peak width in χ direction when a real sample is measured. The distribution of peak intensity derived from crystal orientation can be seen also in ω direction. Intensity curves

obtained by measuring a peak by changing ω are called rocking curves and full width at half maximum (FWHM) of them is widely used as a measure of crystallinity.

Reciprocal space mapping (RSM) technique enables direct observation on the reciprocal space cut by a plane. While diffractions occurring at different ω are integrated for each 2θ point in 2θ-θ measurements, intensity distributions along 2θ are collected separately for each ω point in RSM measurements. This situation is created by repeating point measurements with a fixed 1D detector. The resulting data is a map of diffraction intensity plotted on 2θ-ω plane, which can be converted into a map whose axes are reciprocal units. Using an RSM image, one can see the relationship of coexisting crystals such as a thin film and its substrate.

In this study, XRD measurements were conducted with commercial 4-axis diffractometers (Bruker AXS, d8 discover). Out-of-plane and in-plane lattice constants were calculated from peak positions of symmetric (00*n*; n = 1, 2, 3 and 4) and asymmetric (*n*0*n*; n = 1 and 2) diffractions. Mean value and standard deviation of each lattice constant are shown in the graphs. Temperature dependence of lattice constants was measured using a domed hot stage (Anton Paar, DHS 1100) evacuated by a rotary pump (~10 Pa).

3.2.3 Atomic force microscopy [93–95]

Atomic force microscopy (AFM) is one of the techniques categorized as scanning probe microscopy (SPM). SPM enables microscopic observations on surface topography and spatial distribution of physical quantities by detecting an interaction between a scanning probe and a specimen. In AMF measurement, atomic force between the probe and the sample is used to observe microscopic surface morphology. Figure 17

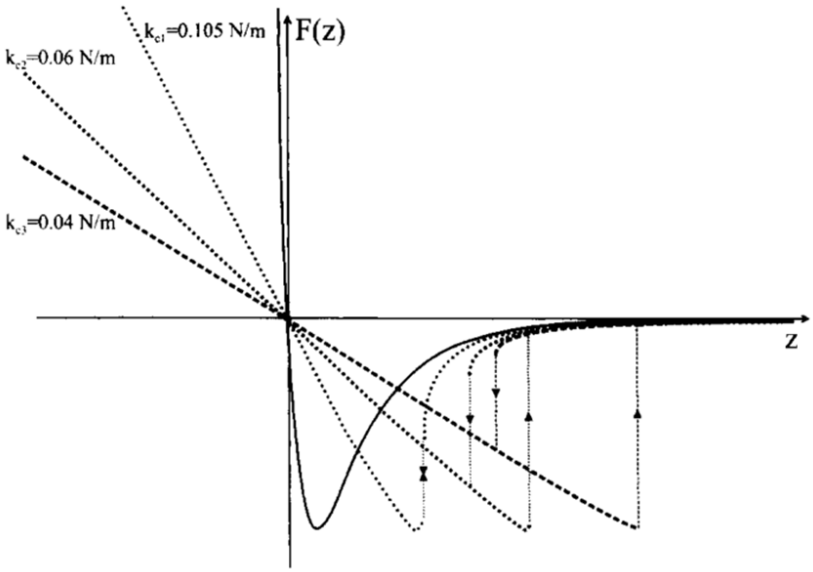

Figure 17. Force-displacement curves. Broken lines shows the experimentally obtained curves with cantilevers with different elastic constants. Reprinted from Surface Science Reports, 34, B. Cappella *et al*., "Force-distance curves by atomic force microscopy", 1–104, Copyright 1999, with permission from Elsevier.

shows the relationship between the atomic force and sample-probe distance, where the positive and negative values represent repulsive and attractive forces, respectively. Solid materials are generally measured in the region where the repulsive Van der Waals force dominantly works. In this region, the variation of atomic force accompanied by the distance change is large and the displacement of the probe is detected sensitively (Contact mode AFM). In contrast, soft materials are generally measured in the attractive force region to avoid shape change of the sample by the scanning probe (Non-contact mode).

Displacement of the probes normal to the sample surface is usually detected by a system using an optical cantilever. In the system, laser is projected on the cantilever on which the probe is attached and reflected to a photo detector. The optical path magnifies the displacement of the cantilever and enables atomic scale detection.

In usual AFM measurements, sample-probe distance is kept at constant by feedback of the sample stage using piezoelectric system during the probe scanning and the feedback values are mapped (Constant-force mode). Meanwhile, samples with atomically flat surfaces are sometimes measured in “constant height mode” where the feedback system is off and the displacement of the cantilever itself is mapped.

In this study, commercial SPM systems (SII-nanotechnology, SPI4000 with SPA400 and E-Sweep with NanoNaviReal) were used for AFM measurements. All the measurements were conducted in contact and constant force mode.

3.2.4 Transmission electron microscopy [96–98]

Transmission electron microscopy (TEM) makes it possible to observe the inner structure of materials by using electron beam passing through them as a probe. The technique has a very wide range of magnification ratio, which enables observation in the scale from sub-nanometer to several tens micrometer.

Figure 18 shows a basic setting of TEM in which a sample is irradiated with accelerated electrons by a condenser lens and a condenser aperture, then, electrons path through an objective aperture, an objective lens, a diffraction lens, an intermediate aperture and lens and projector lenses and reach at a fluorescence screen. Each lens magnetically focuses electrons with a certain focal length like optical lenses. Images formed by the transmitted electrons are called bright field images while the scattered electrons are used to construct dark field images.

Samples must be thin enough for electrons to path through. In the case of cross-sectional observation on thin films, they are sliced with techniques such as ion milling and focused ion beam methods.

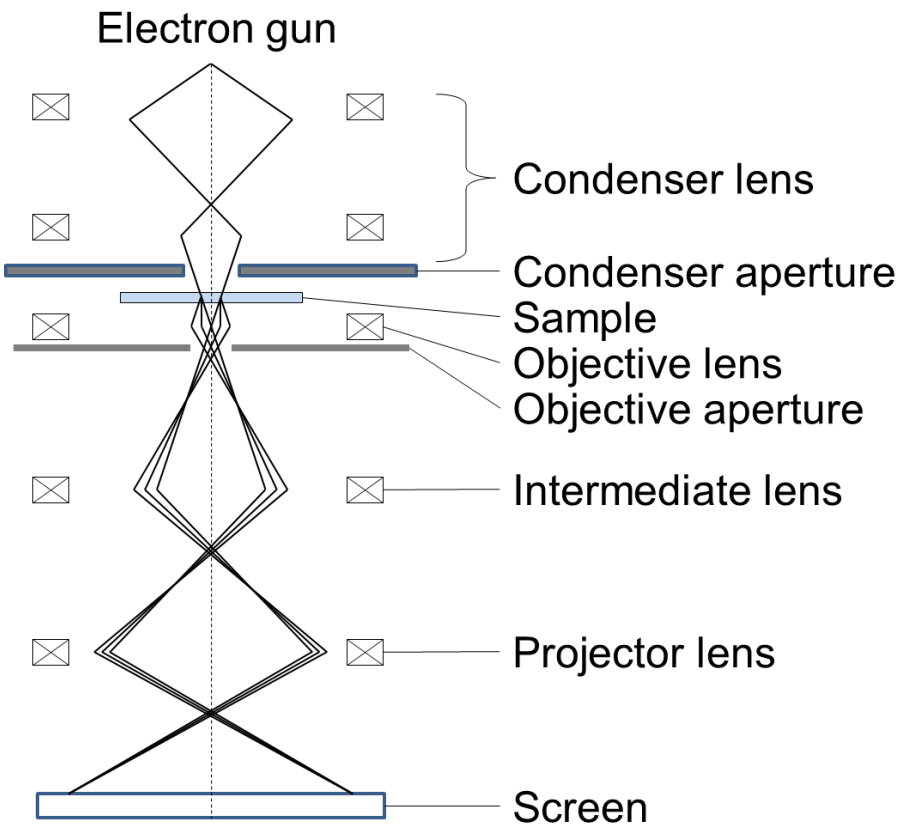

Figure 18. Inner constitution of a transmission electron microscope.

Contrast in TEM images is formed in mainly three manners: Scattering contrast is formed by cutting the scattered electrons with the objective aperture and the intensity is proportional to masses of the scattering atoms. Diffraction contrast is made by stopping the diffracted electrons and reflects the periodic crystal structure in the sample. Phase contrast is formed by the interference between two of the transmitted, scattered and diffracted waves. The latter two contrasts are used in high resolution TEM measurement which provides atomic scale resolution by combined with computational simulations.

Scanning transmission electron microscopy (STEM) is a technique developed in these three decades. In STEM measurements, samples are irradiated with focused

electron beams. This is opposite condition to TEM in which nearly parallel electron beams are focused after they pass through the sample. Atomic scale focusing of electrons has become possible by recent improvements in technique to correct spherical aberration and realized atomic scale observations in STEM measurements.

Annular detectors are used to obtain dark field images in STEM measurements. Especially, images using the electrons scattered to high angle are called high angle annular dark field (HAADF) images. Because the signal intensity is quadratic to atomic mass in HAADF measurements, different ionic species can be identified from each other.

In this study, TEM techniques were adopted to check the phase purity and inner structure of the films directly. For atomic scale measurement, STEM was also used. STEM technique was also applied to site selective observation on anion occupation.

3.3 Compositional characterization

3.3.1 Nuclear reaction analysis [99]

Analysis on anionic composition is one of the significant issues in the studies on oxynitride films because available techniques are limited. Though X-ray photoemission spectroscopy and energy dispersive X-ray analysis with electron beam are frequently used to quantize nitrogen amount in thin films, errors of these measurements are generally large (around 10% or more). This is partly because the former is too surface sensitive and the latter is affected strongly by matrix effects and

possible background signals from the underlying substrate. Elastic recoil detection analysis (ERDA) is one of the reliable methods but requires a special ion beam accelerator which can provide high energy beam of heavy ions like 12 MeV ^{127}I beam [71]. In contrast, nuclear reaction analysis (NRA) can be conducted by using proton beam with as small energy as ~1 MeV in the case of nitrogen quantization.

In NRA, the samples are irradiated by accelerated ion beam and a detector counts emitted radiations caused by a nuclear reaction. The following nuclear reaction can be used for quantization of nitrogen atoms in films.

$$^{15}\mathrm{N}(p, \alpha\gamma)^{12}\mathrm{C} \tag{3.8}$$

The equation represents that a ^{15}N isotope reacts with a proton and emit a α-ray and a γ-ray. Though the natural abundance of ^{15}N is as small as 0.03%, the efficiency of the reaction can be dramatically enhanced by setting the beam energy at a resonance point.

In this study, NRA measurements were carried out with a 1-MV tandetron accelerator at Tandem Accelerator Complex, University of Tsukuba. Resonance at 898 keV of the reaction was used and γ-rays are detected with two 3-inch $Bi_4Ge_3O_{12}$ scintillation counters. The total amount of nitrogen was calculated by comparison to a reference of TiN epitaxial thin films. Error of each data point was calculated assuming 6% deviation in a signal due to fluctuation of ion-beam energy. The value was derived from the standard deviation of signals measured on TiN multiple times.

3.4 Characterization on optical properties

3.4.1 Ultra violet-visible-near infrared spectroscopy

In optical absorption evaluations of thin film materials, it is possible to conduct transmission and reflection measurements, which provide absolute values of absorption. This is an advantage of thin films because diffuse reflection spectroscopy, generally used to evaluate optical absorptions of bulk specimens, is a relative quantification method. The following equations give the values of absorptance A and absorption coefficient α from the transmittance T and reflectance R.

$$A = \frac{1 - T - R}{1 - R} \tag{3.9}$$

$$\alpha = -\frac{1}{t} \ln \frac{T}{1 - R} \tag{3.10}$$

where t is film thickness. Note that these equations are approximated expressions ignoring the contributions of multiple reflections.

In this study absorption spectra were measured in the region of Ultra violet-visible-near infrared (UV-Vis-NIR) light.

3.4.2 Ellipsometry [100,101]

Ellipsometry is a powerful technique to examine optical constants and fine structures of thin film materials or sample surfaces. In the measurement, the samples are irradiated with polarized light and the reflected light is analyzed. Because the analysis process is dependent not on amplitude but only on polarization angle of the reflected light, ellipsometry provides high accuracy.

A basic setup of ellipsometry is composed of a light source, a polarizer, a sample, an analyzer and a photo-detector in this order. A compensator is inserted between the polarizer and the sample when circularly polarized light is used. In actual measurement, some configurations are possible including rotating analyzer ellipsometry, rotating polarizer ellipsometry, rotating compensator ellipsometry, etc.

Light polarization can be dissolved into *s* and *p* wave components, which possess electric field vertical and parallel to the incident plane, respectively. Because reflection on a sample surface causes phase shift and amplitude reduction depending on the polarized directions of the incident light, the reflected light is generally ellipsoidally polarized. Polarization ρ of the reflected light can be represented with two parameters ψ and Δ.

$$\rho = \frac{R_p}{R_s} = \tan\psi \exp(i\Delta) \tag{3.11}$$

where R_s and R_p are the reflectance for *s* and *p* waves, respectively.

When light goes from medium 1 to medium 2, amplitude reflectance for each polarization can be written by the following equations (Fresnel equations).

$$r_s = \frac{N_2 \cos\theta_2 - N_1 \cos\theta_1}{N_2 \cos\theta_2 + N_1 \cos\theta_1} \tag{3.12}$$

$$r_p = \frac{N_1 \cos\theta_2 - N_2 \cos\theta_1}{N_1 \cos\theta_2 + N_2 \cos\theta_1} \tag{3.13}$$

where N_x is the complex refractive index of medium *x* and θ_1 and θ_2 are the incident and refraction angles, respectively. Refraction angle is determined by the following equation (Snell's law).

$$N_1 \sin\theta_1 = N_2 \sin\theta_2 \tag{3.14}$$

Because the reflectance is given by $R_s = |r_s|^2$ and $R_p = |r_p|^2$, the polarization ρ is a

function of the optical coefficients n and k of each medium, which compose complex refractive index by the relation $N = n + ik$. The component k is called extinction coefficient.

At a special incident angle ϕ_B, so-called Brewster's angle, Δ shows sharp drop from 180° to 0° via 90° and ρ reaches its maximum. At the angle, the following relationship is satisfied.

$$\tan \phi_B = \frac{n_2}{n_1} \tag{3.15}$$

Ellipsometry measurements are usually conducted at some points of incident angles around Brewster's angle because the measurement can be conducted with the best accuracy at ϕ_B.

If a sample is composed of several layers as is the case of a film material grown on a substrate, multiple reflections occur at the surface and interfaces. Multiple reflections depend on the optical coefficients and thickness of each layer. Thus, the analysis process in ellipsometry uses optical coefficients and thicknesses as fitting parameters.

Absorption coefficient α can be calculated from the extinction coefficient k with the following equation.

$$\alpha = \frac{4\pi k}{\lambda} \tag{3.16}$$

where λ is the wavelength of the light.

In this study, a commercial spectroscopic ellipsometer (J.A. Woollam, M-2000U) was used in ellipsometry measurements.

3.5 Characterization on electrical properties

3.5.1 Piezoresponse force microscopy [102–104]

Piezoresponse force microscopy (PFM) is equally a SPM technique as AFM. The technique makes it possible to observe a ferroelectric domain structure. In a single domain, direction of spontaneous polarization is three-dimensionally homogeneous. Contrastively to the domain observation by polarized-light microscope in micrometer scale, PFM is a nanometer-scale observation.

Non-centrosymmetric crystals including ferroelectrics exhibit displacement when an external electrical bias is applied (inverse piezoelectric effect). In PFM measurement, an AC bias is applied between a conductive scanning tip and a sample and the sample vibration caused by the inverse piezoelectric effect is detected by the tip. Two detection modes are available in PFM: vertical PFM (VPFM) and lateral PFM (LPFM). While displacements in vertical (normal to surface) direction are examined in VPFM mode, LPFM detects lateral vibrations. Thus, VPFM and LPFM are used to observe out-of-plane and in-plane components of polarizations, respectively.

Amplitude A of piezoresponse depends on the piezoelectric coefficient of the sample. On the other hand, the directions of the polarizations determine the phase shift θ of the piezoelectric vibration from the applied AC bias oscillation. In VPFM mode, an upward polarization causes 180° shift while a downward one causes an in-phase vibration (Fig. 19). Thus, the distribution of the spontaneous polarizations can be visualized by mapping the piezoesponse.

As for samples with a low piezoelectric constant, enhancement of signal by

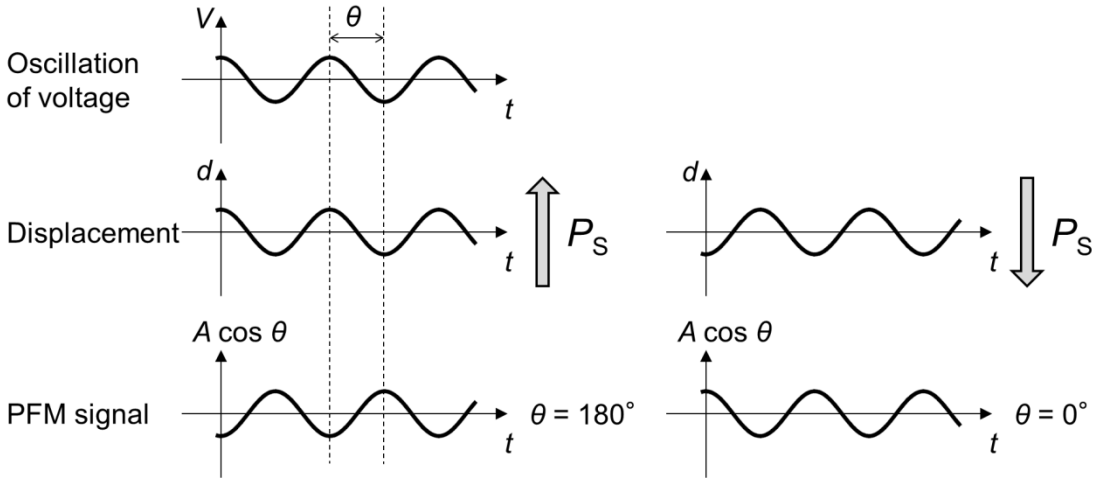

Figure 19. Relationship among AC bias, bias induced displacement and PFM signal. Phase shift in PFM signal is 180° in the case spontaneous polarization directs upward while downward polarization causes in-phase oscillation.

resonance is useful. Depending on the stiffness constant of the cantilevers and the elastic constant of the sample, the piezoelectric vibration undergoes a resonance at a certain frequency of the applied AC field. In resonance mode PFM, the piezoresponse signals are sometimes affected by the surface morphology because the resonance frequency is sensitive to the sample-probe distance. One way to distinguish real piezoresponse signals from the crosstalk of the surface morphology is to check inversion of the phase between the two frequencies slightly lower and higher than the resonant point.

Ferroelectric behaviors can be tested by scanning the tip with applying DC bias over the coercive value of the sample. Following PFM observation shows an artificial single domain in the scanned area if the material is ferroelectric. It is also possible to observe ferroelectric hysteresis loops at a very local point with switching spectroscopy PFM (SS-PFM). SSPFM detects the piezoresponse of the remanent polarization as a

function of the amplitude of the preceding switching DC voltage pulse.

In this study, PFM measurements were conducted using a commercial scanning probe microscope system (SII-nanotechnology, E-Sweep with NanoNaviReal) with a homemade PFM system composed of a function generator (NF corporation, 1930A) and a lock-in amplifier (EG&G, 7260). A Rh-coated silicon cantilever (SII-nanotechnology, SI-DF3-R(100) with stiffness of 1.1 N/m and a resonance frequency of 25 kHz in air) was employed for the measurements.

3.5.2 Impedance measurement [105]

Any electrical systems can be depicted by equivalent circuits composed of resistances, capacitors and inductors. Impedance measurement with an AC electric field is widely applied to measure the components. When a simple solid material without device structure is considered, inner inductances are generally negligible and a parallel or series circuit of a resistance and a capacitor is applicable as an equivalent circuit.

In insulators, whose resistance is high, contribution of capacitance is large in the response to electric fields and they can be used as dielectric materials which can store the energy of applied fields. However, an ideal capacitor does not exist in the real world and any insulators have resistance components, which cause energy loss. Thus, a dielectric material has two quality factors: the ability to store the energy of applied electric fields and the insulating property. The former is described with the dielectric constants ε', while a measure to represent the latter factor is dissipation factor D.

Impedance is defined as a complex quantity to impede AC current flow and all the three components of electrical circuit can be converted into impedance forms. Resistance R is the real part of impedance and capacitance C and inductance L compose

the imaginary part called reactance X as follows.

$$X_C = -\frac{1}{2\pi f C} \tag{3.17}$$

$$X_L = 2\pi f L \tag{3.18}$$

where f is the frequency of the AC field. X_C and X_L are called capacitive and inductive reactance, respectively.

When a parallel circuit of a resistance R and a reactance X is considered, the total impedance Z can be represented as following.

$$Z = \frac{iRX}{R+iX} = \frac{RX^2}{R^2+X^2} + i\frac{R^2X}{R^2+X^2} \tag{3.19}$$

The impedance of a series circuit is as following.

$$Z = R + iX \tag{3.20}$$

Dissipation factor D is defined as the ratio of the real to imaginary parts of the total impedance and results in the following value in both of the parallel and series circuits.

$$D = \frac{R}{X} \tag{3.21}$$

The smaller D value is, the closer the circuit is to an ideal capacitor or inductor. The value is called also as tan δ because it is tangent of vector angle δ of the impedance vector in a complex plane.

In impedance measurements, the real and imaginary impedances are measured and converted into the resistance and reactance components under an assumed equivalent circuit. Calculated values have the following relationships.

$$R_p = R_s(1 + 1/D^2) \tag{3.22}$$

$$X_s = X_p(1 + D^2) \tag{3.23}$$

where R_p and R_s are the resistances calculated based on the parallel and series models,

respectively, and, X_p and X_s are the reactances calculated based on the parallel and series models, respectively. For relatively conductive samples with high *D*, the choice of equivalent circuit has a significant influence on the evaluation of reactance but does not affect the value of resistance so much. For good insulators with low *D*, the situation is opposite.

Dielectric constant can be calculated from the measured capacitance with the following relationship.

$$\varepsilon' = \frac{Cd}{\varepsilon_0 S} \tag{3.24}$$

where ε_0, *d*, *S* represent the vacuum permittivity, distance between electrodes and measured area, respectively.

Each impedance component in a material generally has frequency dependence and the values in a frequency range used in a supposed application are important. Thus, impedance measurements are usually carried out in a certain range of frequency.

There are some methods to measure impedance and an appropriate one must be chosen based on the frequency range and the sample quality. In this study, impedance measurements were conducted with auto-balancing bridge method using a commercial LCR meter (Agilent, E4980). This technique allows a precise measurement in a wide frequency range. Figure 20 shows a basic setup of auto-balancing bridge method in which the sample current is converted into voltage and measured with a high accuracy. In the method, impedance is derived from the following equation.

$$\mathrm{Z} = \frac{E_{low}}{E_{high}} \cdot \frac{1}{R_r} \tag{3.25}$$

where E_{low} and E_{high} are the voltages measured at the high and low end terminals, respectively, and R_r is the reference resistance.

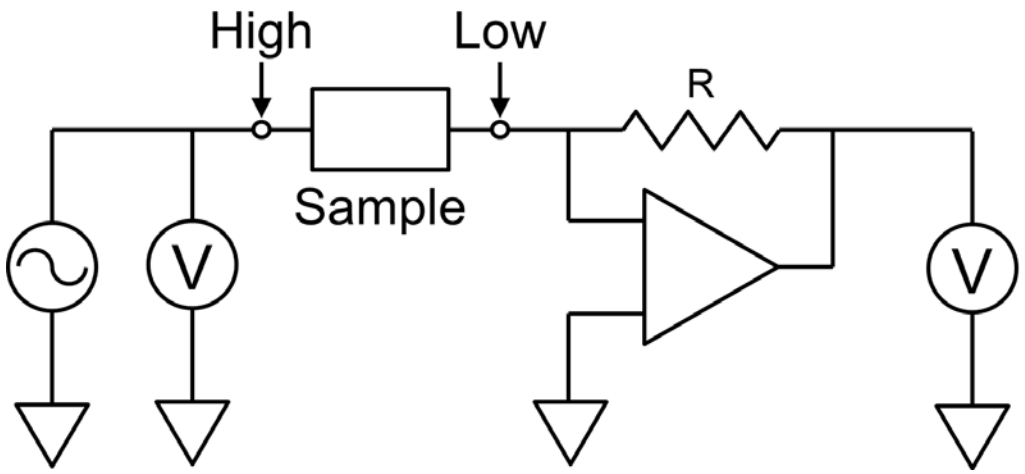

Figure 20. Inner circuit of an auto-balancing bridge.

Terminal configuration is an important factor because it determines parasitic components in the circuit. Some measurement configurations have been developed and we must choose an appropriate way considering the sample impedance and ease of operation.

2-probe method is the simplest way but easily affected by the stray capacitances between the cables and the series impedances of them. 3-probe method enables to cancel the stray capacitances off by using coaxial cables whose shield conductors are connected to the guard terminals of the equipment. One can measure high impedance accurately with this method. 4- and 5-probe methods make it possible to expand the measurement range down to low impedance though their setups are somehow complicated.

In this study, 3-probe method was adopted because of the relatively high impedance of the samples. The samples were attached with top electrodes of platinum deposited by sputtering. Conductive Nb-doped $SrTiO_3$ substrates were used as bottom electrodes. A cryogen-free micro-manipulated probe station (Lake Shore, CRX-4K) was

used for temperature control.

3.5.3 Conductivity measurement [106]

In conductivity measurements on low resistive samples, DC bias is used for probing in order to focus on the resistance component. In a simple 2-probe terminal configuration, the series resistances of the wires, electrodes and interfaces suffer the accuracy of the measurement if the sum of them is comparable to the resistance of the samples. Thus, 4-probe method is generally used to avoid an unexpected voltage drop by the parasitic resistances (see Fig. 21).

Hall measurement technique is useful to evaluate the polarity and density of electrical carriers. Figure 21 schematically shows a basic setup of Hall measurement. Here, an external bias (V_x, 0, 0) is applied along x axis and a magnetic field (0, 0, B_z) is applied vertically to the sample surface. The magnetic field causes Lorentz force to y

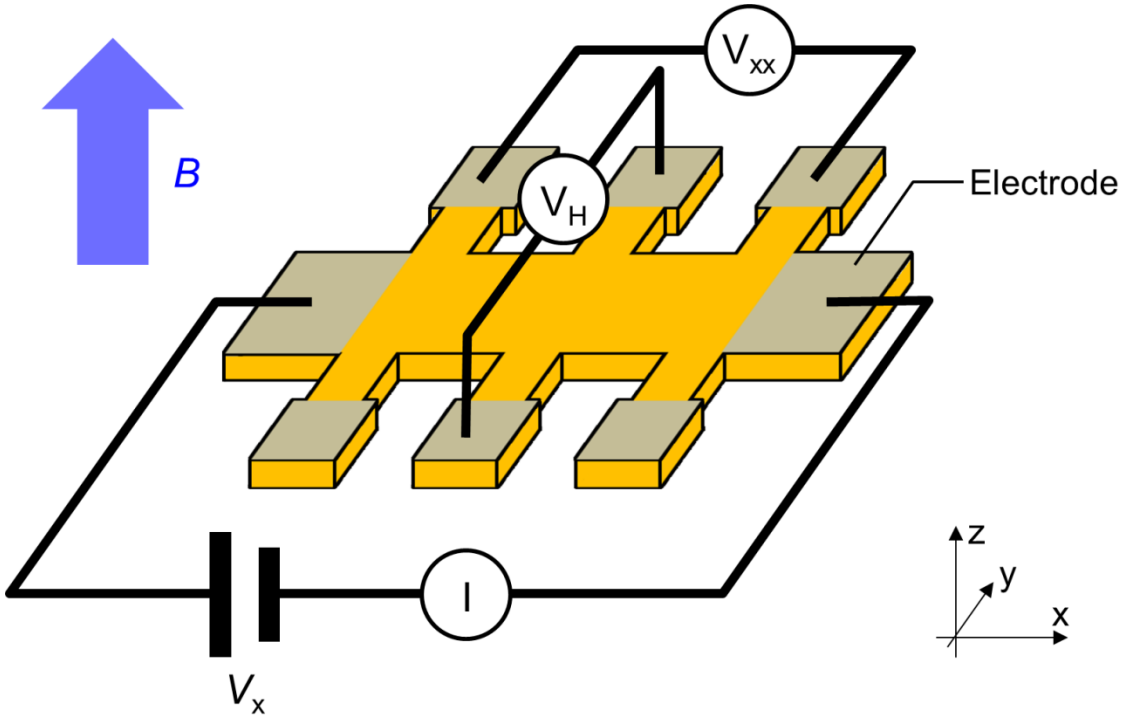

Figure 21. Setup of Hall effect measurement on a patterned sample.

direction on the carriers. In the steady state, the Lorentz force is canceled with the electric field caused by the gradation of carrier density in *y* direction. This electric field is called Hall field E_y and the situation can be described by the following equation.

$$\frac{E_y}{j_x B_z} = \frac{1}{nq} \tag{3.26}$$

where j_x, n and q are the current density in *x* direction, carrier density and charge of each carrier, respectively. By using the relationship $I_x = j_x wt$ (in which I_x is the current in *x* direction and *w* and *t* represent the width and thickness of sample) and definition of Hall coefficient $R_H = E_y/j_x B_z$, the following equation is derived.

$$V_H = R_H \frac{I_x B_z}{t} \tag{3.27}$$

where V_H is the voltage in *y* direction called Hall voltage. Thus, the carrier density can be calculated from the gradient of V_H vs B_z plot. The sign of R_{H} reflects the polarity of the carriers, that is, negative and positive values mean domination by electron and hall carriers, respectively.

Once the carrier density is obtained in Hall measurement, Hall mobility μ can be calculated from the following relationship.

$$\sigma = \frac{1}{\rho} = \mu nq \tag{3.28}$$

where σ and ρ are the conductivity and resistivity, respectively.

In this study, conductivity measurements were carried out on the films patterned in the shape shown in Figure 21 with masks. Control of sample circumstances was done by a Physical Property Measurement System (PPMS, Quantum Design).

3.6 Characterization on anion arrangement

3.6.1 Polarized X-ray absorption spectroscopy [107–109]

X-ray absorption spectroscopy (XAS) is an analysis method on electronic states and local structures of materials. When a sample is irradiated with X-ray, the X-ray is absorbed if it has energy enough to excite electrons from inner core to unoccupied states or out of the binding potential. XAS spectra can be categorized into the two regions: X-ray absorption near edge spectra (XANES) and extended X-ray fine structure (EXAFS) regions. The former is the region lower than about 50 eV from the edge and has fine structure reflecting the excitation process from an inner core to unoccupied density of states (DOS) around Fermi energy. The latter occurs when electrons are emitted from the observed atoms and scattered by the surrounding atoms. XANES is applicable to investigate electronic states of the target atoms including the symmetry and valence, while EXAFS is sensitive to the surrounding environments such as the bond length and the kind of the coordinating species.

There are several detection ways of XAS signals including transmission, total electron yield (TEY) and total fluorescence yield (TFY) methods. Transmission method is the most basic though being not suitable for measurement using soft X-ray with energies less than 3.5 keV. TEY method detects the current flow from ground to the sample accompanied by the emission of electrons and is sensitive to surface region. TFY method is bulk sensitive and detects the emitted photon caused by fluorescence when the excited electrons get back to the opened inner core level.

XAS spectra do not always reflect unoccupied DOS due to the dipole selection

rule of excitation. For example, K core electrons of oxygen are allowed to be excited only to the states with *p* characteristics in order to keep the angular momentum. The rule raises polarization dependence of X-ray absorption. In the case of thin film specimens with (pseudo-)cubic perovskite oxide with [100] orientation, axial and equatorial anion sites bonded to *B*-site cations exist in the directions vertical and parallel to the surface, respectively. In the excitation from O1*s* to t_{2g} orbital of *B* cation, polarized light in the out-of-plane direction is absorbed only by the oxygen ions in the equatorial site while the axial site oxygen ions absorb light polarized in the in-plane direction because they hybridize in π-bonding/antibonding manner. The situation is opposite in the excitation process from O1*s* to e_g states because of the σ bonding/antibonding hybridization.

In this study, site occupancy of oxygen and nitrogen ions was investigated using the polarization dependence of X-ray absorption. Figure 22 show the setting of the measurement. The samples were tilted at 75° to the incident plane of X-ray and irradiated with vertically and horizontally polarized X-ray. The former has 100%

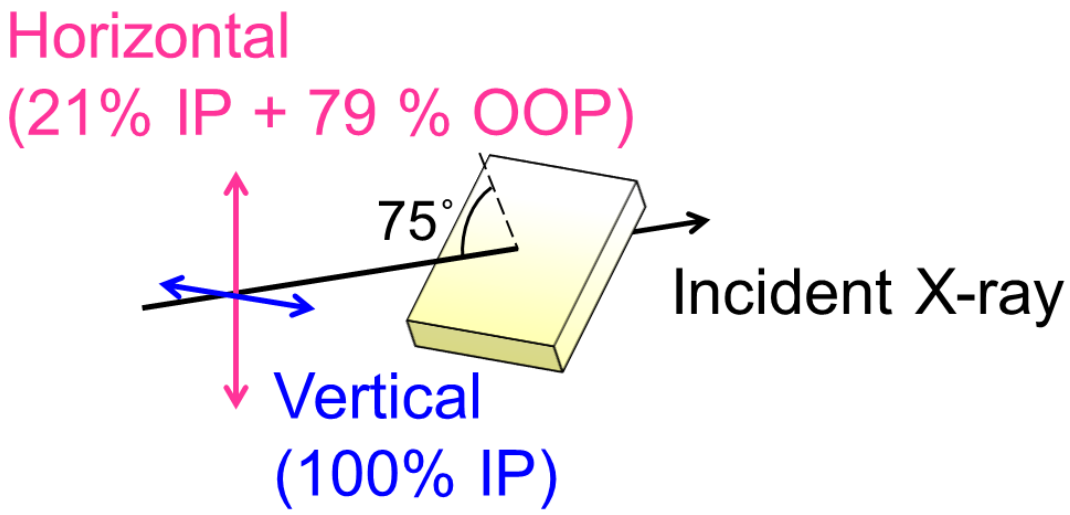

Figure 22. Setup of polarized XAS measurement used in this study.

polarization in the in-plane direction of the samples while the latter is composed of 21% of in-plane polarized light and 79% of out-of-plane one. Linear dichroism of K-edge spectra was used to estimate the differences in site occupancy of nitrogen and oxygen. The measurement was performed on beamline BL-27SU of Spring-8.

3.6.2 Electron energy loss spectroscopy combined with scanning transmission electron microscope [110,111]

Electron energy loss spectroscopy (EELS) is frequently used for composition analysis. Samples are irradiated with electron beam and the energy loss caused by the excitation of inner core electrons is measure in spectroscopic manner. Because the energy loss is dependent on the kind of element, EELS can determine the composition of a particular region of samples by combining electron microscope. Differently from energy dispersive X-ray analysis, in which electron beams are used as well, EELS measurement has sensitivity to light elements including oxygen and nitrogen.

In this study, EELS was measured combined with HAADF-STEM in a site-selective way to investigate the site occupancy of nitrogen and oxygen at axial and equatorial sites in a perovskite oxynitride thin film.

Chapter 4

Epitaxial growth of perovskite oxynitrides*

4.1 Introduction

In this chapter, I demonstrate epitaxial growth of perovskite oxynitrides by the technique of nitrogen plasma assisted pulsed laser deposition (NPA-PLD). I optimized the growth condition of $SrTaO_2N$ (a = 4.03 Å in a pseudo-cubic approximation [11]) epitaxial thin films through a series of investigations on nitrogen content and crystal structure of the films prepared by changing growth parameters. The technique was furthermore extended to epitaxial growth of another perovskite oxynitride, $CaTaO_2N$ (a = 3.9477 Å in a pseudo-cubic approximation [11]). The quality of the obtained thin films was examined by dielectric capacitance measurements.

* This chapter contains the contents of the following publications.

1) D. Oka, Y. Hirose, T. Fukumura, and T. Hasegawa, Cryst. Growth Des. **14**, 87 (2013).

2) D. Oka, Y. Hirose, H. Kamisaka, T. Fukumura, K. Sasa, S. Ishii, H. Matsuzaki, Y. Sato, Y. Ikuhara, and T. Hasegawa, Sci. Rep. **4**, 4987 (2014).

4.2 Method

$SrTaO_{3-x}N_x$ thin films were prepared on the (100) plane of $SrTiO_3$ (STO) and Nb(0.5 wt%)-doped $SrTiO_3$ (NSTO) (a = 3.905 Å) single crystalline substrates with atomically flat surface (Shinkosha Co., Ltd.) by NPA-PLD using a KrF excimer laser (λ = 248 nm). A $Sr_2Ta_2O_7$ ceramic pellet was used as a target, which was prepared by a conventional solid-state reaction of Ta_2O_5 and $SrCO_3$ [112]. Nitrogen gas was activated by an electron cyclotron resonance (ECR) plasma source (Tectra, Gen2). The partial pressure of nitrogen gas (P_{N2}) was varied from ~1.00×10^{-7} to 1.00×10^{-4} Torr, and the substrate temperature (T_S) was set in a range from 500 to 800 °C. The film growth rate r was controlled by the laser repetition rate (0.3–20 Hz) and pulse energy (4–20 mJ). In the dielectric capacitance measurements, $SrTaO_2N$ films deposited on conductive NSTO substrates were used after the following two-step heat treatments for suppressing the leakage current: (1) annealing at 500 °C for 30 h under a gas mixture of nitrogen (P_{N2} = 1.00×10^{-5} Torr, activated by ECR) and oxygen (partial pressure of 2.00×10^{-5} Torr) and (2) annealing at 320 °C for ~500 h in air. The resultant changes in nitrogen content and lattice parameters produced by these treatments were negligible within the detection limits of nuclear reaction analysis (NRA) and X-ray diffraction (XRD), respectively.

$CaTaO_2N$ epitaxial thin films were also grown on (100) planes of STO substrates by NPA-PLD method. A $Ca_2Ta_2O_7$ ceramic pellet was used as a target, which was obtained by sintering $Ca_2Ta_2O_7$ powder at 1400 °C for 50 h. The $Ca_2Ta_2O_7$ powder was synthesized by conventional solid phase reaction of a stoichiometric mixture of Ta_2O_5 and $CaCO_3$ in an alumina crucible: The reaction was first conducted at 800 °C for 24 h and successively heated at 1000 °C for 24 h, and 1200 °C for 50 h. T_S and P_{N2} were

set at 800 °C and 1.0×10^{-5} Torr, respectively. N_2 gas was activated into radicals by a radio frequency (RF) plasma source (SVT Associates, Model 4.5") with input power of 250 W. The plasma source was equipped with a parallel plate capacitor (ion deflector) to remove ionic species from the plasma. The same KrF excimer laser as used in synthesis of the $SrTaO_2N$ films was operated at an energy density of 0.4 J cm^{-1} $shot^{-1}$ and a repetition rate of 20 Hz. Typical deposition rate was 10–20 nm/h. The growth mode of the thin films was monitored *in situ* by reflection high energy electron diffraction (RHEED). Dielectric capacitance measurement was conducted on the films grown on NSTO substrates as in the case of the $SrTaO_2N$ films. To suppress leakage current, the as-grown $CaTaO_2N$ thin films were further annealed at 500 °C for 30 h under a mixture of nitrogen (P_{N2} = 1.0×10^{-5} Torr, activated by the RF plasma source) and oxygen (partial pressure of 2.0×10^{-5} Torr) gas before the measurements.

The nitrogen content of the films was determined by NRA. Rutherford backscattering spectroscopy (RBS) was conducted on a representative thin film of $SrTaO_2N$ to check cation stoichiometry. A ^4He beam accelerated to 2 MeV was employed for the measurements. The incident and backscattering angles were set to 0° and 160°, respectively. The oxygen content was calculated from the nitrogen content by assuming charge neutrality. Crystal structures of the thin films were evaluated by XRD. Microstructure of the thin films was investigated by transmission electron microscopy (TEM) (JEOL Ltd., JEM-2010HC, 200 kV and Hitachi, H-9000NAR, 300 kV for $SrTaO_2N$ and $CaTaO_2N$, respectively). Observation of scanning transmission electron microscopy-high angle annular dark field (STEM-HAADF) image was conducted on the $SrTaO_2N$ epitaxial thin film for investigation on lattice structure in atomic scale with an aberration-corrected scanning transmission electron micrometer (JEOL Ltd.,

JEM-2100F). Surface morphology of the thin films was characterized with an atomic force microscope (AFM). Impedance measurements were conducted in the capacitor configuration of Pt/oxynitride/NSTO.

4.3 Results and discussion

4.3.1 Preparation of $SrTaO_{3-x}N_x$ epitaxial thin films

In this thesis, the chemical composition of the Sr-Ta based films was expressed as $SrTaO_{3-x}N_x$ despite the possible deviation of the total anion content in the formula unit from 3. This is because the perovskite structure was maintained over a wide range of x values (see Fig. 25).

The dependence of the nitrogen content x in the $SrTaO_{3-x}N_x$ films on the growth parameters was investigated by NRA. As shown in Fig. 23a, x was highly sensitive to P_{N2} and reached a maximum at $P_{N2} = 1.0 \times 10^{-5}$ Torr, where the largest concentration of N radicals would be supplied. N radicals were deactivated at higher P_{N2}, which is likely due to recombination in the electron cyclotron resonance plasma source and chamber. The nitrogen content increased from 0 linearly up to ~1.2 with respect to the inverse of deposition rate r (Fig. 23b). This result is reasonable as the supply rates of the other elements (Sr, Ta, and O) from the target were proportional to the deposition rate. This rate was determined by the pulse energy and repetition rate of the excimer laser, while the supply of N radicals was held constant. Meanwhile, x was almost independent of T_S (Fig. 23c), implying that the growth temperature used in this

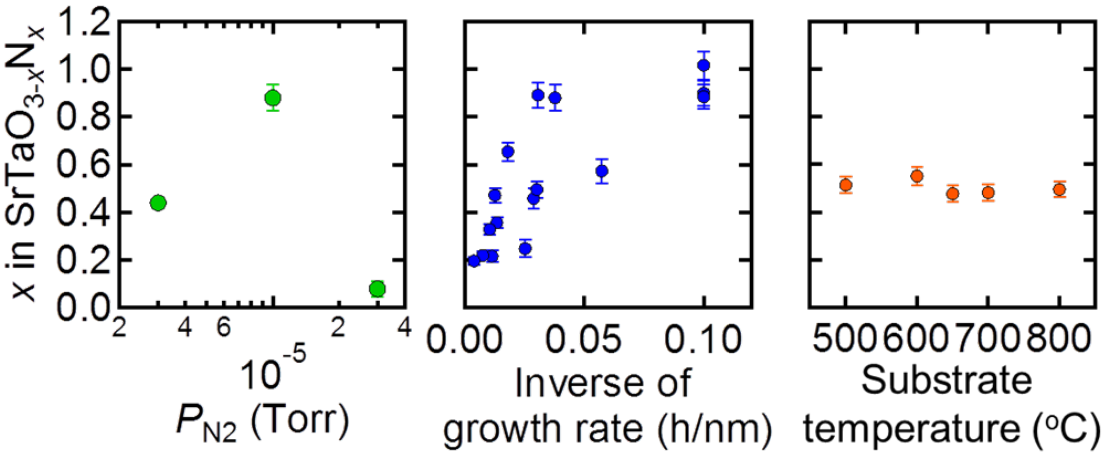

Figure 23. Dependence of nitrogen content on (a) partial pressure of nitrogen P_{N2} (substrate temperature T_S = 800 ºC, deposition rate r ~ 0.04 h/nm), (b) r (P_{N2} = 10^{-5} Torr, T_S = 800 ºC), and (c) T_S (P_{N2} = 10^{-5} Torr, r ~ 0.04 h/nm).

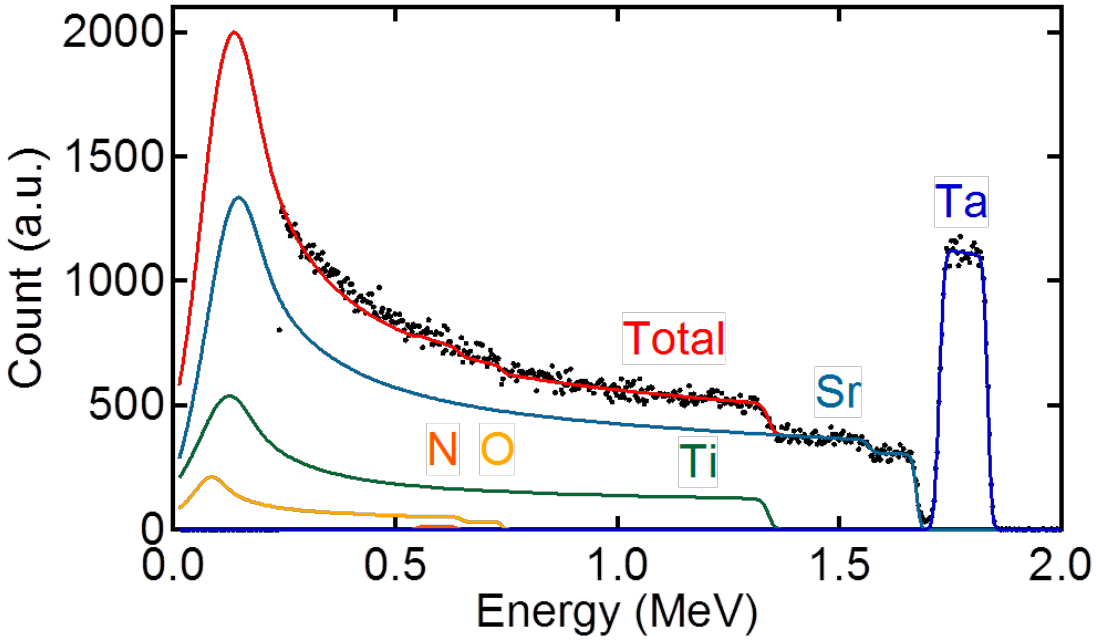

Figure 24. RBS spectrum of the $SrTaO_2N$ thin film.

study was too low to activate N_2 molecules.

Figure 24 shows a ^{4}He-RBS spectrum of a film whose nitrogen content x was evaluated as almost unity. The solid lines are the result of fitting performed with SIMNRA software [113]. The Sr/Ta ratio determined by the fitting was 0.98, with an error of less than 5% and cation stoichiometry was confirmed. The anion contents obtained by the fitting are unreliable due to their small cross sections.

Figure 25 shows the 2θ-θ XRD patterns of the $SrTaO_{3-x}N_x$ films with different nitrogen content x. All of the diffraction peaks from the films are assignable to the perovskite structure of $SrTaO_{3-x}N_x$. The result indicated that pure perovskite $SrTaO_{3-x}N_x$ films grew epitaxially on the STO substrates despite the wide variation in nitrogen content x with exceptions at x is equal to 0 and over 1. In the XRD pattern of the film without nitrogen (x = 0), diffraction from the (101)-oriented perovskite structure was sometimes observed. Although the detailed growth mechanism is unclear, a cation-deficient perovskite structure may be grown epitaxially. In contrast, tantalum nitride was sometimes observed in the films when an excess of nitrogen was present, causing electrical conductance.

The tetragonal lattice parameters, a and c, and the unit cell volume, V, of the $SrTaO_{3-x}N_x$ thin films monotonically increased with increasing x (Fig. 26). Near the stoichiometric composition [x = 1.02(6)], I observed a V of 65.385 Å^3, agreeing well with the reported lattice volume of bulk $SrTaO_2N$ (65.478 Å^3). The cation stoichiometry of this film was confirmed by RBS. In addition, I confirmed the bandgap energy of 2.27 eV (Fig. 27) determined from a plot of $(\alpha h\nu)^2$ versus $h\nu$, which agreed well with a previously reported value (2.3 eV) [11]. I hereafter refer to $SrTaO_{3-x}N_x$ thin films with nitrogen compositions of x = 1.00 ± 0.06 as $SrTaO_2N$ and will discuss the crystal

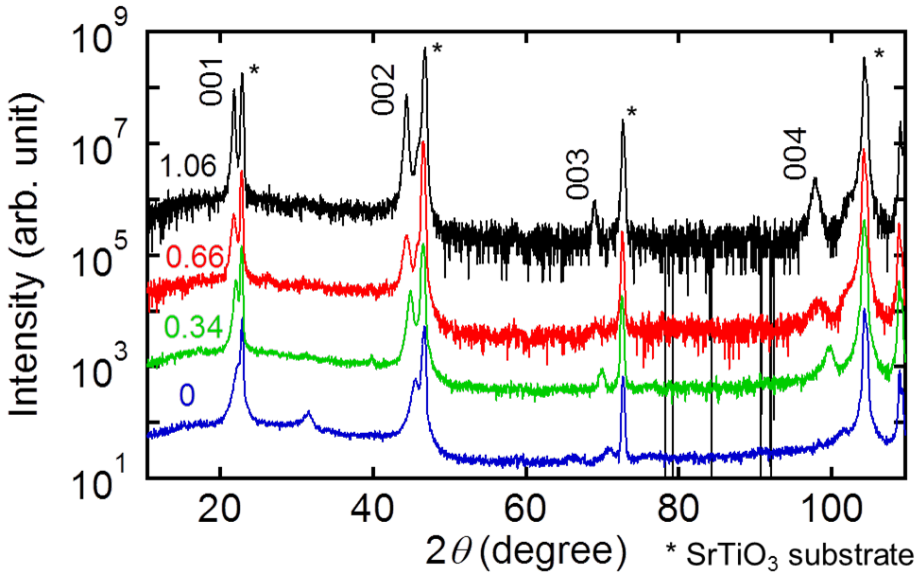

Figure 25. 2*θ*-*θ* XRD patterns of the $SrTaO_{3-x}N_x$ thin films for nitrogen content x = 0, 0.34, 0.66, and 1.06.

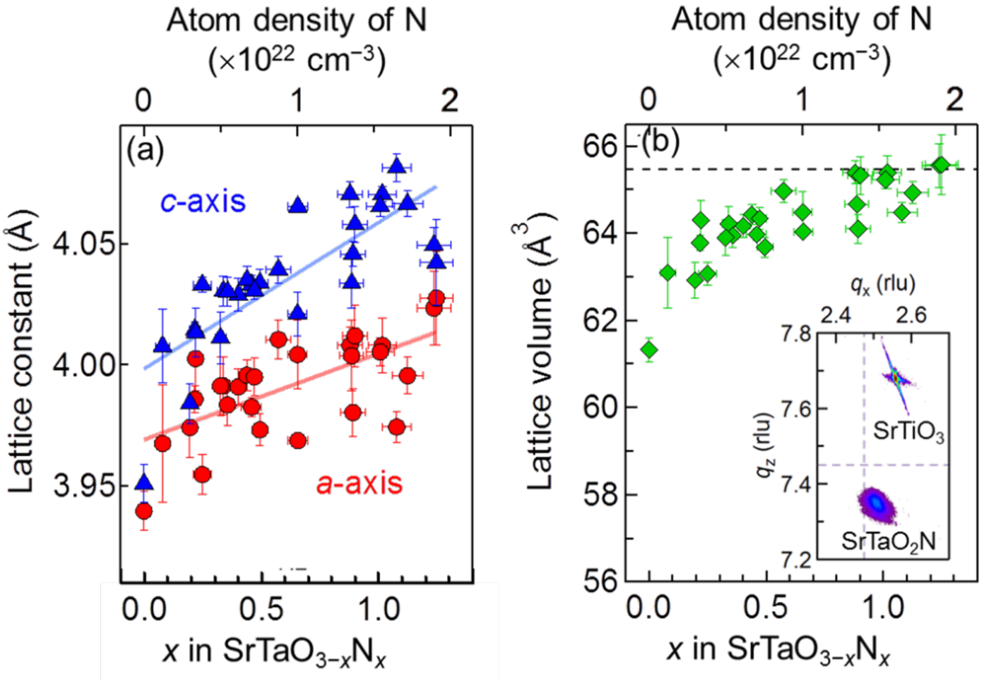

Figure 26. (a) In-plane (circles) and out-of-plane (triangles) lattice constants of the $SrTaO_{3-x}N_x$ thin films as a function of nitrogen content, x. (b) Lattice volume calculated from (a). The dashed line shows the lattice volume of bulk $SrTaO_2N$ [11]. The inset shows a RSM of the 103 diffraction of the $SrTaO_2N$ thin film and STO substrate. The dotted lines represent the lattice constant of bulk $SrTaO_2N$ [11].

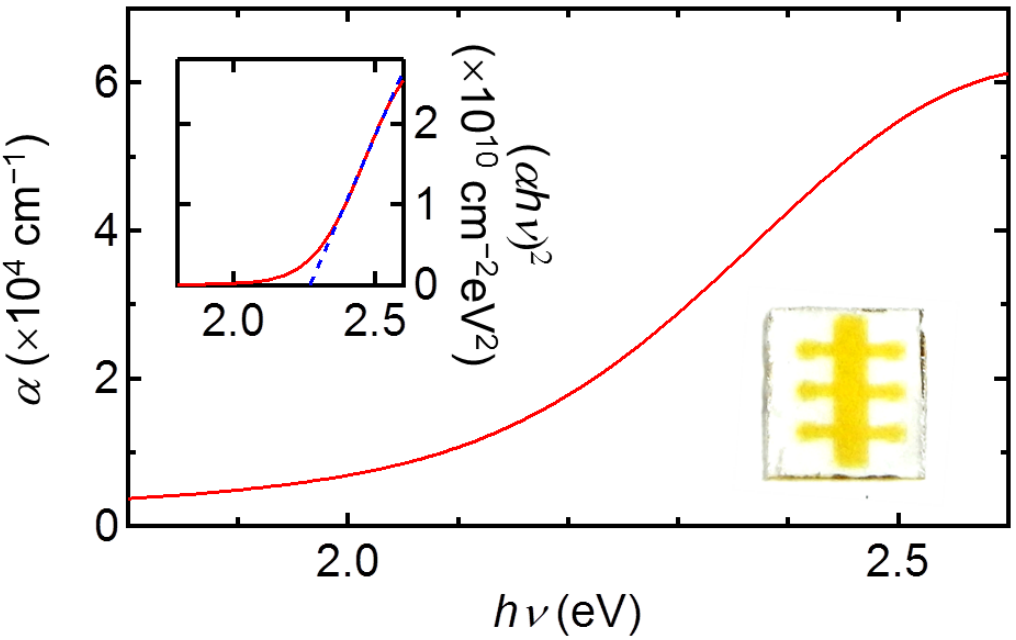

Figure 27. Absorption coefficients of $SrTaO_2N$ epitaxial thin film. The left inset is a Tauc plot. The right inset is a photograph of a patterned $SrTaO_2N$ thin film grown on a $SrTiO_3$ substrate.

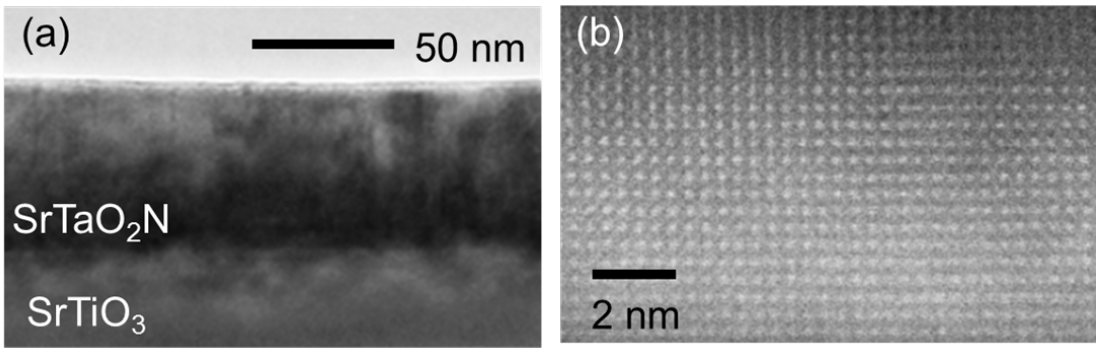

Figure 28. (a) Low-magnification cross-sectional TEM and (b) High-magnification HAADF-STEM image of the $SrTaO_2N$ film thin film.

structure and physical properties of the stoichiometric $SrTaO_2N$ films.

Investigating the microstructure of the $SrTaO_2N$ films using transmission electron microscopy (TEM; Fig. 28a) and high-angle annular dark field scanning TEM (HAADF-STEM; Fig. 28b), I found a sharp film/substrate interface and a uniform perovskite lattice structure with no segregation. Using XRD, I investigated the tetragonal lattice distortions of the $SrTaO_2N$ thin films. Despite the partially relaxed lattice of the thin films (the representative reciprocal space map shown in the inset of Fig. 26b), the tetragonal distortion ratio of c/a reached 1.026 (a = 3.98 Å; c = 4.08 Å) at a film thickness of 20 nm. The c/a ratio decreased with increasing film thickness, becoming nearly constant (~1.013) in the films thicker than 100 nm. These results indicate that the $SrTaO_2N$ epitaxial thin films were highly strained and distorted, especially near the film/substrate interface, compared with bulk $SrTaO_2N$ (c/a = 1.002 [11]). I also confirmed that $SrTaO_2N$ epitaxial thin films were perfectly relaxed (c/a = 1.002) on $(LaAlO_3)_{0.3}(Sr_2AlTaO_6)_{0.7}$ substrate (a = 3.868 Å) with larger lattice mismatch (−4.0%) than STO.

A streaky diffraction pattern was observed in RHEED measurement after complete of deposition with the optimized condition, though oscillation of the peak intensity was not seen during the deposition, indicating that the $SrTaO_2N$ thin films grew in island growth mode. In fact, an AFM image showed formation of square shaped grains on the surface (see Fig. 38). The relatively flat surface on each grain was consistent with the streak pattern in RHEED. It is plausibly due to the large mismatch between $SrTaO_2N$ and STO that the films did not grew in layer-by-layer growth mode despite the relatively high growth temperature.

4.3.2 Preparation of $CaTaO_2N$ epitaxial thin films

Next, I attempted to apply the NPA-PLD method for growth of another perovskite oxynitride, $CaTaO_2N$, in order to examine the versatility of the technique. As mentioned above, the film growth was performed just by changing the composition of target material and some variable parameters slightly.

Figure 29a shows RHEED intensity oscillation during the deposition. Clear oscillation continued for at least 15 cycles, indicating layer-by-layer growth of the epitaxial $CaTaO_2N$ thin films contrastively to the case in the $SrTaO_2N$ epitaxial thin films. The streak-shaped diffraction pattern was still observed after the deposition (Fig. 29b), assuring good crystallinity and flat surface of the films. As shown in the AFM images (Fig. 30), the surface of the $CaTaO_2N$ thin films was indeed atomically flat with a step-and-terrace structure, though small islands were recognizable in the wide-scan image. The RMS roughness evaluated from Figure 30a was 0.14 nm, which is much less

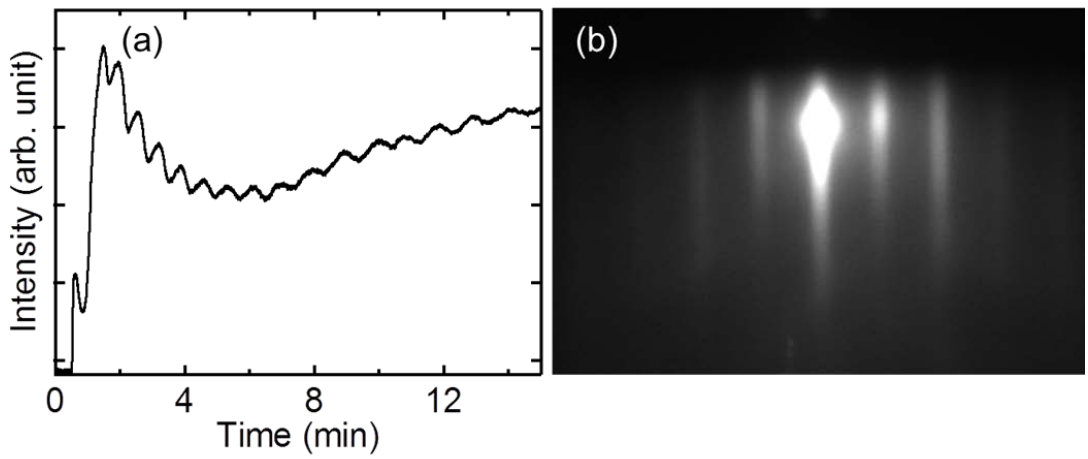

Figure 29. (a) RHEED intensity oscillation during the deposition of $CaTaO_2N$ thin film on STO substrate. (b) RHEED pattern of $CaTaO_2N$ thin film after deposition.

than that of the $SrTaO_2N$ thin film (2.0 nm). The step height calculated from the cross-section (Figure 30c) was ~0.4 nm, corresponding very well to the length of a $CaTaO_2N$ pseudo-cubic unit cell. As far as I know, this is the first report of layer-by-layer growth of a perovskite oxynitride thin film with atomically flat surface. The chemical composition of the $CaTaO_2N$ thin films was determined as $CaTaO_{1.94(11)}N_{1.04(7)}$, which is essentially stoichiometric within experimental error.

Figure 31 shows the typical 2θ-θ profile of a $CaTaO_2N$ film grown on a Nb-doped STO (001) substrate. Only the 00*h* diffractions of perovskite $CaTaO_2N$ were

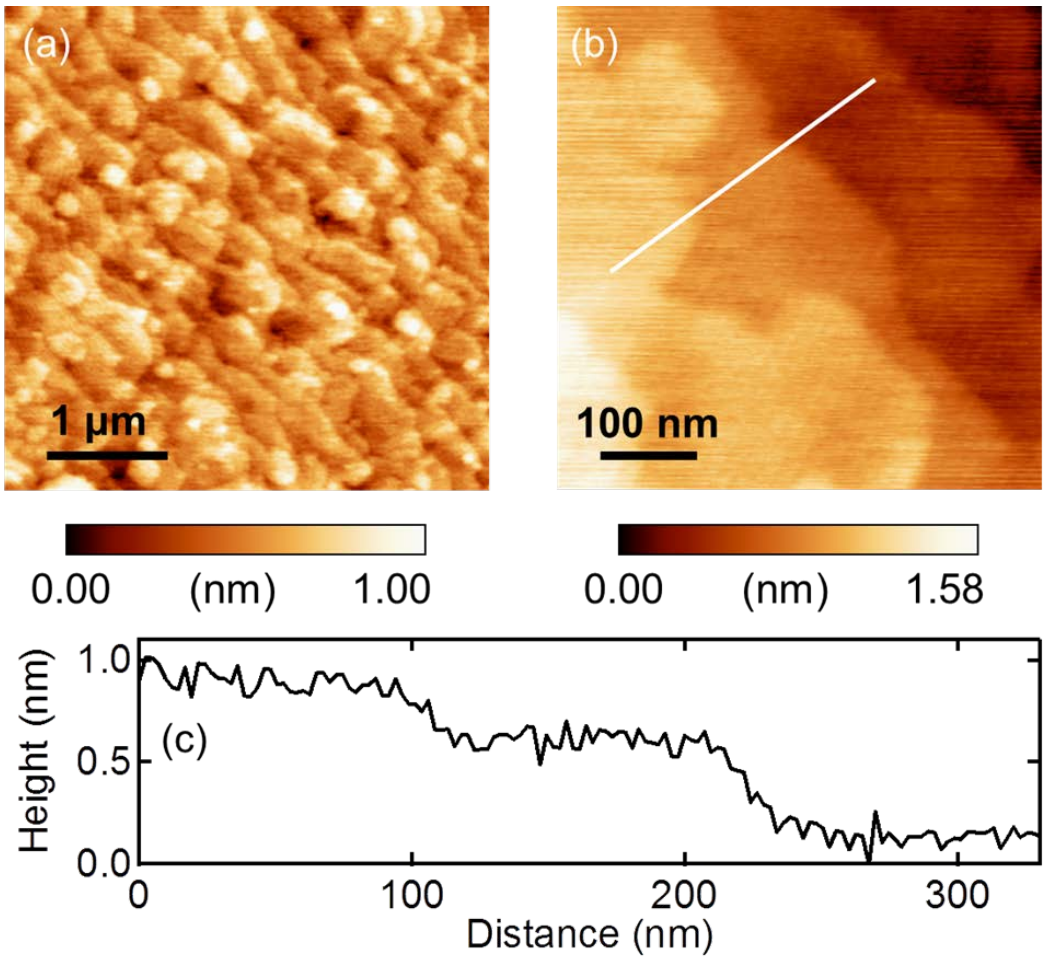

Figure 30. (a, b) AFM images of $CaTaO_2N$ epitaxial thin film on Nb-doped STO substrate at different length scales. (c) Line profile along the white line in (b).

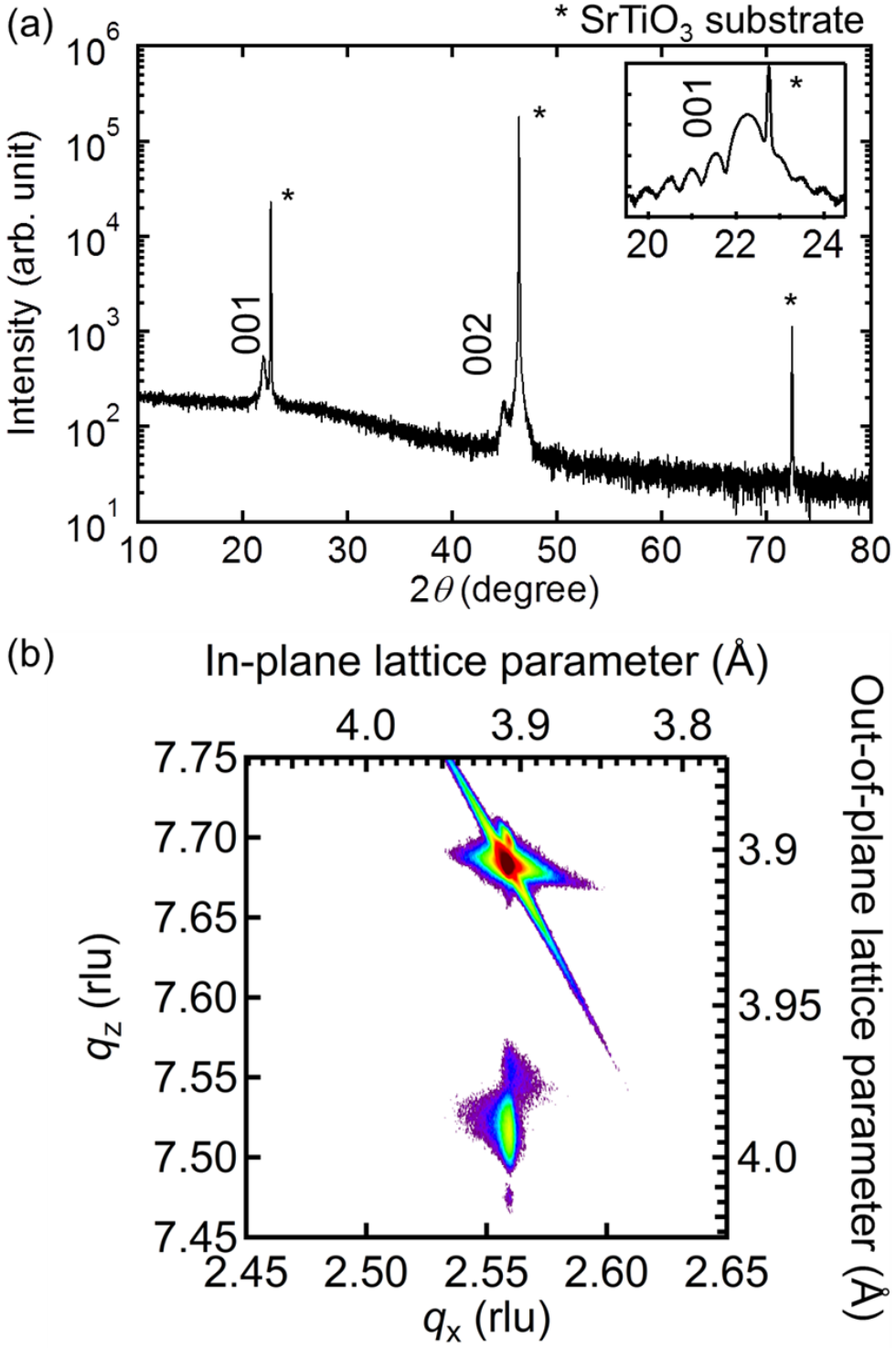

Figure 31. (a) XRD θ–2θ profile of $CaTaO_2N$ epitaxial thin film on Nb-doped STO substrate. Inset shows the fringe pattern around the 001 diffraction. (b) XRD RSM around the 103 diffractions of $CaTaO_2N$ epitaxial thin film and Nb-doped STO.

observed, with no impurity peaks. Asymmetric reflection measurements of *h*0*h* diffractions also confirmed the growth of phase-pure perovskite $CaTaO_2N$ (data not shown). The fringe pattern around the 001 diffraction in the high-resolution 2θ-θ profile (inset of Figure 31a) reveals a sharp interface between the films and substrates. The full width at half-maximum (FWHM) value of the rocking curve of the 001 diffraction was 0.02°, which demonstrates the high crystallinity of the films. In order to investigate the epitaxial strain on the $CaTaO_2N$ films in more detail, XRD-RSM was measured around the 103 diffraction. The obtained RSM image shows tetragonal distortion of the $CaTaO_2N$ films caused by the compressive strain from the STO substrate (Fig. 29b). The lattice parameters of the $CaTaO_2N$ films, evaluated from the RSM, were a = 3.905 Å and c = 3.99 Å. Note that the in-plane lattice constant was perfectly locked to the STO substrate; that is, the $CaTaO_2N$ films were coherently grown on STO. The *c*-axis length is much longer than the values deduced from lattice constants of bulk $CaTaO_2N$ ($a/\sqrt{2}$ = 3.97320 Å, $b/2$ = 3.94655 Å, $c/\sqrt{2}$ = 3.92358 Å [11]), which also validates the epitaxial stress from the substrates.

This is in sharp contrast to the $SrTaO_2N$ epitaxial thin films (a = 4.03 Å in a pseudo-cubic approximation, −3.1% mismatch), which was partially relaxed from the STO substrate. Similar lattice relaxation was also reported in $BaTaO_2N$ epitaxial thin films (a = 4.113 Å) grown on $SrRuO_3$-buffered STO substrate (a = 3.95 Å in a pseudo-cubic approximation, −4.1% mismatch) [61]. Thus, the coherent growth and resultant flat surface and high crystallinity appear to be related to the smaller lattice mismatch (−1.1%) between $CaTaO_2N$ and STO. I did not find any significant difference in surface morphology and crystal structure between the films grown on STO and Nb-doped STO.

The crystal growth manner and microscopic structure of the $CaTaO_2N$ thin films were cross-checked with cross-sectional TEM observations. The obtained TEM images (Figure 32) clearly exhibit sharp film/substrate interface and coherent growth of the $CaTaO_2N$ films without segregation of any secondary phases.

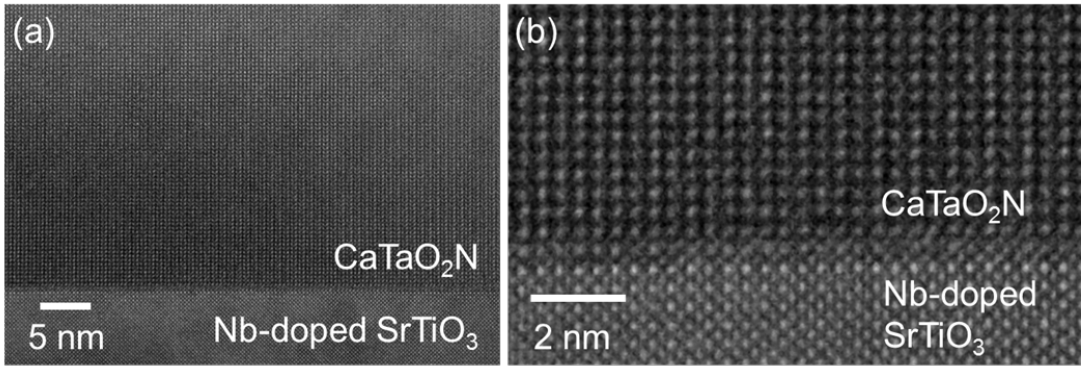

Figure 32. (a) Cross-sectional TEM image of $CaTaO_2N$ epitaxial thin film on Nb-doped STO substrate. (b) Magnified image of the film/substrate interface.

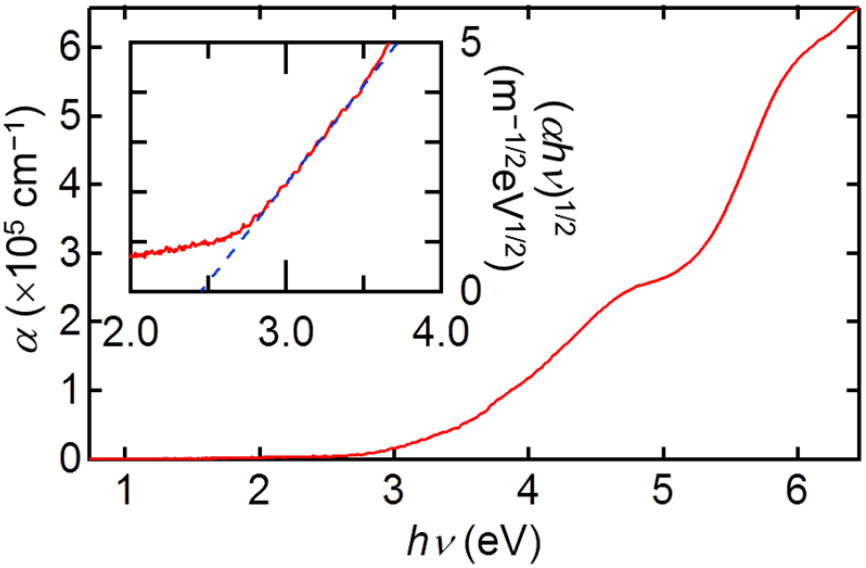

Figure 33. Spectral absorption coefficients of $CaTaO_2N$ epitaxial thin films on STO substrate calculated from optical extinction coefficients measured by spectroscopic ellipsometry. Inset shows the $(\alpha h\nu)^{1/2}$ vs $h\nu$ plots to determine the optical band gaps. Blue dashed line in the inset is the results of linear fitting.

Optical properties of the $CaTaO_2N$ thin films were investigated by spectroscopic ellipsometry. Figure 33 shows absorption spectra of the as-grown and annealed $CaTaO_2N$ thin films, where the absorption coefficient α was calculated from the optical extinction coefficient k using the equation (3.16). Although the detailed band structure of $CaTaO_2N$ has not been reported so far, good linear relations of the $(\alpha h\nu)^{1/2}$ vs $h\nu$ plots suggest that the absorption mechanism of our thin films is indirect transition (inset of Figure 33). The bandgap was determined as ~2.5 eV, which is in good agreement with the reported value of bulk specimen (2.4 eV) [11]. Notably, the bandgap value did not change at all after the annealing process to suppress leakage current, which ensures the nitrogen content was conserved.

4.3.3 Impedance measurement on $SrTaO_2N$ and $CaTaO_2N$ epitaxial thin films

I conducted impedance measurements on the $SrTaO_2N$ and $CaTaO_2N$ epitaxial thin films obtained with NPA-PLD to judge whether the quality of the films are high enough for reliable electrical measurement. As mentioned above, the films were subjected to the post-annealing treatments. Because the treatment caused increase in insulating property (resistance) without change in other film properties including crystal structure, nitrogen amount and optical absorption edge, I speculate that the process filled oxygen vacancies generated under the reductive growth conditions.

Figure 34 shows dielectric constant ε' and dielectric loss tan δ of the $SrTaO_2N$ epitaxial thin film with thickness of 288 nm measured at different temperatures and frequencies. The value of tan δ was less than 0.05 in almost all temperature and

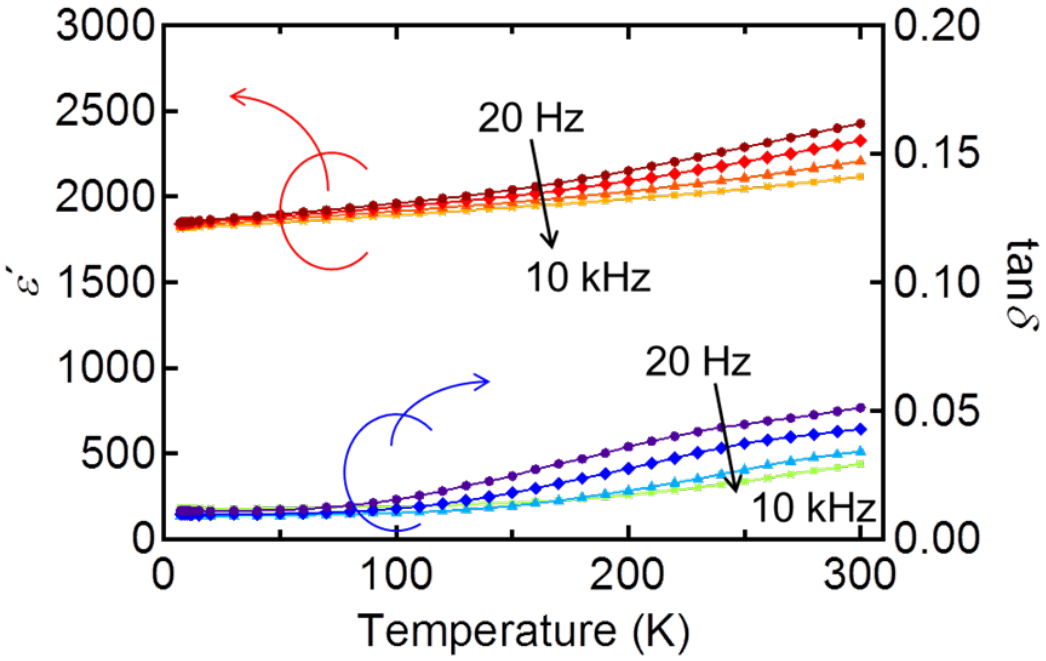

Figure 34. The dielectric constants and tanδ of the $SrTaO_2N$ film (thickness = 288 nm) measured at 20 Hz, 100 Hz, 1 kHz, and 10 kHz as a function of temperature

frequency range examined here, which indicates that the film had good insulating property and the measurements were conducted under a reliable condition with low influence of leakage current. Furthermore the value of ε' was approximately 2000, which is comparable to the reported value on bulk samples [11]. This is highly contrastive to the case of the previously reported $BaTaO_2N$ epitaxial thin films, which showed one order of magnitude lower dielectric constant value than bulk samples [61]. One possible explanation for the difference is that the $BaTaO_2N$ epitaxial thin film did not possess stoichiometric composition because no composition analysis was done in the report.

As for temperature dependence of ε', I found no significant signs of ferroelectric–paraelectric phase transitions up to 600 K, at which the sample began to be oxidized, as confirmed by XRD (data not shown). However, ε' exhibited positive $d\varepsilon'/dT$,

which is an opposite behavior to paraelectric materials including bulk $SrTaO_2N$ specimens and a common characteristic with conventional ferroelectric materials. This inconsistency between the films and bulk samples suggests that polarization properties differ between them, which will be discussed in more detail in the next chapter.

As for $CaTaO_2N$, it was suggested that the dielectric constant ($\varepsilon' \approx 30$) is much smaller than those of $SrTaO_2N$ or $BaTaO_2N$ ($\varepsilon' > 2000$) in the previous study on bulk specimens. However, the small dielectric constant of $CaTaO_2N$ was not very conclusive, because it was difficult to separate the bulk and grain boundary components of ε' in the impedance measurements. The effect of grain boundary should be negligible in the measurements on the epitaxial thin film. Figure 35 shows frequency dependence of ε' and tan δ of the $CaTaO_2N$ epitaxial thin film. The observed tan $\delta < 0.01$, is rather low compared with the previously reported values for perovskite oxynitrides

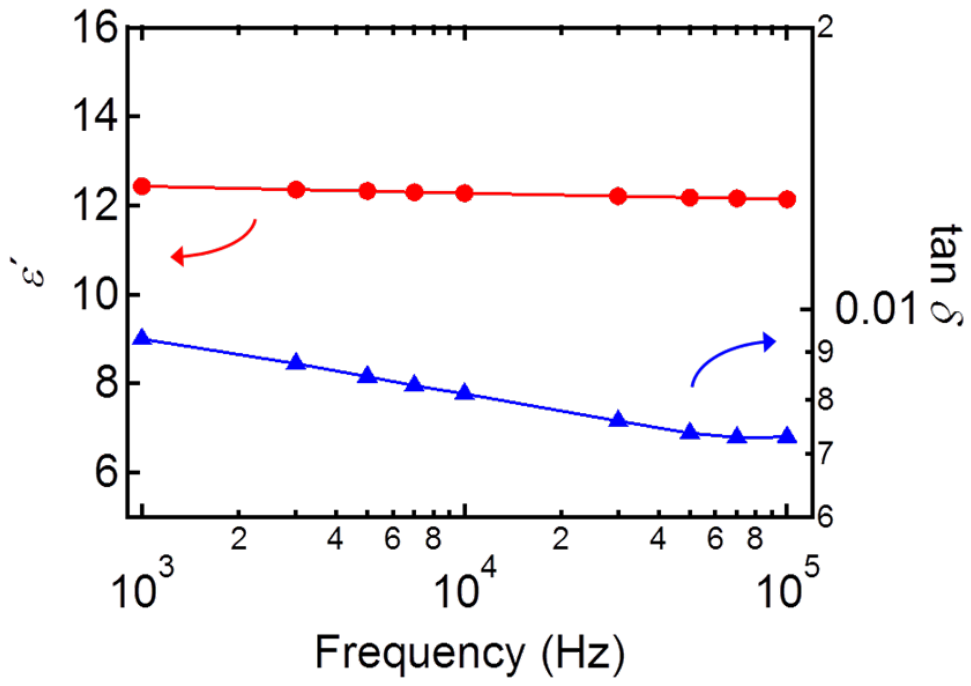

Figure 35. Frequency dependence of dielectric constant (ε') (red circle) and tan δ (blue triangle) of the annealed $CaTaO_2N$ epitaxial thin film on Nb-doped STO substrate.

[11,16,34,35,61]. The lower tan δ value than that of the $SrTaO_2N$ epitaxial thin film plausibly reflects the higher crystallinity due to the better lattice matching to NSTO substrate. Dielectric constant ε' of the $CaTaO_2N$ thin film was approximately 12, almost independent of frequency between 1 kHz and 100 kHz. This value is comparable to that of bulk $CaTaO_2N$ ($\varepsilon' \approx 30$), suggesting that the small ε' is intrinsic to $CaTaO_2N$.

4.4 Conclusion

I succeeded in heteroepitaxial growth of stoichiometric $SrTaO_2N$ and $CaTaO_2N$ thin films on STO substrates by a NPA-PLD method. Especially, the $CaTaO_2N$ films showed coherent growth with layer-by-layer mode resulting in high crystallinity, a sharp film/substrate interface and atomically flat surface. These features have not previously been achieved in epitaxial growth of perovskite oxynitrides. The high quality of the films enabled me to conduct reliable dielectric measurements with low dielectric loss (tan δ ~0.05 and <0.01 for $SrTaO_2N$ and $CaTaO_2N$, respectively). The dielectric constant of the $SrTaO_2N$ was in the same order as the extracted bulk component of that of the previously reported powder samples. The $CaTaO_2N$ also showed comparable values of dielectric constant to that measured on the bulk samples, validating the previous suggestion that the low dielectric constant is an intrinsic property of $CaTaO_2N$. NPA-PLD has been shown to be a powerful tool for heteroepitaxial growth of oxynitride thin films and adaptable to wide range of composition of oxynitrides as in the case of oxide film growth with PLD method. The high-quality thin films obtained by this method will allow us to study intrinsic electrical properties of oxynitrides, which

includes not only dielectric properties in insulating samples but also carrier transports in conducting ones.

Chapter 5

Ferroelectricity and anion arrangement in the $SrTaO_2N$ epitaxial thin films*

5.1 Introduction

The electronic functionalities of perovskite oxynitrides would be influenced by the geometrical configuration of O and N ions. As reviewed in chapter 2, researchers have argued that dielectric properties of ABO_2N are closely related to anion arrangement: for example, Page *et al*. suggested that ferroelectricity in *trans*-type anion-ordered $ATaO_2N$ (*A* = Sr and Ba) phases may be caused by the off-centre displacement of Ta ions [74]. They investigated this concept by theoretically studying the stability of phases with different nitrogen arrangements and space groups. However, *trans*-type phases in this system are less energetically stable than *cis*-type phases, and bulk $SrTaO_2N$ specimens have been confirmed to exhibit *cis*-type configurations (Fig. 36a). As suggested by Page *et al*., the ferroelectric *trans*-type phase would be stabilized

* This chapter contains the contents in the following publication.

D. Oka, Y. Hirose, H. Kamisaka, T. Fukumura, K. Sasa, S. Ishii, H. Matsuzaki, Y. Sato, Y. Ikuhara, and T. Hasegawa, Sci. Rep. **4**, 4987 (2014).

by compressive epitaxial stress because of induced tetragonal distortion (Fig. 36b). Such metastable ferroelectricity was not observed in an epitaxial thin film of compressively strained $BaTaO_2N$ deposited on a $SrRuO_3$-buffered $SrTiO_3$ (STO) substrate [61]. This lack of ferroelectricity was likely caused by the considerably relaxed $BaTaO_2N$ lattice, indicated by the small lattice distortion (c/a = 1.0099) generated by the large lattice mismatch (−4.7%) between the film (a = 4.1125 Å) and the $SrRuO_3$ buffer layer (a = 3.92 Å; pseudo-cubic approximation). Because the $SrTaO_2N$ epitaxial thin film prepared in this study showed larger distortion c/a (~1.026) due to the better lattice matching to the STO substrate (mismatch: −3.1%), I investigated their ferroelectric properties with piezoresponse force microscopy (PFM).

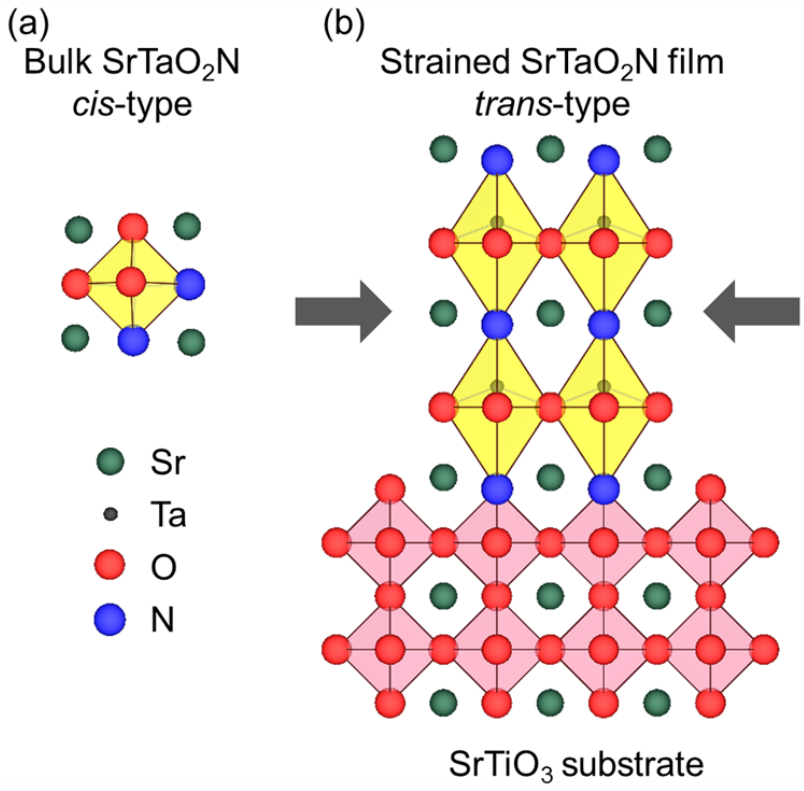

Figure 36. (a) Unstrained bulk $SrTaO_2N$ with a *cis*-type anion arrangement [32, 33]. (b) Tetragonally strained $SrTaO_2N$ thin film with a *trans*-type anion arrangement epitaxially stabilised on the $SrTiO_3$ substrate. The structures were drawn by VESTA [131]

5.2 Method

Atomic force microscopy (AFM) and PFM measurements were conducted using a scanning probe microscope (SII-nanotechnology, E-Sweep with NanoNaviReal) with a homemade PFM system composed of a function generator (NF corporation, 1930A) and a lock-in amplifier (EG&G, 7260). An Rh-coated silicon cantilever (SII-nanotechnology, SI-DF3-R(100) with stiffness of 1.1 N/m and a resonance frequency of 25 kHz in air) was employed for the measurements. In the PFM measurements, the frequency of the driving AC electric field was set to a value slightly (less than 1 kHz) deviated from the contact resonance (~110 kHz). The amplitude of the driving AC field was 1 V. A domain poling process was performed using the following three steps: (1) applying a sample bias of +7 V on the central 5 × 5 μm^2 area, (2) applying −7 V on the central 3 × 3 μm^2 area, and (3) applying +7 V on the central 1 × 1 μm^2 area.

High temperature X-ray diffraction (XRD) measurement was conducted with a four-axis diffractometer (Bruker AXS, d8 discover). The sample was placed in a domed hot stage (Anton Paar, DHS 1100) evacuated with a rotary pump (~10 Pa). To avoid oxidation, I capped the $SrTaO_2N$ epitaxial thin films used for high-temperature XRD with an amorphous $LaAlO_3$ layer (thickness of ~20 nm). The cap layer was deposited by pulsed laser deposition (PLD) at room temperature under a partial oxygen pressure of 3.1×10^{-3} Torr.

Phase stability of $SrTaO_2N$ under epitaxial stress was investigated with first principles calculation (by a collaborator). The potential energy surface (PES) was calculated using Vienna *ab initio* software package. The Perdew–Burke–Ernzerhof

(PBE) functional and projector-augmented wavefunction pseudopotential were adapted. The cut-off energy was 560 eV (41.2 Ry). The **k**-points were sampled according to the Monkhorst–Pack (MP) 8 × 8 × 8 for *Pbmm* and *P*4*mm* cells. The MP 8 × 8 × 8 was used for *I*4/*mcm*. The atomic positions were optimized until the residual force acting on all atomic coordinates was less than 0.01 eV/Å. The bottom of the PES was calculated by optimizing the size and shape of the unit cell and the atomic positions. The residual pressure was smaller than 0.035 GPa in all directions for all considered anion orderings.

5.3 Results and discussion

The ferroelectricity of the $SrTaO_2N$ thin films was investigated using contact-resonance mode vertical PFM (VPFM), which probes the out-of-plane piezoresponse of the film. VPFM measurements were conducted under vacuum (~10 Pa) at room temperature. In the virgin state, small domains (size range from tens to hundreds of nanometers) in the thin film produced much larger piezoresponse than did the surrounding regions (Fig. 37a and 37b). To investigate these locally varying ferroelectric properties, I performed switching spectroscopic measurements, in which I recorded the piezoresponse of the remanent polarization as a function of the amplitude of the preceding switching DC voltage pulse (Fig. 37c). The curves of local piezoresponse versus DC bias exhibited clear hysteresis (Fig. 37d) in the domains that exhibited large piezoresponse in the virgin state (point A in Fig. 37b). The amplitude components of the curve were butterfly shaped (Fig. 37e) and the phase components exhibited sharp 180° inversions at the coercive fields (Fig. 37f). These features denote

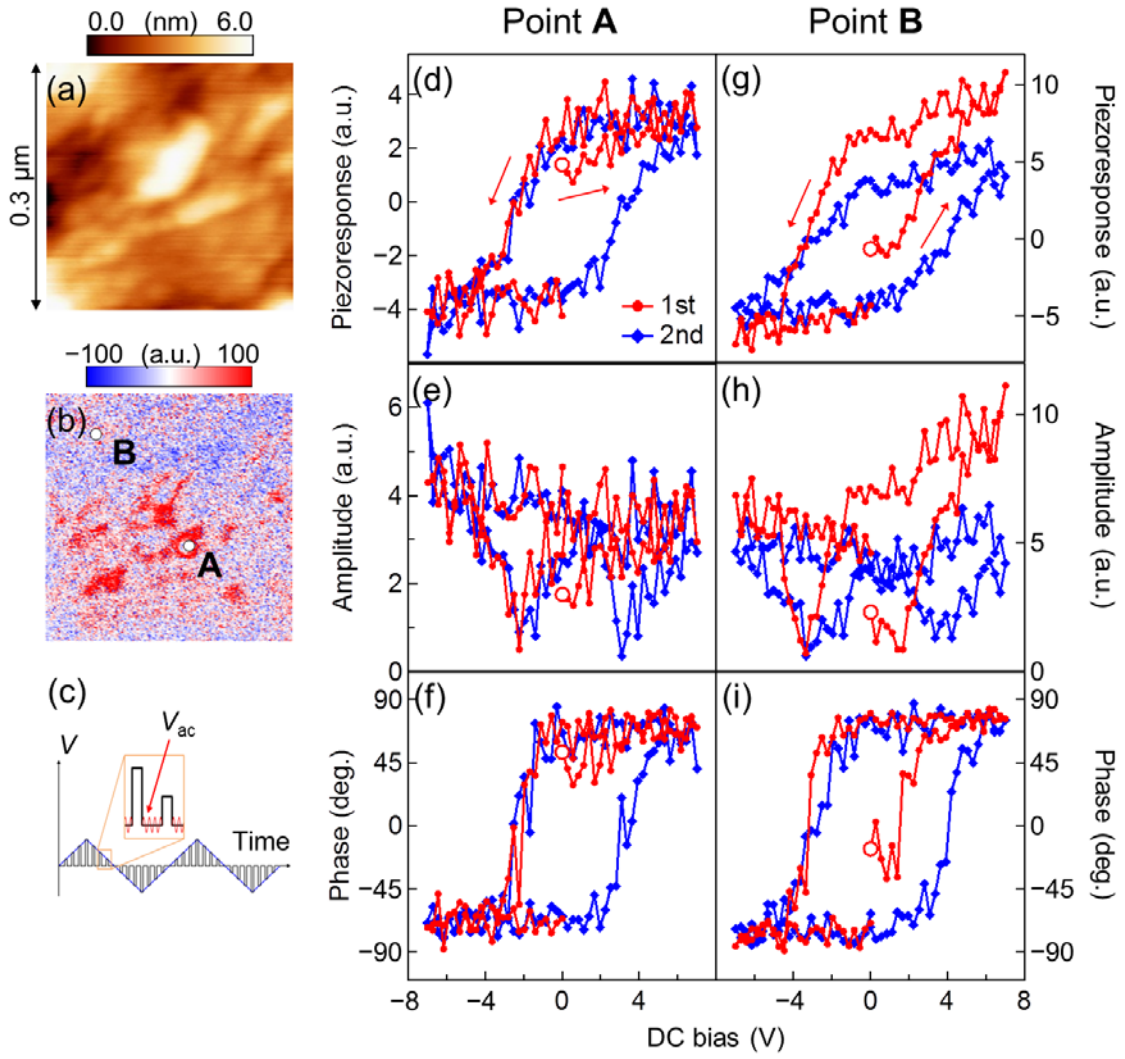

Figure 37. (a) Topographic and (b) piezoresponse (A cosθ) images of the $SrTaO_2N$ thin film (thickness = 288 nm). (c) Schematic illustration of the switching DC pulses and probing AC waves in switching spectroscopy measurements. After each DC pulse, the piezoresponse originating from the remanent polarisation is probed with a small AC bias. (d)–(i) Local piezoresponse examined by switching spectroscopy with an AC bias of ±1 V at positions A [(d)–(f)] and B [(g)–(i)] indicated in (b). Open circles represent the initial point of the measurements. (e), (f) and (h), (i) present the amplitude and phase components of (d), (g), respectively.

the presence of classical ferroelectricity, which has never before been observed in perovskite oxynitrides to our knowledge. The surrounding regions with negligible piezoresponse in the virgin state (point B in Fig. 37b) exhibited an apparent hysteretic piezoresponse induced by the external DC bias (Fig. 37g–37i). The piezoresponse of the $SrTaO_2N$ films was much weaker than those of conventional ferroelectric materials. The weaker response may have been caused by the small piezoelectric constant of $SrTaO_2N$, but it may also be possible that the region near the film/substrate interface was only ferroelectric because of lattice relaxation.

To investigate the unusual hysteretic behavior observed in the matrix region, I took a series of VPFM images from the same region over time after performing domain poling. In the virgin state before poling, the piezoresponse signals were hardly detectable (Fig. 38b) because the measured area was much larger than the size of the ferroelectric domains (tens to hundreds of nanometers). Immediately after poling, the induced piezoresponse was clearly different between the positively and negatively poled regions (Fig. 38e), and there was a 180° phase difference between the two distinct domains, indicating perfect polarization inversion (Fig. 38c and 38d). The induced polar domains began to relax within 1 h, and the contrast between the domains weakened considerably after 8 h (Fig. 38f– 38i); in contrast, the surface morphology did not change over time (Fig. 38a). Such relaxation behavior is typical in relaxor materials and has been observed in lead lanthanum zirconate titanate ceramics [114].

Interpreting these results must be done with caution, however: recent PFM studies on oxides reported that even paraelectric materials, such as TiO_2 thin films and heterostructures such as $LaAlO_3$/ $SrTiO_3$, can exhibit spurious relaxor-like behavior, caused by remanent piezoresponses generated from external-electric field-induced

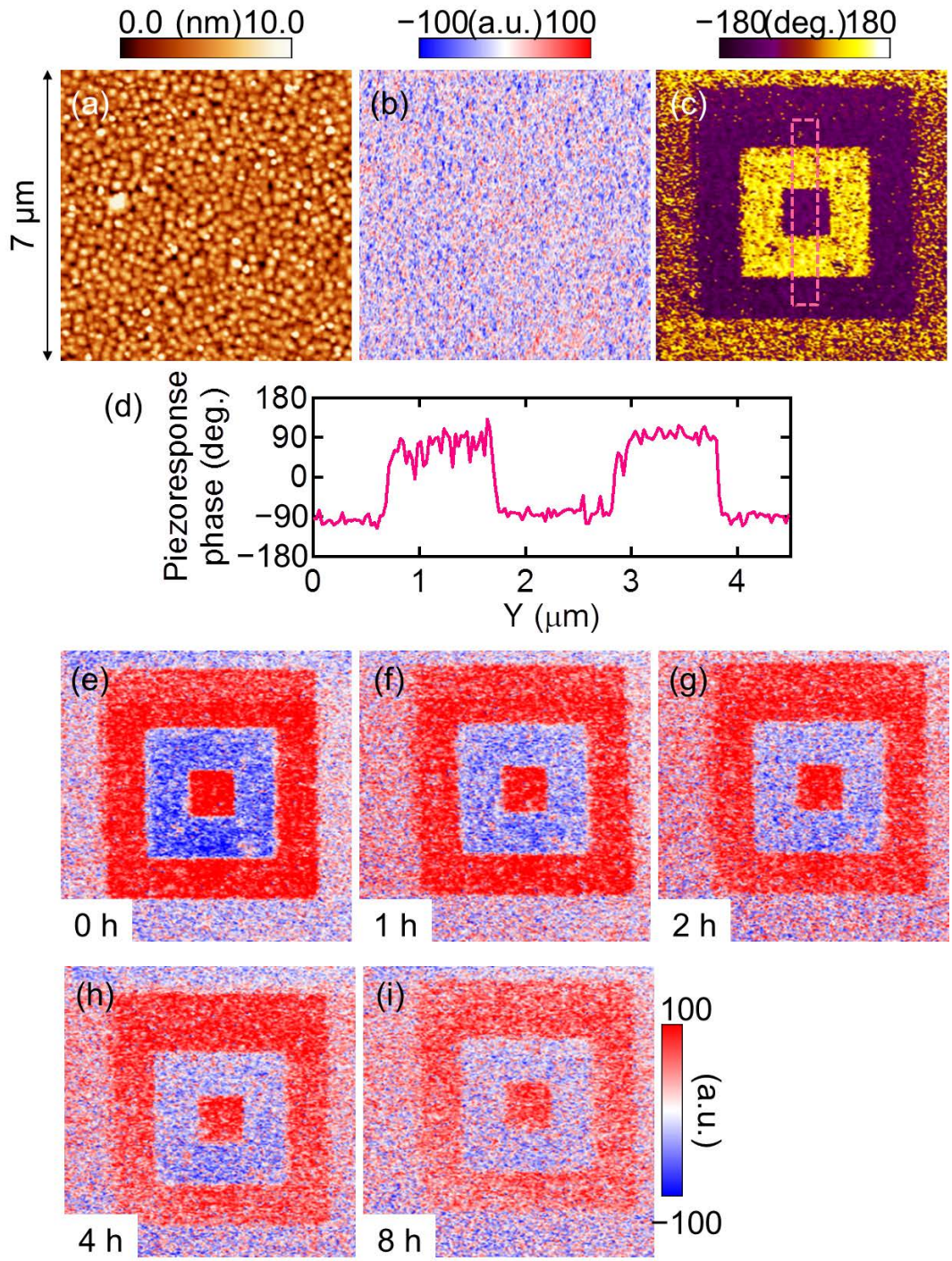

Figure 38. (a) Topographic and (b) piezoresponse (A cosθ) images obtained simultaneously from the $SrTaO_2N$ thin film (thickness = 288 nm) in the virgin state. (c) Phase images of the $SrTaO_2N$ film just after the poling process. (d) Averaged line profile of the dashed rectangle region in (c). (e)–(i) Piezoresponse images obtained from the same area as (c) 1, 2, 4, and 8 hours after the poling process.

motion of ionic species [115,116]. As for this point, we can see difference between the $SrTaO_2N$ epitaxial thin film and the paraelectric materials in the temperature dependence of dielectric constant. As mentioned in Chapter 4, the real part of the dielectric constant showed positive $d\varepsilon'/dT$, which is a common behavior with conventional ‘‘intrinsic’’ relaxors [117]. In contrast, in ‘‘extrinsic’’ relaxors, $d\varepsilon'/dT$ tends to decrease with increasing temperature [118]. Thus, I tentatively conclude that the majority of the present $SrTaO_2N$ film surrounding the small domains (i.e., the relaxor-like matrix region) is an intrinsic relaxor.

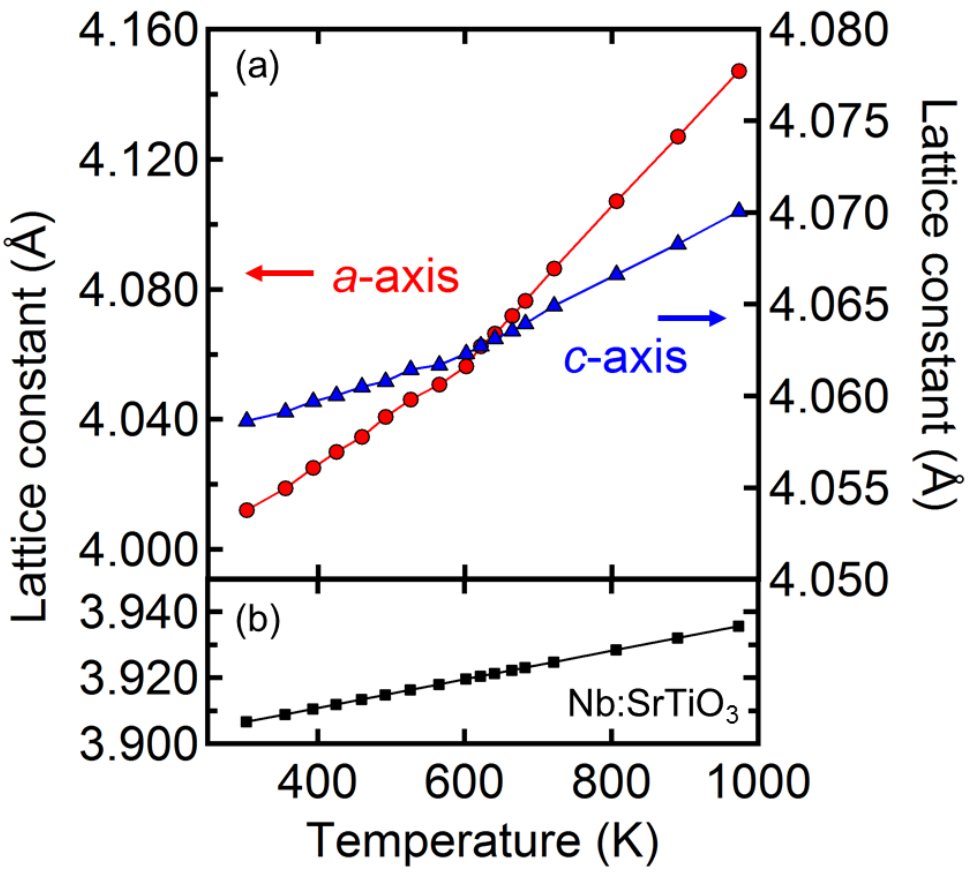

Figure 39. (a) The *a*- and *c*-axis lattice constants of the $SrTaO_2N$ film (thickness = 100 nm) capped with an amorphous $LaAlO_3$ protection layer and (b) simultaneously measured lattice constant of Nb-doped $SrTiO_3$ substrate as a function of temperature.

To investigate the possibility of ferroelectric–paraelectric phase transitions in the matrix region, high-temperature XRD was conducted. To avoid oxidisation, the $SrTaO_2N$ film was capped with ~20 nm of amorphous $LaAlO_3$. Figure 39 shows the measured lattice constants as a function of temperature, clearly indicating an inflection at ~600 K in both the *a*- and *c*-axis lengths. Choi *et al*. reported similar behavior in $BaTiO_3$ ferroelectric thin films at their Curie temperature [119], leading me to speculate that the inflection point in the present $SrTaO_2N$ epitaxial thin film corresponds to its Curie temperature.

Based on these findings, I believe that our $SrTaO_2N$ film contained classical ferroelectric domains (10^1–10^2 nm) and a surrounding matrix with a relaxor-like nature, although I observed hysteretic behavior only in the microscopic PFM measurements and could not obtain more direct evidence for ferroelectricity from macroscopic *P*-*E* measurements because of the large leakage current under high DC electric field (data not shown).

I discuss the origin of the classical ferroelectricity in the present films in the following part. It is plausible that the domains exhibiting classical ferroelectricity can be classified as the polar *trans*-type phase, considering that room-temperature ferroelectricity in the *cis*-type structures has never been observed, experimentally or theoretically. However, first-principles calculations performed by Hinuma *et al*. suggested that $SrTaO_2N$ with specific *cis*-type structures exhibits reversible polarization, although the polarization flips within picoseconds at room temperature [13]. Such a fluctuating polarization might be frozen by the epitaxial strain from the STO substrate, but the *ab initio* molecular dynamics simulations excluded the possibility of polarization freezing (Fig. 40). Thus, I attribute the classical ferroelectric behavior in the small

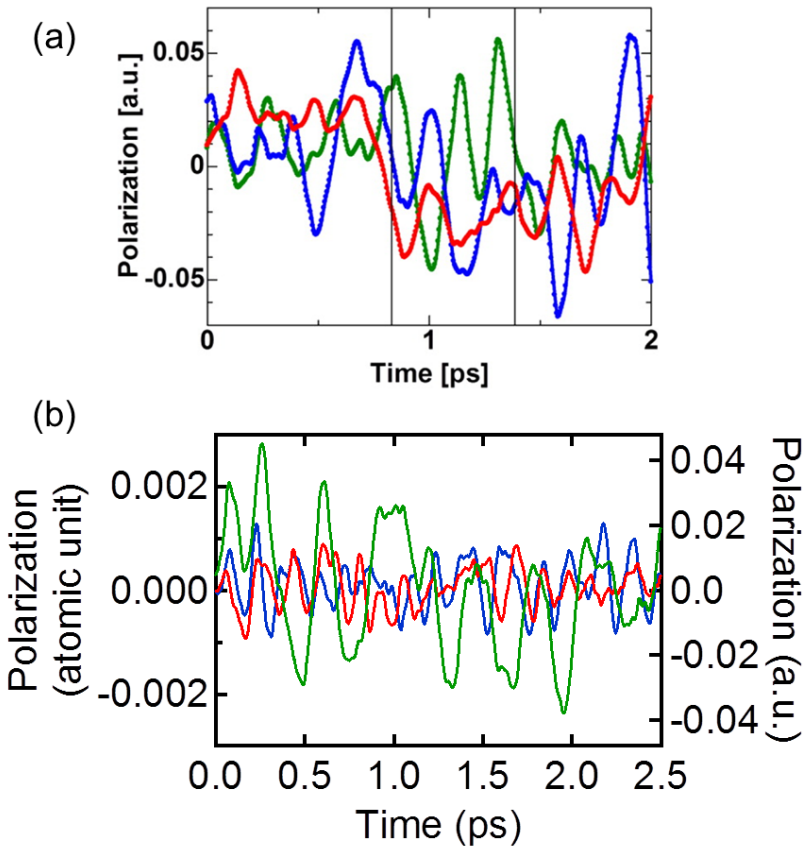

Figure 40. Polarization of the $SrTaO_2N$ cell during *ab initio* MD simulations at T = 300 K in (a) unstrained and (b) strained configurations [80]. The green, blue, and red lines indicate the polarisation in the *a*, *b*, and *c* directions at 300 K, respectively.

domains to *trans*-type N ordering.

Next, the epitaxial stabilization of the polar *trans*-type structure was validated by using DFT calculations. This concept was suggested by Page *et al.* [74] but not yet confirmed with concrete calculations. The energies of the three representative phases suggested by Page *et al.* were compared: paraelectric antipolar *cis*-type (space group symmetry: *Pbmm*), nonpolar *trans*-type (*I*4/*mcm*), and ferroelectric polar *trans*-type (*P*4*mm*) configurations (Table 5). Among these structures, the *cis*-type *Pbmm* phase was the most energetically stable, consistent with the calculation by Page *et al.*, although the

Table 5. Geometrically optimised crystal structures of *Pbmm cis*, *I*4/*mcm trans*, and *P*4*mm trans* models without strain. The total energy per formula unit of each structure relative to the most stable *Pbmm* phase, *E*, is also displayed.

	Pbmm cis	*I4/mcm trans*	*P4mm trans*
Polarity	antipolar	nonpolar	polar
a (Å)	5.81783	4.00435	4.00545
b (Å)	5.78146		
c (Å)	4.00811	4.12524	4.30080
E (meV)	0	216	211

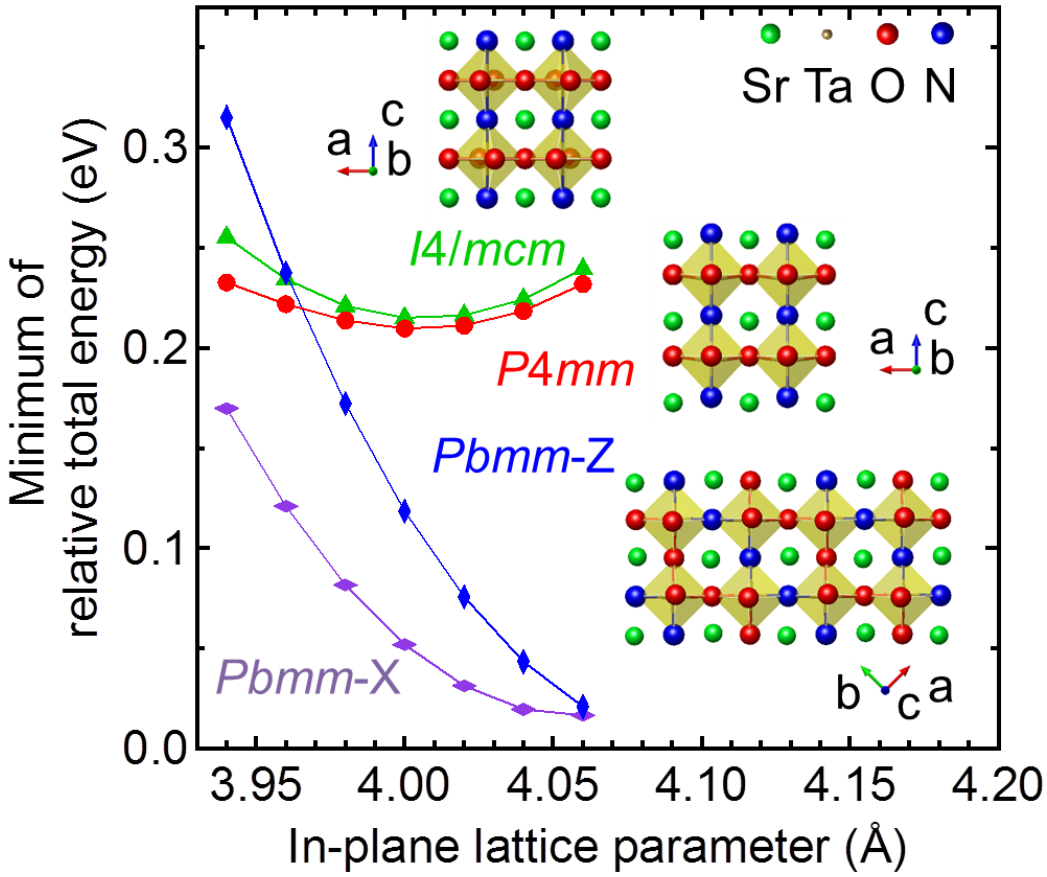

Figure 41. The total energy per formula unit of each structure, *E*, under epitaxial strain; *Pbmm cis* (diamonds, the [110] and [001] directions were assumed as the out-of-plane direction for *Pbmm*-X and *Pbmm*-Z, respectively), *I*4/*mcm trans* (triangles), *P4mm trans* (circles).

absolute values of the energy difference among these structures were not completely reproduced. Figure 41 shows how the epitaxial stress affected the phase stability, calculating the potential energies as functions of the in-plane lattice constant. Remarkably, as the in-plane lattice parameters decreased, the paraelectric *cis*-type *Pbmm* phase became much less stable, regardless of the crystallographic orientation, while the stability of the *trans*-type structures only decreased a small amount. This finding implies that the compressive strain along the in-plane direction stabilizes the polar *trans*-type nitrogen arrangement relative to the *cis*-type.

Note that the *cis*-type *Pbmm*-X phase was more stable than the *trans*-type phases, even under compressive strain (Fig. 41). Considering the major distribution of the relaxor-like phase in the $SrTaO_2N$ film (Fig. 37b and 38b), the relaxor-like phase may be attributable to the *Pbmm*-X phase or to a mixture of the *cis*-type phases; I attribute the minor classical ferroelectric phase to the *trans*-type *P4mm* phase. Contrasting the classical ferroelectricity originating from atomic displacement in the *trans*-type phase, the origin of the relaxor-like properties in the *cis* phases is still unclear. However, the lack of long-range atomic order, a common characteristic of relaxor ferroelectric materials [117], may play a role in the relaxor-like behavior. These results will stimulate future work to explain the relationship between the anion arrangement in perovskite oxynitrides and their ferroelectric properties.

5.4 Conclusion

I observed classical ferroelectric behavior in compressively strained $SrTaO_2N$

epitaxial thin films grown on STO substrates by using VPFM. To my knowledge, this study provides the first observation of ferroelectric behavior in perovskite oxynitrides. Classical ferroelectricity coincident with visible light absorption is difficult to achieve with conventional perovskite oxides, making $SrTaO_2N$ useful for ferroelectric photocatalysts [120] and ferroelectric-based photovoltaic cells [121]. I attributed the classical ferroelectricity in regions with 10^1–10^2 nm domains to *trans*-type anion ordering, likely stabilized by compressive epitaxial strain. In contrast, the surrounding matrix region showed relaxor ferroelectric-like behavior, characterized by the absence of spontaneous polarization, positive $d\varepsilon'/dT$, and a ferroelectric–paraelectric phase transition around 600 K. DFT calculations of the phase stability under epitaxial strain suggested that small domains of the *trans*-type classical ferroelectric phase were embedded in a *cis*-type relaxor-like matrix. This study clarified that the concept to develop noble functionality with adjusting anion arrangement is effective.

Chapter 6

Artificial control on anion distribution in $Ca_{1-x}Sr_xTaO_2N$

6.1 Introduction

In the study on the ferroelectricity of the $SrTaO_2N$ epitaxial thin film, I could not achieve structural observation on the effect of epitaxial strain on anion arrangement. This is because the volume fraction of the ferroelectric region, which was assigned to have *trans*-type anion arrangement, was too small to be detected with some structural measurement technique. The small volume fraction is, at least partly, derived from the partial relaxation of the $SrTaO_2N$ epitaxial thin films form the lattice of $SrTiO_3$ (STO) substrates and resulting smaller tetragonal distortion (c/a = ~1.026) than the calculated ferroelectric *trans* structure (c/a = 1.07). On the other hand, $CaTaO_2N$ showed coherent growth on STO substrate due to the small mismatch of −1.1% and tetragonal distortion (c/a = 1.022) similar to the $SrTaO_2N$ epitaxial thin film. Thus, one possible way to apply higher epitaxial strain to perovskite oxynitride is to mix *A*-site cations of $SrTaO_2N$ and $CaTaO_2N$. It is expected that higher tetragonal distortion is achieved at the composition with higher x in $Ca_{1-x}Sr_xTaO_2N$ where the film can be grown coherently on the substrate. The higher tetragonal distortion might raise the volume fraction of the *trans*-type region

to the level detectable by structural observations.

In this chapter, I present epitaxial thin film growth of perovskite oxynitride with different tetragonal distortion and demonstrate structural observation on anion distribution in them with the techniques of polarized X-ray absorption (XAS) and electron energy loss spectroscopy (EELS) analysis combined with scanning transmission electron microscope (STEM). Tetragonal distortion of the epitaxial thin films was systematically controlled by changing composition parameter x in $Ca_{1-x}Sr_xTaO_2N$. In addition, I used two kinds of single crystals, Nb(0.5 wt%)-doped STO (NSTO; a = 3.905 Å) and $DyScO_3$ (DSO; a = 3.94 Å in a pseudo-tetragonal approximation) to change the extent of tetragonal distortion in oxynitride films with the same composition.

6.2 Method

A series of $Ca_{1-x}Sr_xTaO_2N$ (x = 0, 0.1…0.7) epitaxial thin films were prepared on the (100) plane of NSTO (Shinkosha Co., Ltd.) and the (110) plane of DSO substrate (CrysTec GmbH) with atomically flat surfaces by the technique of nitrogen plasma assisted pulsed laser deposition (NPA-PLD). $Ca_{2-2x}Sr_{2x}Ta_2O_7$ ceramic pellets were used as target to grow films with corresponding cation compositions. The pellets were prepared by sintering mixture of $Sr_2Ta_2O_7$ and $Ca_2Ta_2O_7$ powders with the corresponding cation ratio at 1400 °C for 10 h followed by further sintering at 1500 °C for 10h. The procedure to synthesize the powders of $Sr_2Ta_2O_7$ and $Ca_2Ta_2O_7$ are described in Chapter 4. The substrate temperature and partial pressure of N_2 gas were

set at 600−650 °C and 1.0×10^{-5} Torr, respectively. N_2 gas was activated into plasma by an electron cyclotron resonator with operation current of 30 mA. A KrF excimer laser (λ = 248 nm) operated at 10 Hz was used for ablation. Energy density of laser pulses was adjusted to control the deposition rates less than 10 nm/h. Thicknesses of the films were within the range of 15–26 nm.

Compositions of the films were confirmed with X-ray photoemission spectroscopy using the $SrTaO_2N$ and $CaTaO_2N$ epitaxial thin films obtained in Chapter 4 as references. Crystal structures of the thin films were evaluated by X-ray diffraction (XRD) using a four-axis diffractometer (Bruker AXS, d8 discover). In the XRD measurement, reciprocal space mapping (RSM) was conducted with a 1D detector while out-of-plane lattice constants were calculated from the peak positions of (00*h*) diffractions detected with a 0D detector. XAS were taken on O K-edge and N K-edge regions using vertically and horizontally polarized X-ray beams with an incident angle of 75° to the sample surfaces. The XAS measurements were carried out on beamline BL-27SU of Spring-8. The signals were collected in total electron yield (TEY) and total fluorescence yield (TFY) modes. In bulk sensitive TFY mode, only N K-edge spectra will be shown because O K-edge spectra severely overlap with signals from substrates. The following 7 representative samples were evaluated in the XAS measurements: $CaTaO_2N$, $Ca_{0.8}Sr_{0.2}TaO_2N$, $Ca_{0.7}Sr_{0.3}TaO_2N$, $Ca_{0.5}Sr_{0.5}TaO_2N$ and $SrTaO_2N$ films on NSTO substrate and $CaTaO_2N$ and $Ca_{0.5}Sr_{0.5}TaO_2N$ films on DSO substrate. Only TFY mode detection was performed in the measurements on the films grown on DSO substrates because the highly insulating substrate prevented collection of data in TEY mode. The spectra were normalized with the following procedure: 1) Raw spectra were divided by mirror current. 2) Linear baselines were extracted by fitting the regions just

lower than peaks and subtracted. 3) Spectra were normalized by net peak areas of the region 395–412, 395–405 and 528–546 eV for spectra of N K-edge in TEY mode, N K-edge in TFY mode and O K-edge in TEY mode, respectively. X-ray linear dichroism (XLD) was calculated using the ratio between in-plane (IP) and out-of-plane (OOP) direction components as 100%:0% in vertically polarized X-ray and 21%:79% in horizontally polarized one. XLD fraction was defined as the ratio of XLD signal to sum of IP and OOP components of absorption. Microscopic lattice structures were investigated by cross-sectional STEM (Jeol, JEM-ARM200F, 200 kV) in high angle annular dark field (HAADF) mode. In the HAADF-STEM measurement, elemental analysis was conducted with EELS (Gatan, GIF Quantum ER Model965) in a site selective manner. EELS spectra were normalized with the following procedure: 1) Baselines were extracted by fitting the whole energy region with the function $f(x) = \exp(ax + b)$, where a and b are fitting parameters, and subtracted from the spectra. 2) Spectra were normalized with the average of intensity in the region between N-K edge and O-K edge peaks (425–525 eV).

6.3 Result and discussion

Figure 42 shows RSM images of the $Ca_{1-x}Sr_xTaO_2N$ films. The films within a composition range of $0 \leq x \leq 0.5$ grew coherently on NSTO substrates while DSO allowed coherent growth with a wider range of $0 \leq x \leq 0.7$ due to the larger lattice constant of DSO than NSTO. The films showed sign of lattice relaxation at higher x in both cases. All the coherently grown films showed clear fringe patterns around (001)

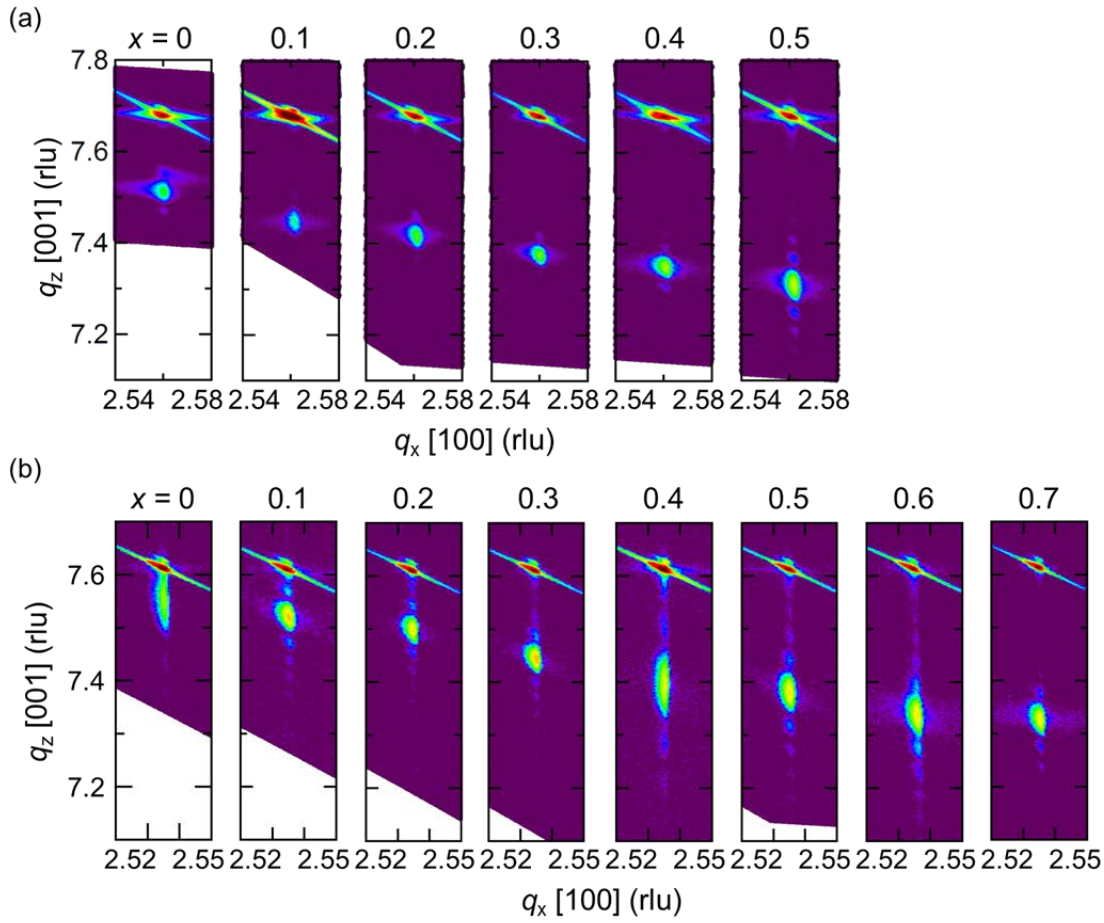

Figure 42. XRD RSMs around 103 diffraction of $Ca_{1-x}Sr_xTaO_2N$ epitaxial thin films grown on (a) NSTO ($0 \leq x \leq 0.5$) and (b) DSO ($0 \leq x \leq 0.7$).

peaks in 2θ-θ pattern, indicating flat surfaces and sharp film/substrate interfaces (Fig. 43). *c*-axis lattice constant raised monotonically with increasing Sr amount *x* on both substrates (Fig. 44). The almost linear relationships indicate the change in lattice constant can be described with Vegard's law very well. The highest tetragonal distortion (c/a = 1.05) was achieved at the composition of $Ca_{0.5}Sr_{0.5}TaO_2N$ on NSTO substrate. The value was much larger than that of the $SrTaO_2N$ epitaxial thin film grown on NSTO substrate (c/a = ~1.026) as expected.

Figure 45 and 46 show polarized XAS spectra of the films grown on NSTO

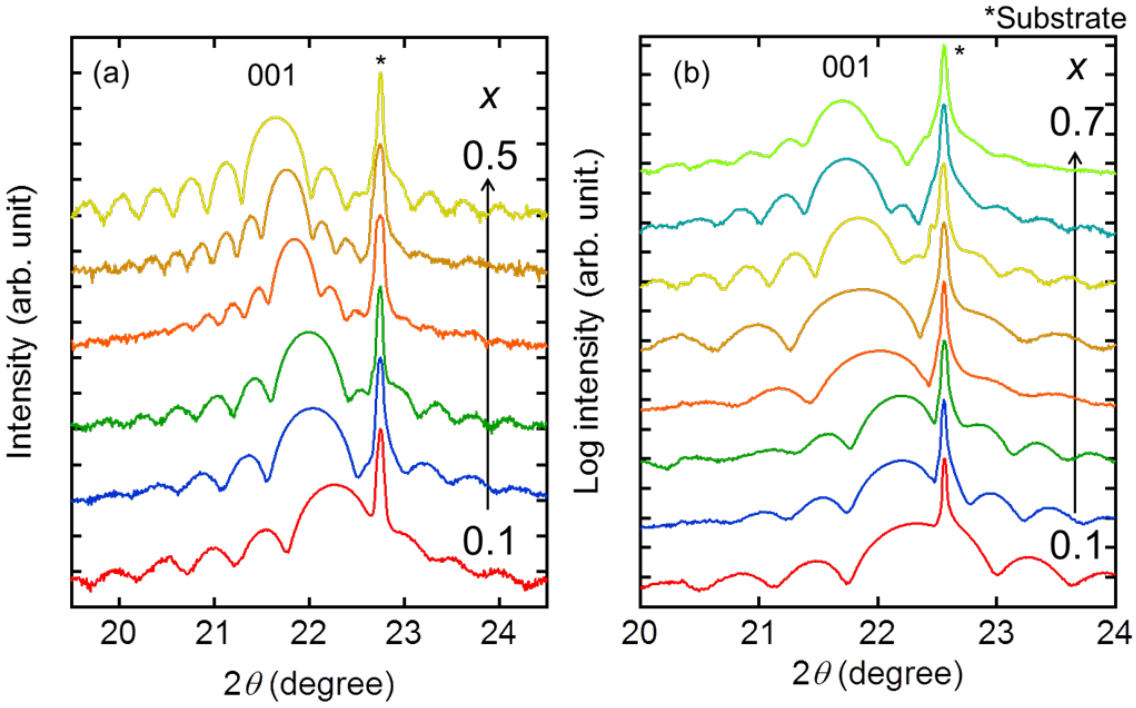

Figure 43. XRD 2θ-θ patterns around 001 diffraction of $Ca_{1-x}Sr_xTaO_2N$ epitaxial thin films grown on (a) NSTO ($0 \le x \le 0.5$) and (b) DSO ($0 \le x \le 0.7$).

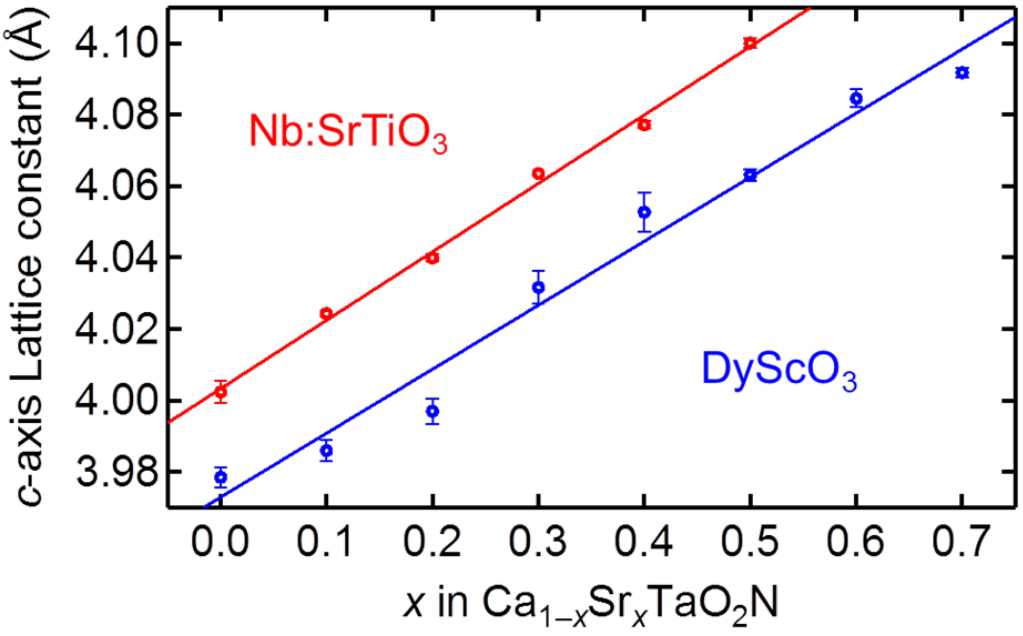

Figure 44. *c*-axis lattice constants of $Ca_{1-x}Sr_xTaO_2N$ epitaxial thin films grown on NSTO ($0 \le x \le 0.5$) and DSO ($0 \le x \le 0.8$) as functions of Sr content *x*.

substrate taken in TEY mode. The polarization dependence was not clear in both N and O K-edge spectra of the $SrTaO_2N$ epitaxial thin film (Fig. 45e and 46e), which indicates the similar occupancy of the two anion sites by nitrogen and oxygen. This result is consistent with the model suggested by the piezoresponse force microscopy in Chapter 5 that the matrix part of the $SrTaO_2N$ epitaxial thin films is composed of *cis*-type structure without long range anion ordering. The situation is similar in the N-Kedge spectra of the $CaTaO_2N$ epitaxial thin film, which possessed a similar *c*/*a* value, i.e. tetragonal distortion, as the $SrTaO_2N$ epitaxial thin film (Fig. 45a). Meanwhile, weak XLD was observed in O K-edge spectra on the $CaTaO_2N$ (Fig. 46a), which suggests slight difference in site occupancy of oxygen. The difference between $SrTaO_2N$ and $CaTaO_2N$ may be related to the homogeneity of epitaxial strain in the films: $CaTO_2N$ is totally strained by the substrate while $SrTaO_2N$ has gradient in strain along the growth direction due to the partial relaxation from the lattice of the substrate.

XLD of both N and O K-edge spectra was much clearer in the highly distorted mixed crystals than pure phases. Figure 47 shows XLD fraction of each spectrum for rough comparison of XLD intensity. Larger XLD fraction in the mixed crystals than in the pure ones is confirmed in the N K-edge spectra. Furthermore O K-edge spectra exhibit the tendency that XLD becomes larger with increasing Sr ratio and was the highest in the $Ca_{0.5}Sr_{0.5}TaO_2N$ epitaxial thin film with the highest distortion. $Ca_{0.5}Sr_{0.5}TaO_2N$ shows slightly smaller intensity than $Ca_{0.8}Sr_{0.2}TaO_2N$ and $Ca_{0.7}Sr_{0.3}TaO_2N$ in N k-edge XLD. This may be attributable to the influence of some surface states including adsorbed molecules because the $Ca_{0.5}Sr_{0.5}TaO_2N$ film showed the clearest XLD in the spectra taken in bulk-sensitive TFY mode (Fig. 48).

Figure 49 shows N K-edge spectra of $CaTaO_2N$ and $Ca_{0.5}Sr_{0.5}TaO_2N$ grown on

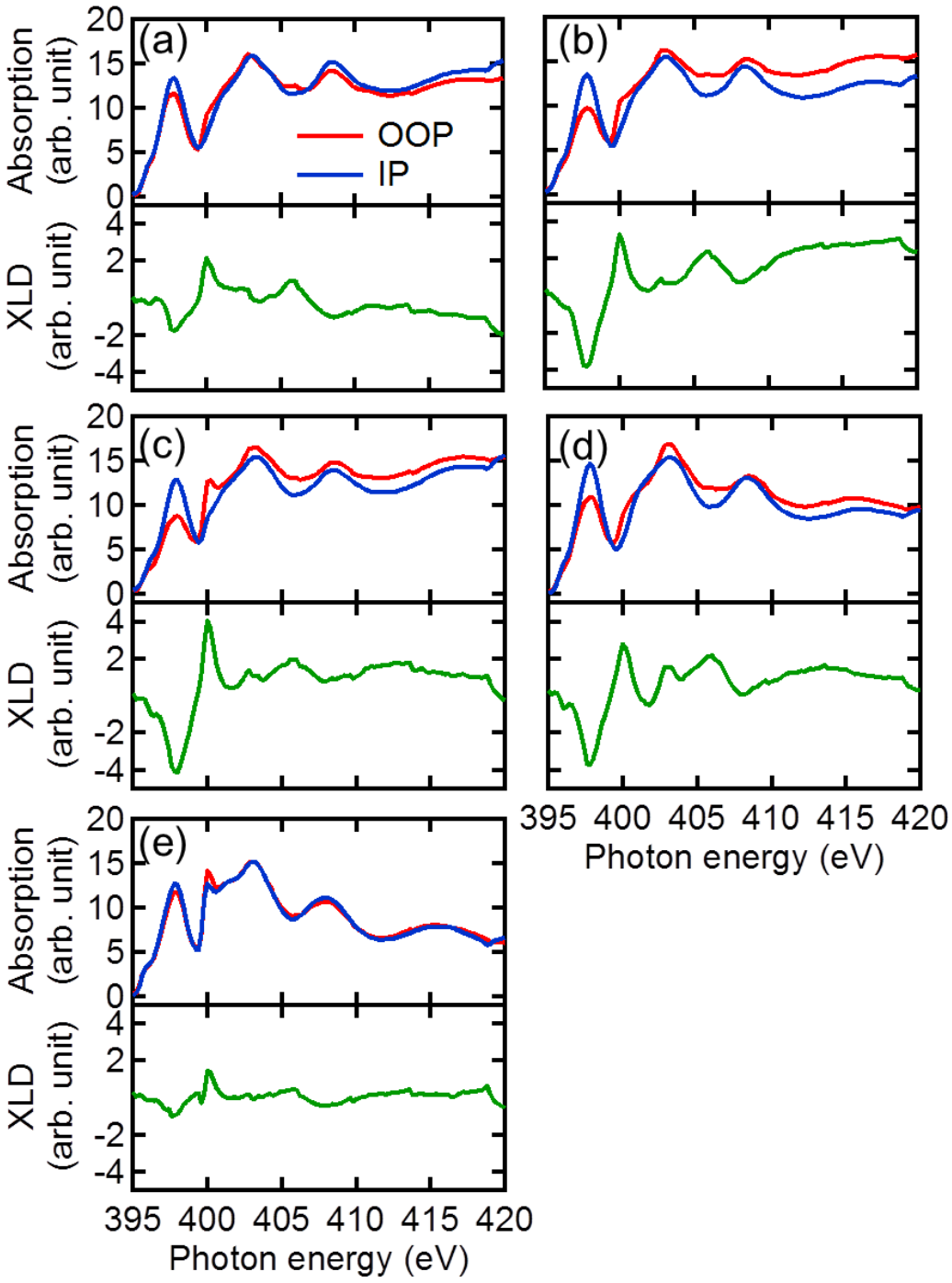

Figure 45. XAS N-K edge spectra of $Ca_{1-x}Sr_xTaO_2N$ [x = 0, 0.2, 0.3, 0.5, 1 for (a)–(e), respectively] epitaxial thin films grown on NSTO substrate observed in TEY mode. Red and blue lines show absorption of X-ray polarized in out-of-plane and in-plane directions, respectively, and green lines show difference between the red and blue lines.

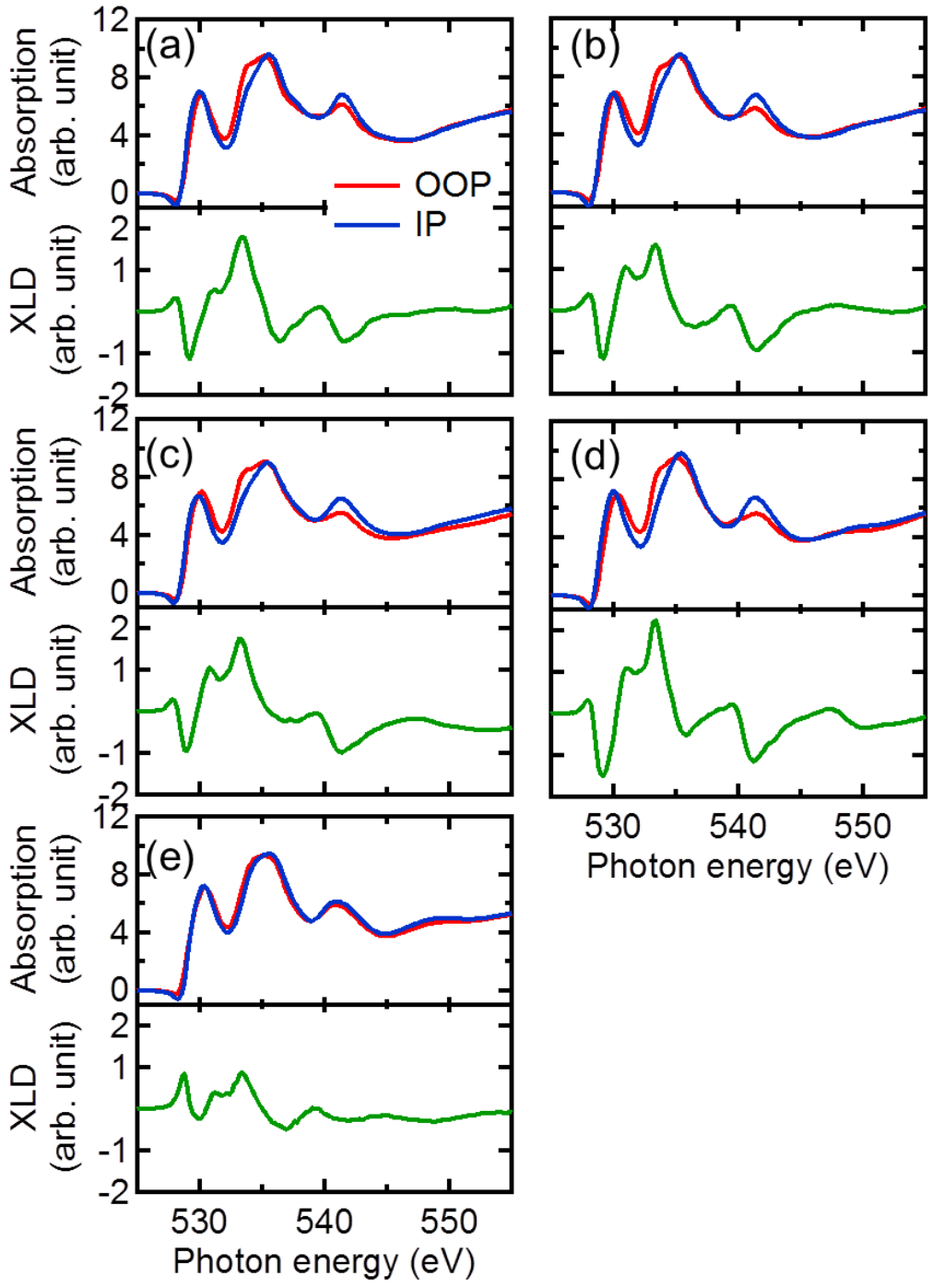

Figure 46. XAS O-K edge spectra of $Ca_{1-x}Sr_xTaO_2N$ [x = 0, 0.2, 0.3, 0.5, 1 for (a)–(e), respectively] epitaxial thin films grown on NSTO substrate observed in TEY mode. Red and blue lines show absorption of X-ray polarized in out-of-plane and in-plane directions, respectively, and green lines show difference between the red and blue lines.

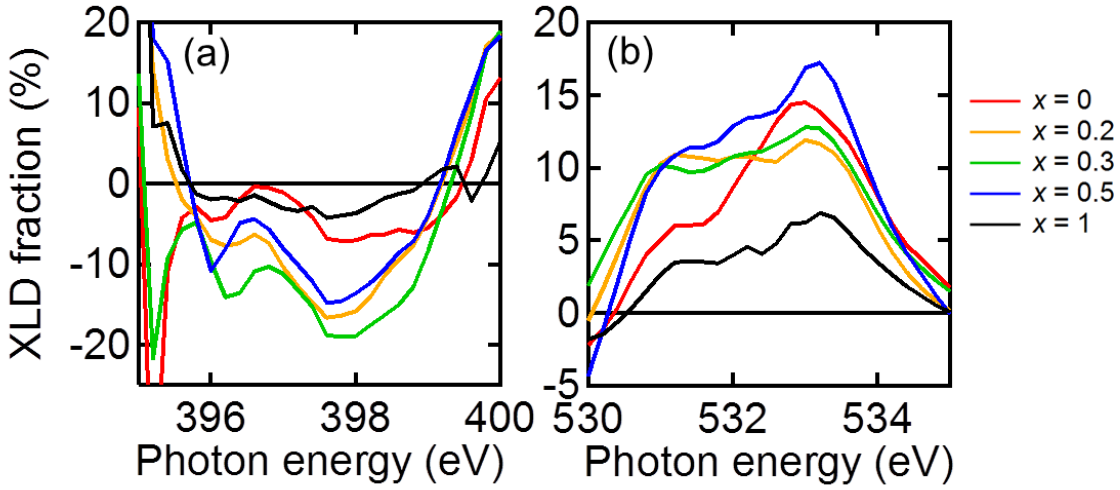

Figure 47. (a) N K-edge and (b) O K-edge XLD fractions calculated from the XAS spectra in Fig. 45 and 46.

DSO substrate take in TFY mode. While $CaTaO_2N$ showed almost no XLD, the $Ca_{0.5}Sr_{0.5}TaO_2N$ film exhibited a small but finite XLD signal. Though the similar tendency is seen in the films grown on NSTO, the XLD intensity of the $Ca_{0.5}Sr_{0.5}TaO_2N$ film grown on DSO (c/a = 1.03) was obviously weaker than that grown on NSTO (c/a = 1.05). This indicates that the difference in XLD intensity in the series of samples is not attributable to composition but to tetragonal distortion.

Because the XAS measurements clearly indicated different configuration between axial and equatorial sites, HAADF-STEM EELS measurement was performed on the $Ca_{0.5}Sr_{0.5}TaO_2N$ epitaxial thin film grown on NSTO substrate, which showed the highest tetragonal distortion. In the HAADF-STEM image, a clear single crystalline lattice image was observed (Fig. 50a). The selected area shown in Figure 50b was divided into 61 × 14 cells and an EELS spectrum was taken at each cell. From the image I picked up points corresponding to the axial and equatorial anion sites and averaged the EELS spectra, respectively (Fig. 50c). It can be seen that the spectrum of

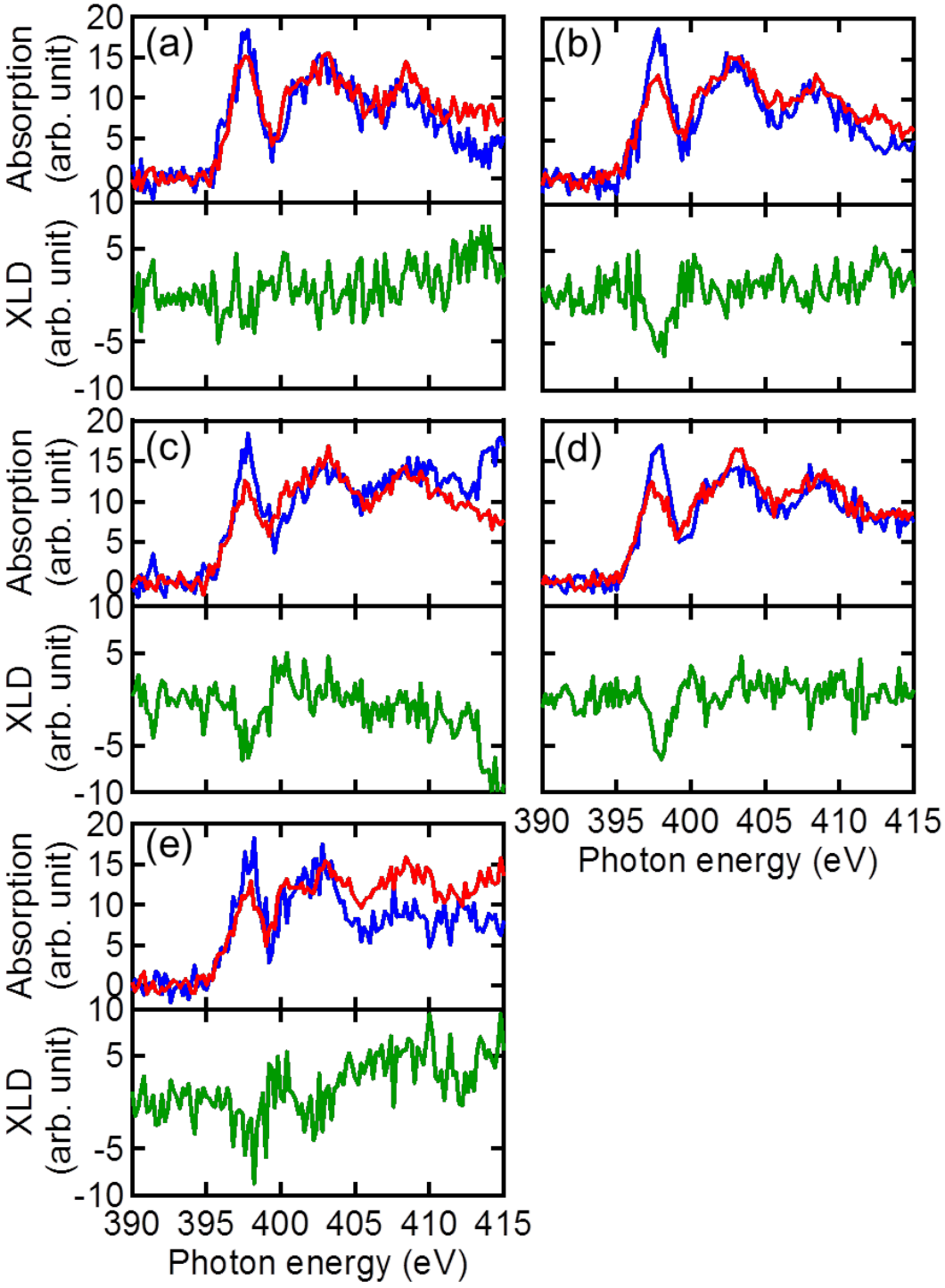

Figure 48. XAS N-K edge spectra of $Ca_{1-x}Sr_xTaO_2N$ [x = 0, 0.2, 0.3, 0.5, 1 for (a)–(e), respectively] epitaxial thin films grown on NSTO substrate observed in TFY mode. Red and blue lines show absorption of X-ray polarized in out-of-plane and in-plane directions, respectively, and green lines show difference between the red and blue lines.

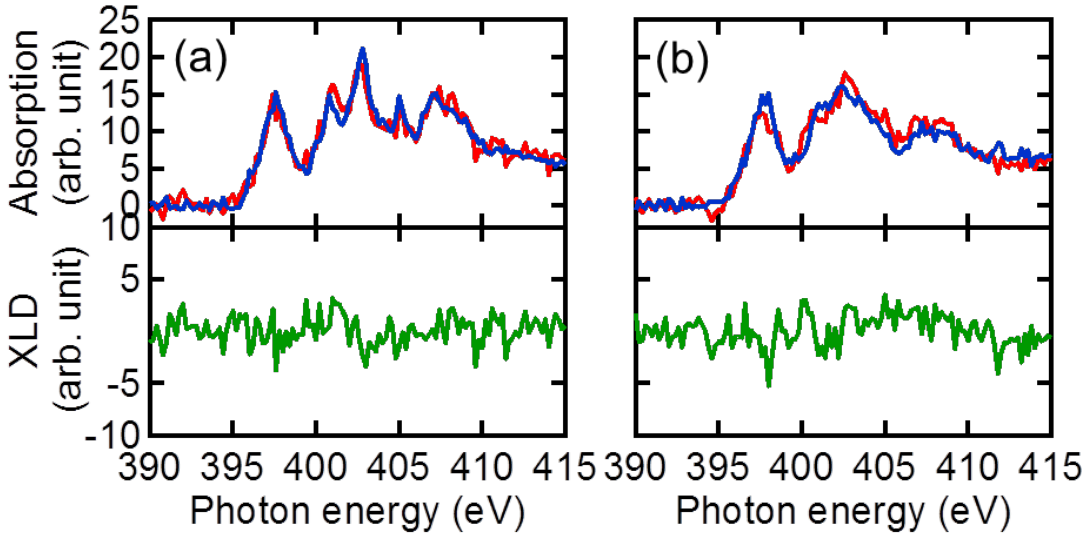

Figure 49. XAS N-K edge spectra of (a) $CaTaO_2N$ and (b) $Ca_{0.5}Sr_{0.5}TaO_2N$ epitaxial thin films grown on DSO substrate observed in TFY mode. Red and blue lines show absorption of X-ray polarized in out-of-plane and in-plane directions, respectively, and green lines show difference between the red and blue lines.

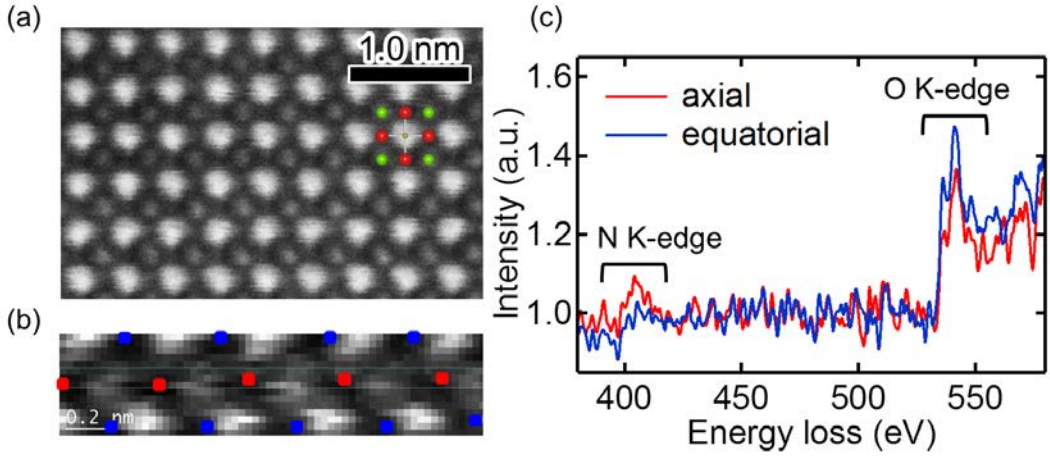

Figure 50. (a) HAADF-STEM image of the $Ca_{0.5}Sr_{0.5}TaO_2N$ epitaxial thin film grown on NSTO, (b) HAADF-STEM image simultaneously measured with EELS and (c) averaged EELS spectra observed at axial (red) points and equatorial (blue) ones in (b), respectively.

axial site showed higher intensity at N K-edge peak, while that of equatorial site possessed a stronger O K-edge peak. The result clearly indicates that more nitrogen ions are allocated at the axial site in the highly distorted thin film, which is consistent with the suggestion by the first principles calculation on $SrTaO_2N$ that larger tetragonal distortion stabilizes *trans*-type structure in a relative sense.

6.4 Conclusion

Effect of tetragonal distortion induced by epitaxial stress on anion arrangement was investigated in the series of $Ca_{1-x}Sr_xTaO_2N$ epitaxial thin films. The films were grown in a coherent manner on NSTO and DSO substrates within the composition range of $0 \leq x \leq 0.5$ and $0 \leq x \leq 0.7$, respectively. With increasing x, tetragonal distortion c/a was enhanced due to the larger lattice mismatch and reached up to 1.05 in the $Ca_{0.5}Sr_{0.5}TaO_2N$ epitaxial thin film grown on NSTO. The highly distorted film showed clear XLD signal in polarized XAS measurement, which indicates different site occupancy between axial and equatorial sites. EELS analysis combined with HAADF-STEM observation clarified higher and lower occupation on axial and equatorial sites by nitrogen, respectively. These results proved the effectiveness in artificial control of anion arrangement with epitaxial stress which would provide us a chance to develop noble functionalities in anion mixed compounds such as oxynitrides.

Chapter 7

Filling control on the conduction band of $SrNbO_{3-x}N_x$

7.1 Introduction

Valence state of transition metal oxides is one of the predominant factors that govern their electrical properties because it determines the number of electrons in the conduction band. In case of perovskite oxides, there are too many reports on filling control of conduction band composed of *d*-orbital of *B*-site cations and resultant electrical properties by partial substitution of *A*-site cations. On the other hand, the influence of partial substitution for oxygen site has rarely been studied. Differently from substitution of *A*-site cations, anion site substitution directly perturbs the conduction path, usually the network of *B*-site cations and oxygen anions, which may have unexpected influence on physical properties.

In this chapter, I present control of valence state of *B*-site cation with partial substitution of oxygen by nitrogen. In contrast to d^0 stable Ta ion, Nb, belonging to the same element group as Ta, has flexibility in valence state that allows it d^0 to d^1 states. Thus I chose $SrNbO_{3-x}N_x$ as a model system to conduct the filling control here.

7.2 Method

A series of $SrNbO_{3-x}N_x$ epitaxial thin films with different nitrogen content x were prepared on the (100) plane of $KTaO_3$ substrate (a = 3.989 Å) (MTI corporation) by nitrogen plasma assisted pulsed laser deposition (NPA-PLD) method. A ceramic pellet of $Sr_2Nb_2O_7$ was used as a target, which was obtained by sintering $Sr_2Nb_2O_7$ powder at 1400 °C for 24 h. The $Sr_2Nb_2O_7$ powder was synthesized by conventional solid phase reaction of a stoichiometric mixture of Nb_2O_5 and $SrCO_3$ in an alumina crucible: The mixture was first reacted at 900 °C for 12 h and successively heated at 1200 °C for 12 h. Substrate temperature and partial pressure of nitrogen gas was fixed to 630 °C and 1.0×10^{-5} Torr, respectively, during the deposition of the films. Nitrogen was activated into plasma with an electron cyclotron resonator (ECR) and the nitrogen content x in the films was controlled by changing the operation current of ECR from 0 to 40 mA. A KrF excimer laser (λ = 248 nm) to ablate the target was operated at an energy fluence of 0.37–0.44 J cm^{-2} $shot^{-1}$, and a repetition rate of 10 Hz. Deposition rate was typically set within 4−7 nm/h and resulting thickness of the films were from 25 to 45 nm.

Nitrogen content x in the films was evaluated by nuclear reaction analysis (NRA) using the $^{15}N(p,\alpha\gamma)^{12}C$ reaction. Energy of incident proton beam was set at 898 keV resonance of the reaction and the emitted γ-ray was detected with two 3-in. $Bi_4Ge_3O_{12}$ scintillation counters. Using a TiN epitaxial film as a reference, x was calculated under the reasonable assumption that ^{15}N occupies natural isotope ratio (0.03%) of all the nitrogen atoms. The NRA measurements were carried out with a 1 MV tandetron accelerator at Tandem Accelerator Complex, University of Tsukuba.

Crystal structures of the thin films were evaluated by X-ray diffraction (XRD) using a four-axis diffractometer (Bruker AXS, d8 discover). Resistivity of the films was examined by conventional 4-probes method and Hall effect measurements were used to determine carrier density and mobility. Before the transport property measurements, silver thin film of 100 nm was deposited on top of each terminal as an electrode by sputtering. Sample circumstances such as temperature and magnetic field during the measurements were controlled with Physical Property Measurement System (PPMS, Quantum Design). Optical absorption coefficient of the films were calculated from transmission and reflection measured with a UV-visible-NIR spectrometer.

7.3 Result and discussion

Nitrogen content x in the $SrNbO_{3-x}N_x$ thin films increased monotonically with increasing operation current of ECR as shown in Figure 51. x took values within $0 \leq x \leq 1.02$ (7), which is consistent with the possible range of Nb valence from 4+ ($SrNbO_3$) to 5+ ($SrNbO_2N$). Epitaxial growth of phase pure thin films with perovskite structure was confirmed by XRD 2θ-θ measurements (Fig. 52). Figure 53 shows lattice parameters a and c as functions of nitrogen content x. $SrNbO_3$, an end member of the system, grew coherently on the KTO substrate. By introducing nitrogen, lattice constant increased monotonically and lattice relaxation was induced even with a small amount of $x = 0.07$. However, the change in lattice parameters by increasing x was within 0.05 Å both in a and c axes and much smaller than that observed in the $SrTaO_{3-x}N_x$ system in Chapter 4. The small change in lattice parameter is plausibly attributable to the cancelation of the

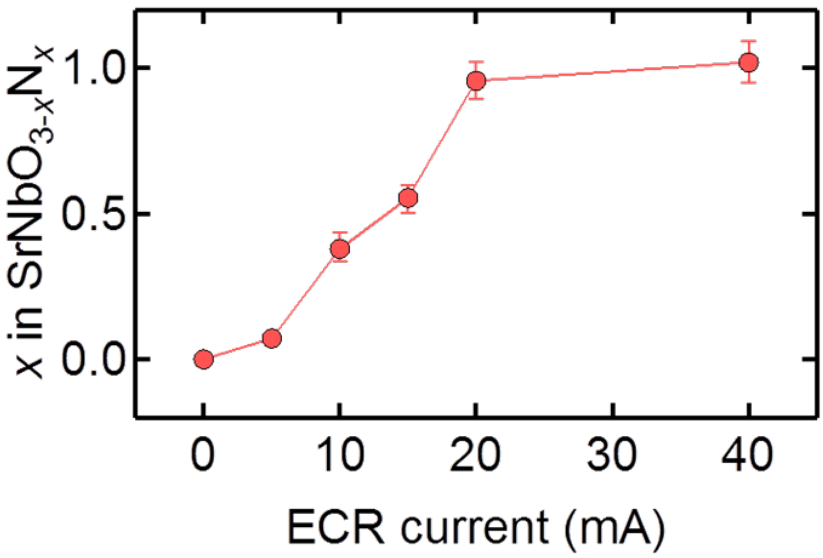

Figure 51. Nitrogen content *x* in the $SrNbO_{3-x}N_x$ thin films grown in nitrogen plasma created with different ECR currents.

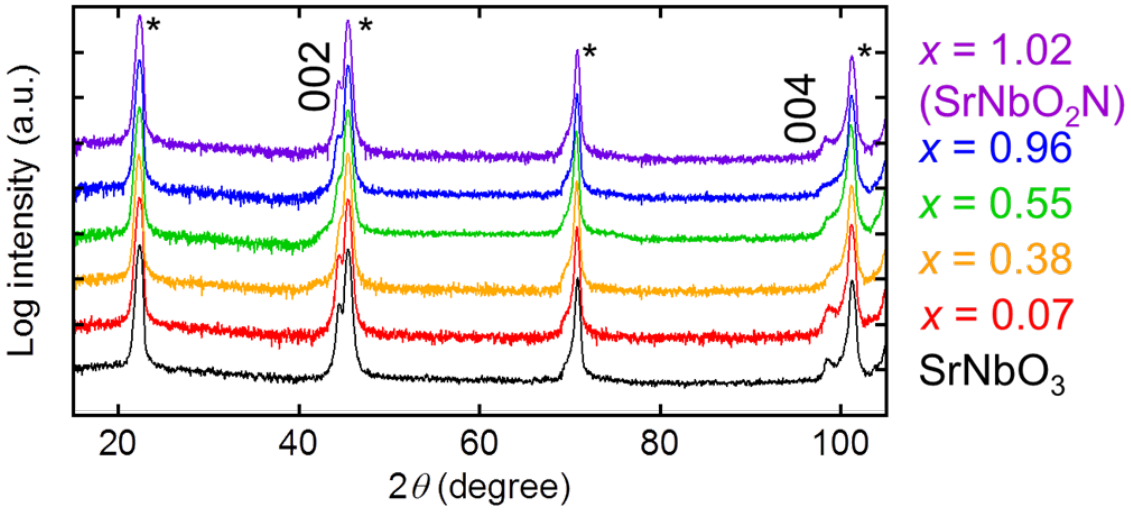

Figure 52. XRD 2*θ*-*θ* patterns of the $SrNbO_{3-x}N_x$ thin films on KTO substrate measured in out-of-plane direction.

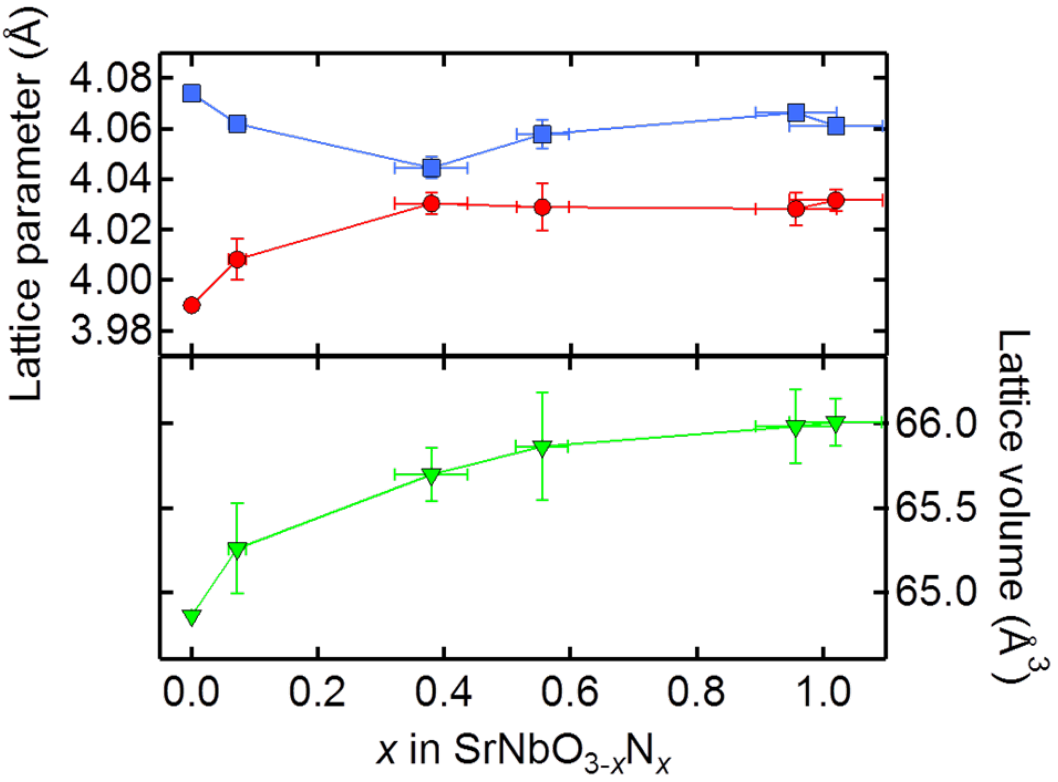

Figure 53. (a) *a*- and *c*-axis lattice parameters of the $SrNbO_{3-x}N_x$ thin films and (b) lattice volume calculated from *a* and *c* as functions of nitrogen content *x*.

effect of nitrogen introduction by decrease of Nb ionic radius accompanying the valence change from Nb^{4+} (0.68 Å) to Nb^{5+} (0.64 Å). These analyses on composition and crystal structure indicate successful growth of the series of $SrNbO_{3-x}N_x$ epitaxial thin films. I hereafter describe the film with nitrogen content x = 1.02(7) as $SrNbO_2N$ film, which has essentially d^0 state within the experimental error.

Figure 54 shows resistivity ρ, carrier density n and mobility μ as functions of x measured at room temperature. The resistivity ρ of the films monotonically increased with increasing x. This is not surprising because Nb should be subjected to the change in valence state from d^1 to d^0. Actually, n decreased following the value calculated from x under the assumption of rigid band model (dashed line in Fig. 54b). However, the

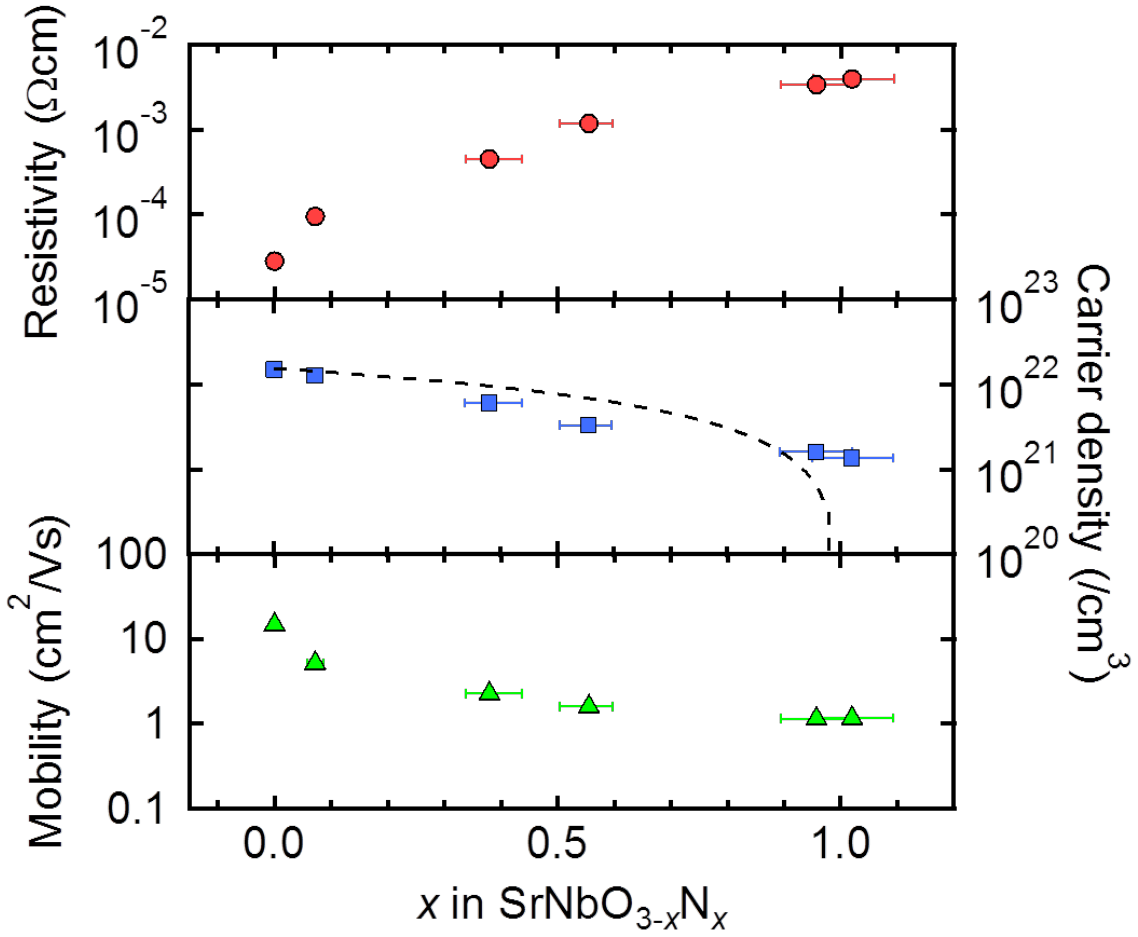

Figure 54. (a) resistivity, (b) carrier density and (c) mobility of the $SrNbO_{3-x}N_x$ thin films grown on KTO substrate as functions of nitrogen content *x*.

$SrNbO_2N$ epitaxial thin film showed a significant amount of residual carriers (> 1 × 10^{-21} cm^{-3}). One possible origin of the residual carriers is oxygen vacancies generated under the reductive growth condition. Such oxygen vacancies would form shallow impurity level. The increase in ρ caused by nitrogen introduction is attributable not only to the decrease in carrier density but also to that in mobility. The reduction of μ suggests that the carrier path, i.e., cubic network composed of niobium and oxygen, was structurally perturbed by nitrogen substitution for the oxygen site.

Figure 55 shows temperature dependence of the resistivity of the $SrNbO_{3-x}N_x$ epitaxial thin films. The $SrNbO_3$ film with the lowest resistivity of the order of

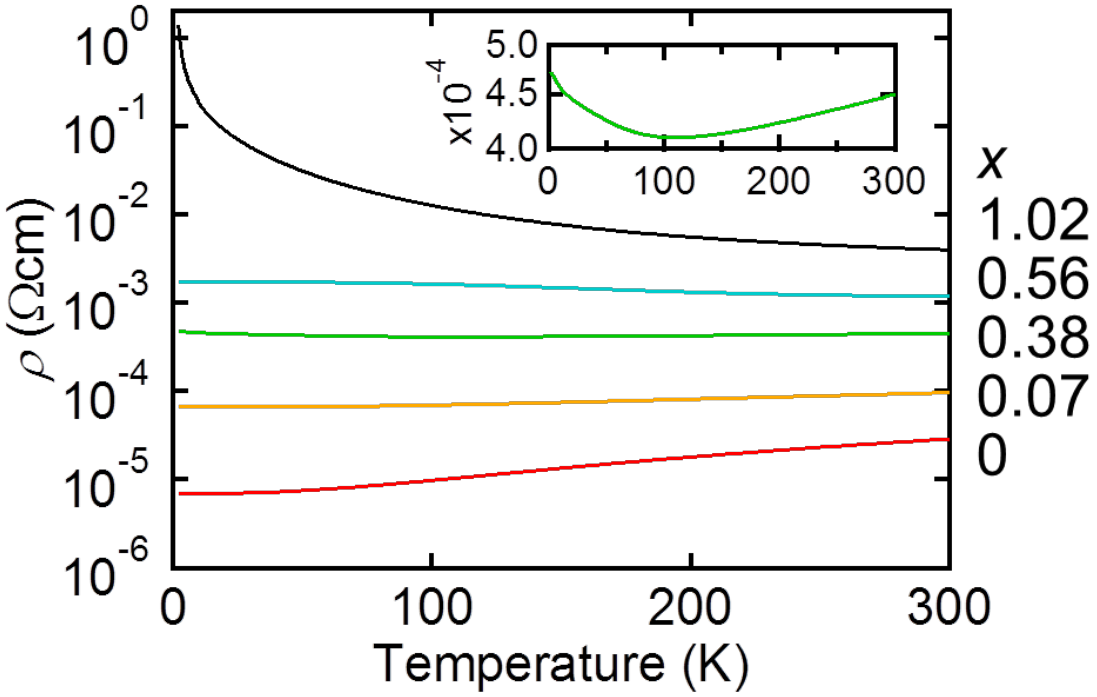

Figure 55. Temperature dependence of the $SrNbO_{3-x}N_x$ thin films on KTO substrate. Inset shows magnified view of the data for x = 0.38.

10^{-6}–10^{-5} Ωcm showed metallic temperature dependence ($d\rho/dT > 0$). Following the increase in resistivity by nitrogen introduction, the temperature dependence gradually turned from metallic to semiconducting ($d\rho/dT < 0$). The composition x = 0.38 is critical and at the composition the ρ-T curve showed temperature-induced metal-insulator transition around 100 K (inset of Fig. 55). The end member, $SrNbO_2N$ thin film showed insulating behavior, in which the conductivity can be extrapolated to 0 S/cm at 0 K (Fig. 56). The low temperature conductivity of the $SrNbO_2N$ can be fitted well with the following ES variable range hopping (VRH) law, which includes the effect of the Coulomb interaction among electron carriers [122].

$$\sigma(T) = \sigma_{ES} \exp\left[-(T_{ES}/T)^{\frac{1}{2}}\right] \tag{7.1}$$

In the range higher than 5 K, higher-order inelastic hopping conduction, which can be described by the following power law, superimposed on the Mott VRH conduction [123].

$$\sigma(T) = \sum C_N T^{\gamma} \tag{7.2}$$

where C_N is a prefactor, N is the number of localized states and $\gamma = N - N/(N+1)$. In the fitting of the conductivity of $SrNbO_2N$, I used the following equation combining these two mechanisms of electrical conduction.

$$\sigma(T) = \sigma_{ES} \exp\left[-(T_{ES}/T)^{\frac{1}{2}}\right] + C_1(T-5)^{1.33} + C_2(T-5)^{2.5} \tag{7.3}$$

Fitting of the equation to the experimental data (Fig. 56) indicates that the insulating behavior is a consequence of localization of wave function induced by nitrogen. This

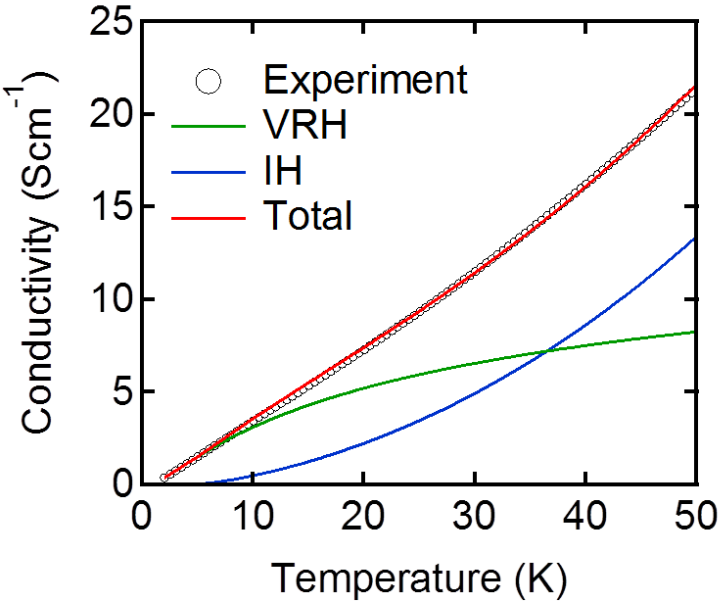

Figure 56. Temperature dependence of conductivity of $SrNbO_2N$ epitaxial thin film. Experimental data is shown with white circles. Red curve is the fitting result obtained by equation (7.3). Green and blue curves indicate the Mott VRH and inelastic hopping components of the red curve.

suggests that conduction electrons are scattered by randomly dispersed nitrogen atoms in the crystal. However, the scattering mechanism should not be simple and can include the following structural and chemical effects: 1) Nitrogen insertion bends chemical bonds. 2) Nitrogen ions would attract electrons owing to the high covalency. 3) a N^{3-} ion makes the high-valent state (i.e. 5+) of neighboring Nb ions.

As for optical absorption, the influence of nitrogen introduction was observed in both NIR ($h\nu$ < 1.7 eV) and visible ($h\nu$ > 1.7 eV) light regions (Fig. 57). In the former region, $SrNbO_3$ showed large absorption increasing toward lower energy. This is free electron absorption characteristic of metallic materials. Actually, the absorption in NIR region was suppressed by increasing nitrogen amount *x*, which reduces the number of free electron as shown in the above-mentioned electrical measurement. On the other hand, the absorption in the visible light region reflects the cha nge in band structure. $SrNbO_3$ has been reported to have optical absorption with an edge at 1.9 eV derived

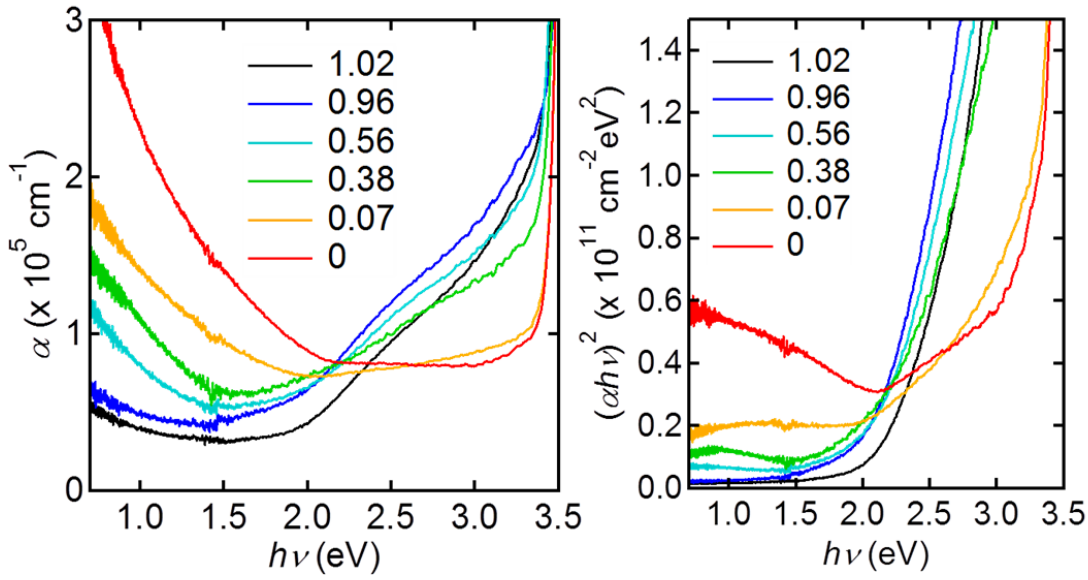

Figure 57. (a) Absorption coefficient spectra and (b) $(\alpha h\nu)^2$ vs $h\nu$ plot of the $SrNbO_{3-x}N_x$ thin films on KTO substrate.

from electron transition within the split conduction band mainly composed of 4*d* orbital of Nb [124]. The present $SrNbO_3$ epitaxial thin also showed visible light absorption at almost the same region though the absorption edge position is unclear due to the overlapping of the free electron absorption. On the other hand, it is known that $SrNbO_2N$ also shows visible light absorption with an absorption edge at 1.9 eV [11]. Though the edge position is accidentally almost the same as that of the $SrNbO_3$, the origins are totally different: the electronic transition from the valence to conduction bands gives the edge in the case of some other d^0 perovskite oxynitrides. The bandgap of $SrNbO_2N$ was determined to be 2.0 eV from the Tauc plot of the present epitaxial thin film under the assumption of direct bandgap semiconductor (Fig. 57b). The value is almost the same as the reports on the bulk specimens but slightly higher. This may be attributable to inaccuracy in determining band edge from the spectra of bulk specimens; they shows relatively large absorption under the absorption edge, which is plausibly derived from structural and/or chemical defects.

It should be noted that the $SrNbO_2N$ film showed much higher absorption efficiency than the $SrNbO_3$ film though their absorption edges are very close to each

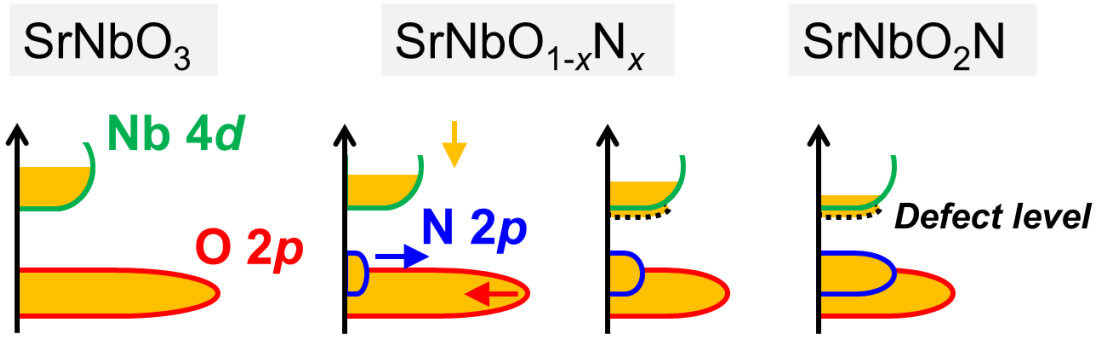

Figure 58. Band structure of $SrNbO_{3-x}N_x$ system estimated from electrical and optical measurements.

other. The $SrNbO_{3-x}N_x$ thin films with intermediate composition between $SrNbO_3$ and $SrNbO_2N$ showed relatively sharp change in the visible light region rather than in the NIR light region. While the film with x = 0.07 showed similar visible light absorption to $SrNbO_3$, the film with x = 0.38 possessed quite close structure to $SrNbO_2N$.

The above-mentioned features observed in both electrical and absorption measurements suggest that the band structure of the $SrNbO_{3-x}N_x$ system can be described by rigid band model as illustrated in Figure 58. This can be a useful feature for applications including photoanode because $SrNbO_{3-x}N_x$ with an intermediate

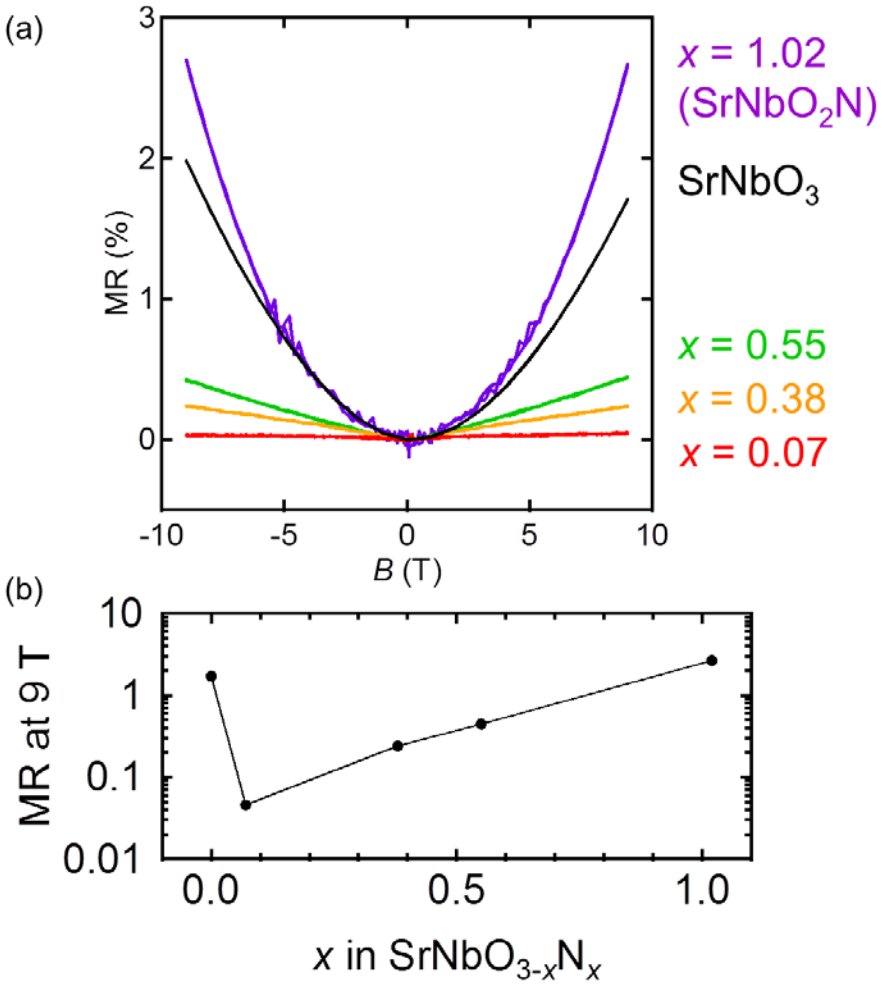

Figure 59. (a) Magnetic field dependence of MR of the $SrNbO_{3-x}N_x$ films measured at 10 K and (b) MR value at 9 T as a function of nitrogen content x.

composition with $0 < x < 1$ possesses higher absorption coefficient than $SrNbO_3$ and higher mobility than $SrNbO_2N$ at the same time.

In addition to the systematic changes in the band structure and the related properties with nitrogen insertion, I here observed a unique electrical property, high magnetoresistance (MR) at low temperature. Unless noted otherwise, MR effects mentioned later will represent those taken under the configuration that applied magnetic field is vertical to current flow (transverse MR). Figures 59a and b show MR curves of the $SrNbO_{3-x}N_x$ epitaxial thin films measured at 10 K and MR values measured at magnetic field B of 9 T plotted against nitrogen amount x, respectively. Notably, the MR value in $SrNbO_{3-x}N_x$ monotonically increases with increasing x with an exception of x = 0. The MR increased with decreasing temperature and the highest MR value, 50%, was recorded at x = 1.02, B = 9 T and T = 2 K (Fig. 60).

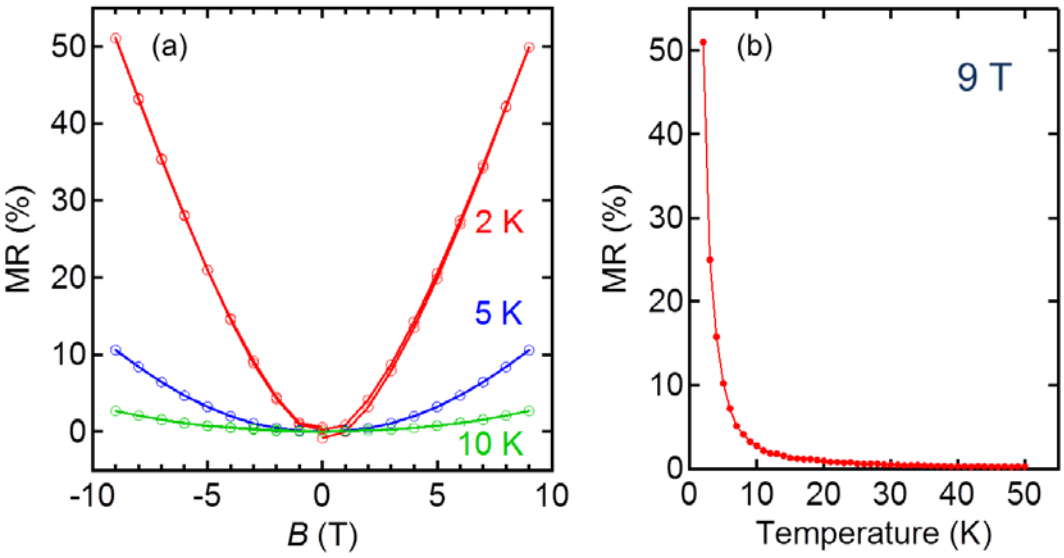

Figure 60. (a) Magnetic field dependence of MR of the $SrNbO_2N$ film measured at three temperature points and (b) temperature dependence of MR value of the $SrNbO_2N$ film measured at 9 T.

MR behaviors of non-magnetic materials have been widely reported and some mechanisms have been proposed so far: 1) A classical theory explained MR behavior of metals which can be treated as Fermi gas with free electrons and derived the magnetic field dependence as $\mathrm{MR} \propto (\mu B)^2$ based on Lorentz force applied to the electrons [88]. 2) Parish *et al*. reported that some of positive MR effects of nonmagnetic materials can be explained by construction of a "resister network" [125]. The model is suitable to describe inner equivalent electrical circuit of inhomogeneous semiconductors including doped silver chalcogenides. 3) As for the conduction mechanisms in disordered electron systems showing VRH conduction, magnetic field dependence has been a topic of great interest for both theoreticians and experimentalists and some mechanisms has been proposed on positive and negative MR effects so far [126].

The MR effect of $SrNbO_3$ can be understood by the classical theory based on

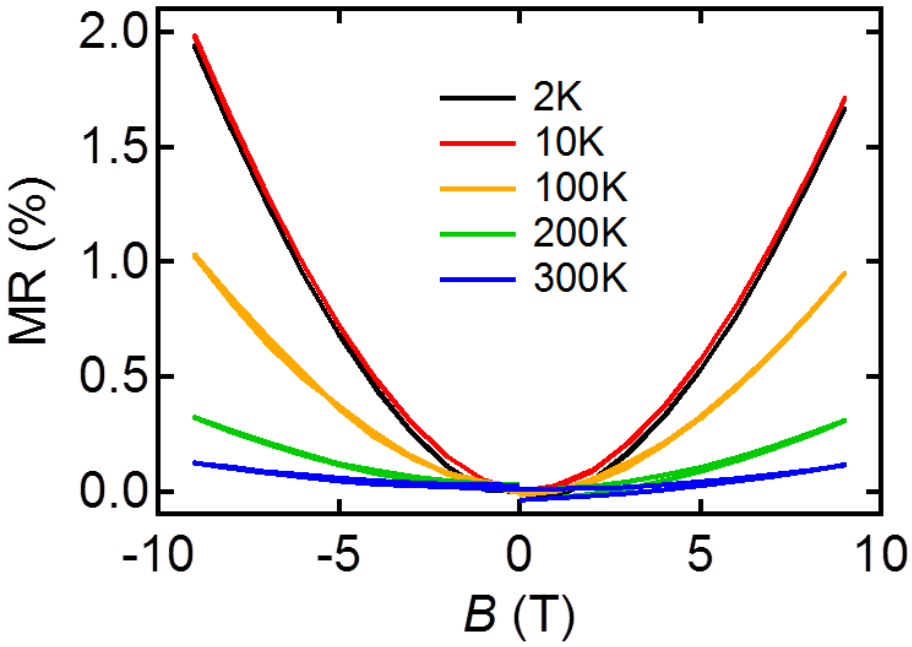

Figure 61. Magnetic field dependence of MR of the $SrNbO_3$ film measured at several temperature points.

Fermi gas, because all the MR curves measured at different temperatures can be fitted by quadratic curves (Fig. 61). The MR amplitude was of the order of few %, which is similar to the MR effects of usual metals. On the other hand, the classical theory is not applicable to the MR behaviors of $SrNbO_{3-x}N_x$ ($x > 0$) films because the trend that MR amplitude raises with increasing nitrogen content, which induces reduction in mobility μ, is contradicting to the classical expression of $\mathrm{MR} \propto (\mu B)^2$.

The "random resister model" is also not likely to give a reasonable explanation for them. Because the theory is based on Lorentz force on electrons, MR effect in the regime should have large dependence on the direction of applied field. Figure 62 shows the MR effect as a function of the angle of applied field. The difference in resistivity by changing the angle is less than 2 %, which indicates that the MR effect is highly

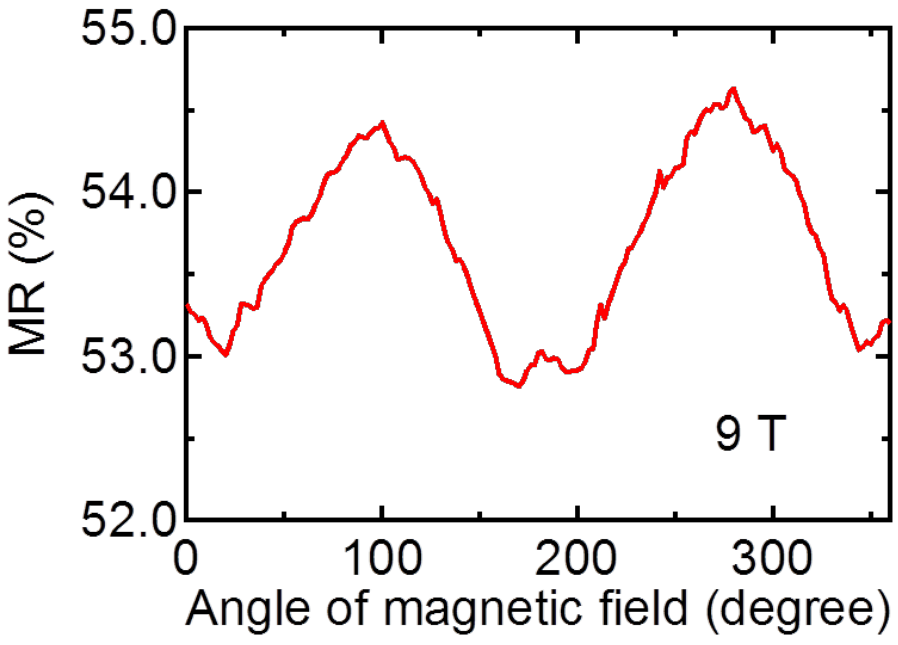

Figure 62. MR of the $SrNbO_2N$ epitaxial thin film measured at 2K and 9 T as a function of magnetic field angle. Magnetic field was rotated around [010] axis where current flows and 0° and 90° indicates [100] and [001] directions, respectively.

isotropic.

Thus, MR effect based on VRH conduction is the most probable origin considering the fact that the conductivity of the $SrNbO_2N$ film as a function of temperature followed Mott VRH law at low temperature. As an origin of positive MR in disordered semiconductors, the wave-function shrinking model has been proposed and investigated by some theoreticians. In the model, applied magnetic field causes shrinkage of localized orbitals and reduces the probability of electron hopping, which increases resistance. Magnetic field also induces decrease in resistance (i.e. negative MR effect) in disordered systems. Some numerical investigations treated quantum interferences among forward scattering paths and derived both positive and negative MR effects [127–130].

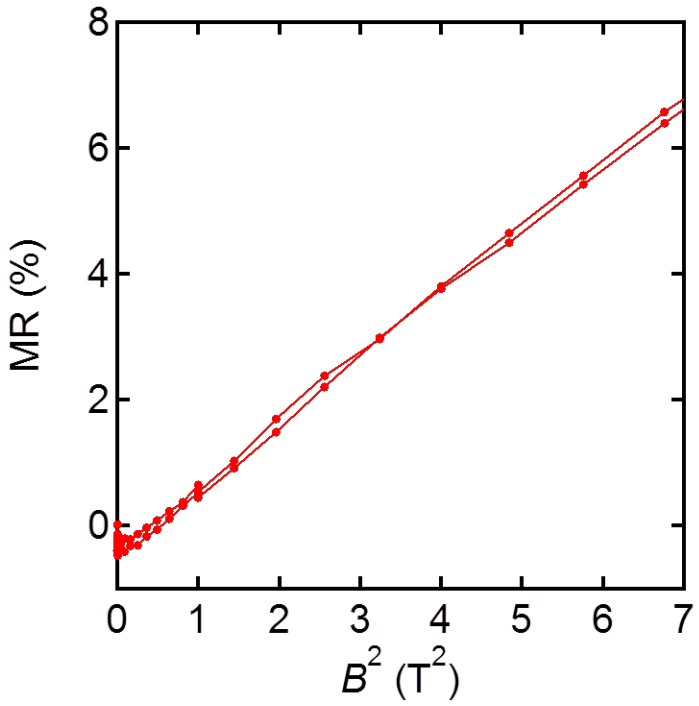

Figure 63. Low field MR of the $SrNbO_2N$ epitaxial thin film measured at 2 K as a function of B^2.

In this study, the $SrNbO_2N$ thin films showed negative MR in the very low field region at 2 K followed by positive MR growing as B^2 (Fig. 63). The negative and positive MR behaviors are possibly attributable to the quantum effect and orbital shrinkage mentioned above. At high field region, the MR value of the $SrNbO_2N$ film was positive and increased as $B^{3/2}$. The other MR curves taken on the $SrNbO_{3-x}N_x$ ($x >$

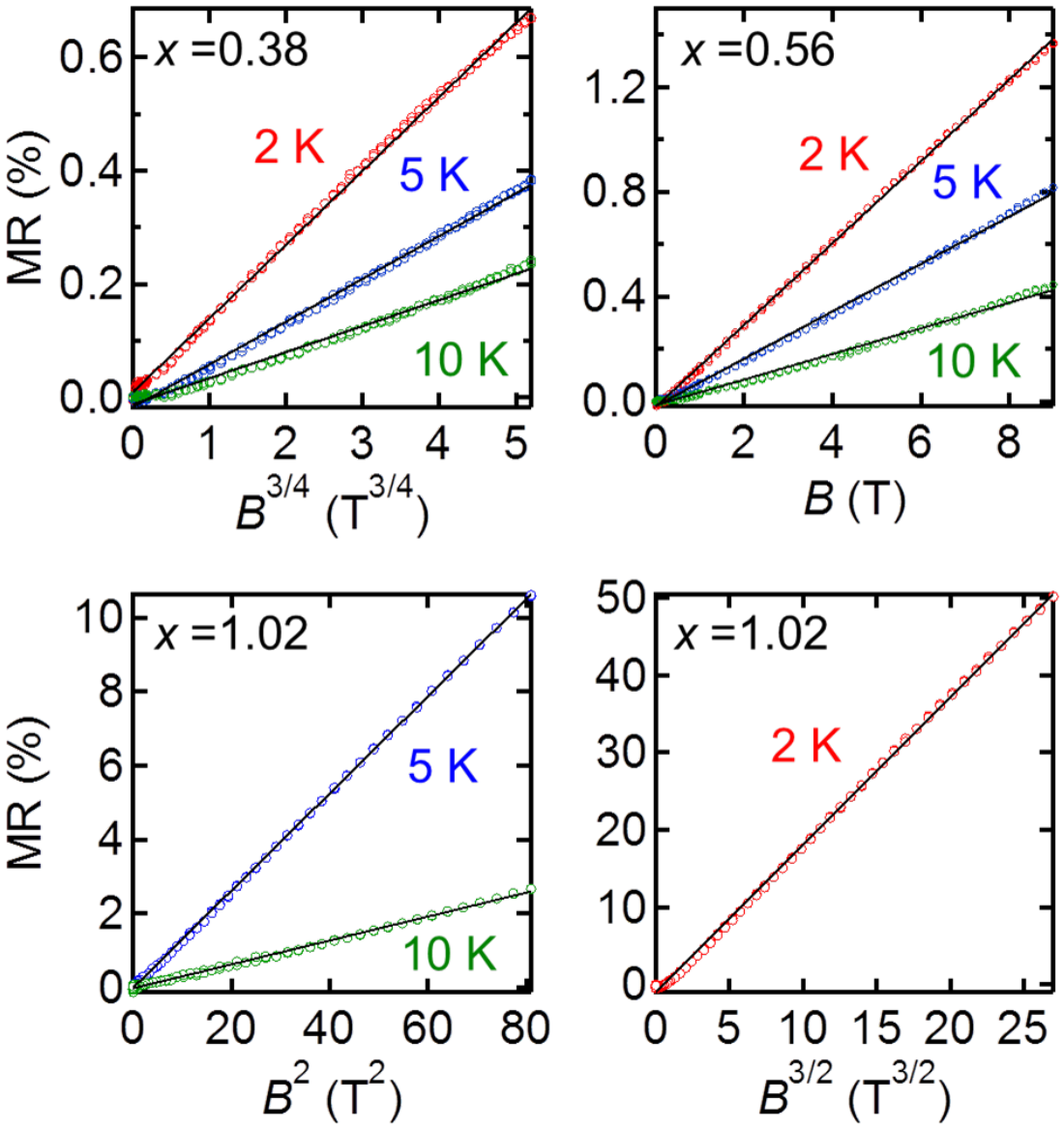

Figure 64. MR of the $SrNbO_{3-x}N_x$ epitaxial thin films as functions of powered *B*.

0) films also showed MR curves described by powered B but with different indices: MR $\propto B^{3/4}$, B, B^2 for x = 0.34, 0.56, 1.02 (at 5 and 10 K), respectively (Fig. 64). As for the film with x = 0.07, the MR effect was too small. In order to analyze these behaviors quantitatively, more detailed theoretical investigations are needed.

7.4 Conclusion

I demonstrated filling control of the conduction band of $SrNbO_{3-x}N_x$ composed mainly of 4d orbital of Nb by changing nitrogen content x. The $SrNbO_3$ epitaxial thin film, one of the end members of the system with d^1 electronic configuration, showed low resistivity of the order of 10^{-6}–10^{-5} Ωcm and metallic temperature dependence ($d\rho/dT > 0$). By introducing nitrogen, lattice relaxation was induced even with the small amount of x = 0.07, and resistivity increased with higher nitrogen amount. Temperature dependence of ρ was changed from metallic to semiconducting at a critical composition of x = 0.38 and finally becomes insulating at x =1.02. At the same time, nitrogen introduction caused significant change in optical absorption spectrum. Broad free electron absorption was suppressed in IR region by increasing x while visible light absorption (> 2.0 eV) was enhanced due to the shift of electronic transition mechanism from intraband to interband ones. Both of the electrical transport and optical properties indicate that the $SrNbO_{3-x}N_x$ system can be described by the rigid band model, in which the band filling is tunable with nitrogen content.

In addition, I found magnetoresistive behavior in $SrNbO_{3-x}N_x$ at low temperature. While the end member $SrNbO_3$ showed MR describable by the classical

electromagnetics theory, the oxynitride thin films with $x > 1$ exhibited MR behaviors probably originating from orbital shrinkage by magnetic field. The highest MR observed in the $SrNbO_2N$ thin film raised with decreasing temperature and reached about 50% at 2 K under magnetic field of 9 T. This result revealed that nitrogen can contribute to strong localization of wave function in perovskite oxynitrides, which may result in anomalous effects in electrical conductivity including large magnetoresistance.

Chapter 8

General conclusion

In this thesis I demonstrated that the approach using heteroepitaxy is significantly effective in the researches of perovskite oxynitrides. The technique of nitrogen plasma assisted pulsed laser deposition (NPA-PLD) enabled to synthesize phase pure epitaxial thin films of perovskite oxynitrides: $SrTaO_2N$, $CaTaO_2N$, $Ca_{1-x}Sr_xTaO_2N$ and $SrNbO_{3-x}N_x$. Impedance measurement on the $SrTaO_2N$ and $CaTaO_2N$ epitaxial thin films confirmed that the quality of the films was high enough to conduct reliable electrical measurements. The success in fabricating the high quality oxynitride thin films and survey on novel functionalities in them led to the following findings:

Ferroelectricity in the $SrTaO_2N$ epitaxial thin film

The $SrTaO_2N$ epitaxial thin films showed ferroelectricity, which has not been observed in bulk specimens so far. Piezoresponse force microscopy revealed that the films were composed of small domains with classical ferroelectricity surrounded by relaxer-like matrix part. First principles studies suggested that the former originated from *trans*-type structure stabilized by the large epitaxial strain while the latter possessed plausibly *cis*-type structure. The present study paved a new way to develop novel electrical properties by tuning anion arrangement with epitaxial strain.

Artificial control on anion arrangement

A series of $Ca_{1-x}Sr_xTaO_2N$ epitaxial thin films grown coherently on Nb:$SrTiO_3$ and $DyScO_3$ single crystals showed systematic change in tetragonal distortion caused by epitaxial strain. X-ray absorption spectroscopy indicated clear difference in nitrogen occupancy between axial and equatorial sites in the highly distorted films. Furthermore, higher occupation on the axial site by nitrogen ions was confirmed by electron energy loss spectroscopy combined with scanning transmission electron microscopy. These results provided strong evidence for the influence of epitaxial strain on anion arrangement.

Conductive properties in $SrNbO_{3-x}N_x$

NPA-PLD allowed precise tuning on nitrogen content in $SrNbO_{3-x}N_x$ thin films and resulting electrical properties which could be explained by rigid band model. The $SrNbO_2N$ thin film showed insulating behavior despite the high carrier density over $1 \times 10^{21} cm^{-3}$, which was caused by strong localization of wave function probably induced by random distribution of nitrogen. The strong localization of wave function resulted in large positive magnetoresistance at low temperature. The phenomenon is plausibly explained by wave function shrinkage model.

Bibliography

[1] A. S. Bhalla, R. Guo, and R. Roy, Mater. Res. Innov. **4**, 3 (2000).

[2] G. H. Haertling, J. Am. Ceram. Soc. **82**, 797 (1999).

[3] A. Urushibara, Y. Moritomo, T. Arima, A. Asamitsu, G. Kido, and Y. Tokura, Phys. Rev. B **51**, 103 (1995).

[4] S. Stramare, V. Thangadurai, and W. Weppner, Chem. Mater. **15**, 3974 (2003).

[5] B. Batlogg, Phys. B C **126**, 275 (1984).

[6] Y. Kobayashi, O. J. Hernandez, T. Sakaguchi, T. Yajima, T. Roisnel, Y. Tsujimoto, M. Morita, Y. Noda, Y. Mogami, A. Kitada, M. Ohkura, S. Hosokawa, Z. Li, K. Hayashi, Y. Kusano, J. E. Kim, N. Tsuji, A. Fujiwara, Y. Matsushita, K. Yoshimura, K. Takegoshi, M. Inoue, M. Takano, and H. Kageyama, Nat. Mater. **11**, 507 (2012).

[7] M. Jansen and H. Letschert, Nature **404**, 980 (2000).

[8] R. Aguiar, D. Logvinovich, A. Weidenkaff, A. Rachel, A. Reller, and S. G. Ebbinghaus, Dye. Pigment. **76**, 70 (2008).

[9] S. G. Ebbinghaus, H.-P. Abicht, R. Dronskowski, T. Müller, A. Reller, and A. Weidenkaff, Prog. Solid State Chem. **37**, 173 (2009).

[10] A. Kasahara, K. Nukumizu, G. Hitoki, T. Takata, J. N. Kondo, M. Hara, H. Kobayashi, and K. Domen, J. Phys. Chem. A **106**, 6750 (2002).

[11] Y.-I. Kim, P. M. Woodward, K. Z. Baba-Kishi, and C. W. Tai, Chem. Mater. **16**, 1267 (2004).

[12] B. Ravel, Y.-I. Kim, P. Woodward, and C. Fang, Phys. Rev. B **73**, 1 (2006).

[13] Y. Hinuma, H. Moriwake, Y. Zhang, T. Motohashi, S. Kikkawa, and I. Tanaka,

Chem. Mater. **24**, 4343 (2012).

[14] R. Aguiar, D. Logvinovich, a Weidenkaff, H. Karl, C. Schneider, a Reller, and S. Ebbinghaus, Mater. Res. Bull. **43**, 1376 (2008).

[15] Y. Lu, C. Le Paven-Thivet, R. Benzerga, L. Le Gendre, a. Sharaiha, F. Tessier, and F. Cheviré, Appl. Surf. Sci. **264**, 533 (2013).

[16] A. Ziani, C. Lepaventhivet, L. Legendre, D. Fasquelle, J. Carru, F. Tessier, and J. Pinel, Thin Solid Films **517**, 544 (2008).

[17] I. C. Lekshmi, A. Gayen, and M. S. Hegde, Mater. Res. Bull. **40**, 93 (2005).

[18] I. Marozau, A. Shkabko, M. Döbeli, and T. Lippert, Acta Mater. **59**, 7145 (2011).

[19] R. Marchand, F. Pors, Y. Laurent, O. Regreny, J. Lostec, and J. M. Haussonne, J. Phys. Colloq. **47**, c1 (1986).

[20] D. Serrate, J. M. De Teresa, and M. R. Ibarra, J. Phys. Condens. Matter **19**, 023201 (2007).

[21] F. Pors, R. Marchand, Y. Laurent, P. Bacher, and G. Roult, Mater. Res. Bull **23**, 1447 (1988).

[22] X. Gouin, R. Marchand, Y. Laurent, and F. Gervais, Solid State Commun. **93**, 857 (1995).

[23] S. J. Clarke, K. a. Hardstone, C. W. Michie, and M. J. Rosseinsky, Chem. Mater. **14**, 2664 (2002).

[24] A. Rachel, S. G. Ebbinghaus, M. Güngerich, P. J. Klar, J. Hanss, A. Weidenkaff, and A. Reller, Thermochim. Acta **438**, 134 (2005).

[25] M. Higashi, R. Abe, T. Takata, and K. Domen, Chem. Mater. **21**, 1543 (2009).

[26] A. Gomathi, S. Reshma, and C. Rao, J. Solid State Chem. **182**, 72 (2009).

[27] Y.-I. Kim and E. Lee, J. Ceram. Soc. Japan **119**, 371 (2011).

[28] M. R. Brophy, S. M. Pilgrim, and W. a. Schulze, J. Am. Ceram. Soc. **94**, 4263 (2011).

[29] S. Balaz, S. H. Porter, P. M. Woodward, and L. J. Brillson, Chem. Mater. **25**, 3337 (2013).

[30] E. Günther, R. Hagenmayer, and M. Jansen, Zeitschrift Für Anorg. Und Allg. Chemie **626**, 1519 (2000).

[31] S. G. Ebbinghaus, R. Aguiar, A. Weidenkaff, S. Gsell, and A. Reller, Solid State Sci. **10**, 709 (2008).

[32] M. Yang, J. Oró-Solé, J. a Rodgers, A. B. Jorge, A. Fuertes, and J. P. Attfield, Nat. Chem. **3**, 47 (2011).

[33] Y.-R. Zhang, T. Motohashi, Y. Masubuchi, and S. Kikkawa, J. Ceram. Soc. Japan **119**, 581 (2011).

[34] Y.-R. Zhang, T. Motohashi, Y. Masubuchi, and S. Kikkawa, J. Eur. Ceram. Soc. **32**, 1269 (2012).

[35] Y. Zhang, Y. Masubuchi, T. Motohashi, S. Kikkawa, and K. Hirota, Ceram. Int. **39**, 3377 (2013).

[36] Y.-I. Kim, Ceram. Int. **40**, 5275 (2014).

[37] K. Maeda, M. Higashi, B. Siritanaratkul, R. Abe, and K. Domen, J. Am. Chem. Soc. **133**, 12334 (2011).

[38] B. Siritanaratkul, K. Maeda, T. Hisatomi, and K. Domen, ChemSusChem **4**, 74 (2011).

[39] S. J. Clarke, B. P. Guinot, C. W. Michie, M. J. C. Calmont, and M. J. Rosseinsky, Chem. Mater. **14**, 288 (2002).

[40] D. Logvinovich, L. Bocher, D. Sheptyakov, R. Figi, S. G. Ebbinghaus, R. Aguiar, M. H. Aguirre, A. Reller, and A. Weidenkaff, Solid State Sci. **11**, 1513 (2009).

[41] M. Yashima, M. Saito, H. Nakano, T. Takata, K. Ogisu, and K. Domen, Chem. Commun. (Camb). **46**, 4704 (2010).

[42] N.-Y. Park and Y.-I. Kim, J. Mater. Sci. **47**, 5333 (2012).

[43] D. Logvinovich, S. G. Ebbinghaus, A. Reller, I. Marozau, D. Ferri, and A. Weidenkaff, Zeitschrift Für Anorg. Und Allg. Chemie **636**, 905 (2010).

[44] D. Logvinovich, R. Aguiar, R. Robert, M. Trottmann, S. G. Ebbinghaus, a. Reller, and a. Weidenkaff, J. Solid State Chem. **180**, 2649 (2007).

[45] D. Logvinovich, J. Hejtmánek, K. Knížek, M. Maryško, N. Homazava, P. Tomeš, R. Aguiar, S. G. Ebbinghaus, a. Reller, and a. Weidenkaff, J. Appl. Phys. **105**, 023522 (2009).

[46] I. D. Fawcett, K. V. Ramanujachary, and M. Greenblatt, Mater. Res. Bull. **32**, 1565 (1997).

[47] G. Liu, X Zhao and H.A. Eick, J. Alloy. Compd. **187**, 145 (1992).

[48] A. Kusmartseva, M. Yang, J. Oró-Solé, a. M. Bea, a. Fuertes, and J. P. Attfield, Appl. Phys. Lett. **95**, 022110 (2009).

[49] M. Yang, J. Oró-Solé, A. Kusmartseva, A. Fuertes, and J. P. Attfield, J. Am. Chem. Soc. **132**, 4822 (2010).

[50] A. B. Jorge, J. Oró-Solé, A. M. Bea, N. Mufti, T. T. M. Palstra, J. a Rodgers, J. P. Attfield, and A. Fuertes, J. Am. Chem. Soc. **130**, 12572 (2008).

[51] D. Logvinovich, M. H. Aguirre, J. Hejtmanek, R. Aguiar, S. G. Ebbinghaus, a. Reller, and a. Weidenkaff, J. Solid State Chem. **181**, 2243 (2008).

[52] Y.-I. Kim and P. M. Woodward, J. Solid State Chem. **180**, 3224 (2007).

[53] J. Grins and G. Svensson, Mater. Res. Bull. **29**, 801 (1994).

[54] K. Maeda and K. Domen, J. Catal. **310**, 67 (2014).

[55] F. Chevire, F. Tessier, and R. Marchand, ChemInform **37**, (2006).

[56] D. Logvinovich, a Borger, M. Dobeli, S. Ebbinghaus, a Reller, and a Weidenkaff, Prog. Solid State Chem. **35**, 281 (2007).

[57] N. Kumar, A. Sundaresan, and C. Rao, Mater. Res. Bull. **46**, 2021 (2011).

[58] J. Oró-Solé, L. Clark, W. Bonin, J. P. Attfield, and A. Fuertes, Chem. Commun. (Camb). **49**, 2430 (2013).

[59] M. Yang, J. a Rodgers, L. C. Middler, J. Oró-Solé, a B. Jorge, A. Fuertes, and J. P. Attfield, Inorg. Chem. **48**, 11498 (2009).

[60] R. Aguiar, a Weidenkaff, C. Schneider, a Reller, and S. Ebbinghaus, Prog. Solid State Chem. **35**, 291 (2007).

[61] Y.-I. Kim, W. Si, P. M. Woodward, E. Sutter, S. Park, and T. Vogt, Chem. Mater. **19**, 618 (2007).

[62] D. Fasquelle, a. Ziani, C. Le Paven-Thivet, L. Le Gendre, and J. C. Carru, Mater. Lett. **65**, 3102 (2011).

[63] Y. Lu, C. Le Paven, H. V. Nguyen, R. Benzerga, L. Le Gendre, S. Rioual, F. Tessier, F. Cheviré, A. Sharaiha, C. Delaveaud, and X. Castel, Cryst. Growth Des. **13**, 4852 (2013).

[64] C. Le Paven-Thivet, L. Le Gendre, J. Le Castrec, F. Cheviré, F. Tessier, and J. Pinel, Prog. Solid State Chem. **35**, 299 (2007).

[65] C. Le Paven-Thivet, A. Ishikawa, A. Ziani, L. Le Gendre, M. Yoshida, J. Kubota, F. Tessier, and K. Domen, J. Phys. Chem. C **113**, 6156 (2009).

[66] A. E. Maegli, L. Sagarna, S. Populoh, B. Penkala, E. H. Otal, and A.

Weidenkaff, J. Solid State Chem. **211**, 106 (2014).

[67] A. Fuertes, Dalton Trans. **39**, 5942 (2010).

[68] S. H. Elder, F. J. DiSalvo, L. Topor, and A. Navrotsky, Chem. Mater. **5**, 1545 (1993).

[69] P. R. Willmott, Appl. Phys. A **69**, 437 (1999).

[70] P. R. Willmott and J. Huber, Rev. Mod. Phys. **72**, 315 (2000).

[71] I. Marozau, a. Shkabko, G. Dinescu, M. Döbeli, T. Lippert, D. Logvinovich, M. Mallepell, a. Weidenkaff, and a. Wokaun, Appl. Phys. A **93**, 721 (2008). [76] A. M. Glazer, Acta Crystallogr. Sect. B Struct. Crystallogr. Cryst. Chem. **28**, 3384 (1972).

[72] C. J. Howard and H. T. Stokes, Acta Crystallogr. Sect. B Struct. Sci. **54**, 782 (1998).

[73] J. P. Attfield, Cryst. Growth Des. **13**, 4623 (2013).

[74] K. Page, M. W. Stoltzfus, Y.-I. Kim, T. Proffen, P. M. Woodward, A. K. Cheetham, and R. Seshadri, Chem. Mater. **19**, 4037 (2007).

[75] R. L. Withers, Y. Liu, P. Woodward, and Y.-I. Kim, Appl. Phys. Lett. **92**, 102907 (2008).

[76] C. Fang, J. Phys. Chem. Solids **64**, 281 (2003).

[77] H. Wolff and R. Dronskowski, J. Comput. Chem. **29**, 2260 (2008).

[78] K. Tatsumi and R. Hoffmann, Inorg. Chem. **19**, 2656 (1980).

[79] P. J. Camp, A. Fuertes, and J. P. Attfield, J. Am. Chem. Soc. **134**, 6762 (2012).

[80] A. Fujishima and K. Honda, Nature, **238**, 37 (1972).

[81] K. Maeda and K. Domen, J. Phys. Chem. Lett. **1**, 2655 (2010).

[82] T. Hisatomi, J. Kubota, and K. Domen, Chem. Soc. Rev. **43**, 7520 (2014).

[83] Y. Moriya, T. Takata, and K. Domen, Coord. Chem. Rev. **257**, 1957 (2013).

[84] A. Tsukazaki, A. Ohtomo, T. Onuma, M. Ohtani, T. Makino, M. Sumiya, K. Ohtani, S. F. Chichibu, S. Fuke, Y. Segawa, H. Ohno, H. Koinuma, and M. Kawasaki, Nat. Mater. **4**, 42 (2004).

[85] D. B. Cherisey and G. K. Hubler, *Pulased Laser Deposition of Thin Films* (Wiley, New York, 1994).

[86] D. Lowndes, D. Geohegan, and A. Puretzky, Science (1996).

[87] T. Ohnishi, H. Koinuma, and M. Lippmaa, Appl. Surf. Sci. **252**, 2466 (2006).

[88] C. Kittel, *Introduction to Solid State Physics (8th edition)* (Wiley, New York, 2004).

[89] D. P. Norton, Mater. Sci. Eng. R Reports **43**, 139 (2004).

[90] S. Ohashi, M. Lippmaa, N. Nakagawa, H. Nagasawa, H. Koinuma, and M. Kawasaki, Rev. Sci. Instrum. **70**, 178 (1999).

[91] C. J. Tung, J. C. Ashley, and R. H. Ritchie, Surf. Sci. **81**, 427 (1979).

[92] B. D. Cullity and S. R. Stock, *Elements of X-Ray Diffraction (3rd Edition)* (Prentice Hall, 2011).

[93] G. Binnig, C. Quate, and C. Gerber, Phys. Rev. Lett. **56**, (1986).

[94] B. Cappella and G. Dietler, Surf. Sci. Rep. **34**, 1 (1999).

[95] F. J. Giessibl, Rev. Mod. Phys. **75**, 949 (2003).

[96] 日本表面科学会 編、透過型電子顕微鏡、1999 年、丸善株式会社

[97] J. M. Cowley, Appl. Phys. Lett. **15**, 58 (1969).

[98] N. Dellby, O. L. Krivanek, P. D. Nellist, P. E. Batson, and a. R. Lupini, Microscopy **50**, 177 (2001).

[99] J. R. Tesmer and M. Nastasi, *Handbook of modern ion beam analysis* (Material Research Society, 1995).

[100] 藤原裕之、分光エリプソメトリー、2003、丸善株式会社

[101] J.-T. Zettler, Prog. Cryst. Growth Charact. Mater. **35**, 27 (1997).

[102] S. V Kalinin, A. Rar, and S. Jesse, IEEE Trans. Ultrason. Ferroelectr. Freq. Control **53**, 2226 (2006).

[103] S. V Kalinin, A. N. Morozovska, L. Q. Chen, and B. J. Rodriguez, Reports Prog. Phys. **73**, 056502 (2010).

[104] H. Okino, J. Sakamoto, and T. Yamamoto, Jpn. J. Appl. Phys. **42**, 6209 (2003).

[105] Agilent Impedance Measurement Handbook: A guide to measurement technology and techniques 4th Edition (Agilent Technologies, 2013)

[106] 日本化学会 編、実験化学講座7 電気物性、磁気物性（第 5 版）、2004、丸善株式会社

[107] J. G. Chen, Surf. Sci. Rep. **30**, 1 (1997).

[108] P. Lee, P. Citrin, P. Eisenberger, and B. Kincaid, Rev. Mod. Phys. **53**, 769 (1981).

[109] T. C. Kaspar, A. Ney, A. N. Mangham, S. M. Heald, Y. Joly, V. Ney, F. Wilhelm, A. Rogalev, F. Yakou, and S. A. Chambers, Phys. Rev. B **86**, 035322 (2012).

[110] K. Kimoto, T. Asaka, T. Nagai, M. Saito, Y. Matsui, and K. Ishizuka, Nature **450**, 702 (2007).

[111] D. A. Muller, L. F. Kourkoutis, M. Murfitt, J. H. Song, H. Y. Hwang, J. Silcox, N. Dellby, and O. L. Krivanek, Science **319**, 1073 (2008).

[112] R. Aguiar, D. Logvinovich, A. Weidenkaff, A. Reller, and S. G. Ebbinghaus, Thermochim. Acta **471**, 55 (2008).

[113] Mayer, M. *SIMNRA User's Guide*, *Report IPP 9/113*, (Max-Planck-Institut für

Plasmaphysik, Garching, Germany, 1997)

[114] V. Shvartsman, A. Kholkin, A. Orlova, D. Kiselev, A. A. Bogomolov, and A. Sternberg, Appl. Phys. Lett. **86**, (2005).

[115] Y. Kim, A. N. Morozovska, A. Kumar, S. Jesse, E. a Eliseev, F. Alibart, D. Strukov, and S. V Kalinin, ACS Nano **6**, 7026 (2012).

[116] C. W. Bark, P. Sharma, Y. Wang, S. H. Baek, S. Lee, S. Ryu, C. M. Folkman, T. R. Paudel, A. Kumar, S. V. Kalinin, A. Sokolov, E. Y. Tsymbal, M. S. Rzchowski, A. Gruverman, and C. B. Eom, Nano Lett. **12**, 1765 (2012).

[117] A. A. Bokov and Z.-G. Ye, J. Mater. Sci. **41**, 31 (2006).

[118] R. Parker, Phys. Rev. **124**, 1719 (1961).

[119] K. J. Choi, M. Biegalski, Y. L. Li, A. Sharan, J. Schubert, R. Uecker, P. Reiche, Y. B. Chen, X. Q. Pan, V. Gopalan, L.-Q. Chen, D. G. Schlom, and C. B. Eom, Science. **306**, 1005 (2004).

[120] Y. Inoue, Energy Environ. Sci. **2**, 364 (2009).

[121] S. Y. Yang, J. Seidel, S. J. Byrnes, P. Shafer, C.-H. Yang, M. D. Rossell, P. Yu, Y.-H. Chu, J. F. Scott, J. W. Ager, L. W. Martin, and R. Ramesh, Nat. Nanotechnol. **5**, 143 (2010).

[122] A. L. Efros and B. I. Shklovskii, J. Phys. C Solid State Phys. **8**, L49 (2001).

[123] Y. Xu, D. Ephron, and M. Beasley, Phys. Rev. B **52**, (1995).

[124] X. Xu, C. Randorn, P. Efstathiou, and J. Irvine, Nat. Mater. **11**, 595 (2012).

[125] M. Parish and P. Littlewood, Nature **426**, 1 (2003).

[126] P. A. Lee and T. V. Ramakrishnan, Rev. Mod. Phys. **57**, 287 (1985).

[127] V. Nguen, B. Spivak, and B. Shklovskii, Zh. Eksp. Teor. Fiz **1784**, 1021 (1985).

[128] U. Sivan, O. Entin-Wohlman, and Y. Imry, Phys. Rev. Lett. **60**, 1566 (1988).

[129] E. Medina, M. Kardar, Y. Shapir, and X. Wang, Phys. Rev. Lett. **64**, 1816 (1990).

[130] A. V. Shumilin and V. I. Kozub, Phys. Rev. B **85**, 115203 (2012).

[131] K. Momma and F. Izumi, J. Appl. Crystallogr. **44**, 1272 (2011).